ALMA MATER STUDIORUM
UNIVERSITÀ DI BOLOGNA

DOTTORATO DI RICERCA IN

IL FUTURO DELLA TERRA, CAMBIAMENTI CLIMATICI E SFIDE SOCIALI

Ciclo 37

Settore Concorsuale: 04/A4 - GEOFISICA

Settore Scientifico Disciplinare: GEO/10 - GEOFISICA DELLA TERRA SOLIDA

TRANSIENT DEFORMATIONS: UNDERSTANDING EARTH'S INTERIOR THROUGH CLIMATE CHANGE

Presentata da: Anastasia Consorzi

Coordinatore Dottorato

Silvana Di Sabatino

Supervisore

Giorgio Spada

Co-Supervisore

Daniele Melini

Esame finale anno 2025

Contents

List of Figures

Abstract

Transient effects in the response of the Earth to surface unloading events is a topic that, in spite of its first appearance almost fifty years ago, is still a matter of debate in the geophysical community. Transient patterns have been recognized in post seismic deformation, and their presence as a creep mechanism is observed in laboratory experiments. However, when it comes to Glacial Isostatic Adjustment, or, more in general, unloading (and loading) events, their presence is hard to identify. The reasons are numerous as much as the variables that take part in this process - Earth's rheology and structure, ice-sheet evolution, size and dynamics, *et cetera*. Still, recognizing their presence (or justifying their absence) would represent a significant step towards a comprehensive understanding of mantle relaxation mechanisms at intermediate time scales.

In this work, I examine the response of several Earth models including layers with transient rheology. The aim is outlining the most favorable conditions under which we can expect to observe, through geodetic techniques, transient deformations following an unloading event. Particularly, this Thesis explores in a detailed way the Andrade rheology, a transient model that has gained much success in recent years, especially in the planetary sciences community. Two of the main results of my work are indeed the recovery of the analytical expressions of the relaxation modulus in the time domain of the Andrade model and the Love numbers for an homogeneous Andrade planet. The methods that I developed in the context of the transient Earth's response to surface unloading are rather general, so I have been able to apply them also to a set of case

studies about the response of extrasolar planets to tidal and loading forcings. Part of this work is presented here as well. To probe the influence of transient rheology, I employ Andrade's law in some of the layers of my Earth's models, notably those which compose the mantle, and I run some comparison test to evaluate potential discrepancies with similar Earth's models that instead contemplated only steady-state rheology (Maxwell) in their viscous layers. These experiments consider three different scenarios: the first two are toy-tests, whose design is kept simple to allow a easy and direct interpretation or the role of each model parameter; contrarily, the last depicts a more realistic situation, and employs a high-resolution ice model describing the evolution of Helheim Glacier, in Greenland.

My findings indicate that fast changes in the load history (*i.e.,* the function that describes the temporal evolution of the ice load) and the position of the observation point with respect to the melting masses are parameters of utmost relevance. In regions characterized by a shallow elastic lithosphere, transient features emerge more clearly, due to the stronger influence of the underlying viscous layers given by their proximity to the surface. Moreover, the displacement rates reach the maximum difference from their non-transient counterparts in the regions right beneath the shrinking load, suggesting that, in the future, sub-glacial geodesy campaigns may significantly improve the identification of transient features in the Earth's response. My work also suggests that there exists a range of viscosities in which the discrepancies between the surface response produced by the Andrade Earth's models and the Maxwell ones are maximized: indeed, small values of viscosity allow Maxwell models to relax earlier and to produce trends similar to those of Andrade's ones, while in case of larger viscosity values, the differences between the output rates increase. However, assuming larger values of viscosity in the uppermost part of the mantle makes both configurations more stiff, and, as a result, the responses at the surface are extremely similar to their elastic counterpart, and the viscoelastic contribution is difficult to recognize. Finally, by comparing the outcomes produced by

various kinds of ice-histories, it is evident that sudden changes promote the identification of transient displacements at the surface, whilst in case of slow, progressive ice evolution, which allows the Earth's model to adjust gradually, it is not possible to distinguish any transient regime. However, a noteworthy result of my tests consists in the fact that even for medium-scale glaciers, the viscoelastic (or *anelastic*) contributions to the displacement may be significant already on short time periods ($\sim 15\ yr$).

These results emphasize the importance of studying transient rheological phenomena. Moreover, these kind of studies became even more crucial in the context of present-day climate change. Many ice-covered regions around the world, like Antarctica and Greenland, are experiencing a rising number of extreme melting events, calvings, and other important variations that affect the equilibrium between the hydrosphere, the cryosphere and the geosphere. Hence, the growth both in number and magnitude of this phenomena may increase our possibility to observe transient signals in the Earth's response.

Chapter 1

Introduction

Understanding the Earth's dynamic behavior represents one of the most challenging tasks of modern geophysics (and maybe, also of modern physics). Our planet is a complex system made of many sub-parts that interact with one another in a non-linear way - and that is why it is called "Earth System". For this reason, in latest years, many fields of geophysics that followed separate paths in the past, have joined up together to allow a deeper understanding of a broad range of geophysical phenomena. This is particularly true in the field of Glacial Isostatic Adjustment (GIA), a process that involves the response of the Earth to the variation of surface masses like ice sheets, glaciers, and the oceans. This response includes every physical mechanism through which the planet responds to the redistribution of masses, including sea level (SL) changes, vertical and horizontal displacement at the surface over a broad range of time scales, polar wander, changes in the planet's moment of inertia *et cetera*.

In this thesis I present the outcomes of my research which concerns an aspect of GIA modeling: the response of the Earth's surface to the variation of surface loads. The interest of the community in surface (and tidal) loads resides in the fact that, as well as seismic waves, they allow us to make hypotheses about the Earth's internal behavior, and more specifically they are essential to infer Earth's mantle viscosity and

rheology. Seismology offers the chance to understand the Earth elastic behavior that, yet, represents just a "snapshot", a part, of the entire response range: in this sense, GIA provides complementary information that enables us to further understand Earth's rheology and dynamics. Ultimately, it is the way in which mantle *flows* that manifests Glacial Isostatic Adjustment.

My goal is to understand whether a particular type of deformation, the "transient deformation", can be recognized after or during unloading events. Transient deformations are expected on the basis of microphysical arguments (Karato, 2021), observed in laboratory experiments (Gribb and Cooper, 1998; Jackson and Faul, 2010), and even in other geophysical phenomena such as post-seismic deformation (Pollitz, 2005). However, until now, their role in GIA is not clear, and it has been difficult to recognize them. The main reason is because the transient stage happens in between the instantaneous elastic response and the following constant flow phase, and thus is highly probable that, if ever present, the transient stage eventually triggered by the end of the last ice age, ceased long ago. However, present-day Climate Change (CC) could represent a further push for the study of transient rheology in unloading events. The conclusions of Nield et al. (2014) further motivate the last claim: in their paper, the authors state that the simultaneous presence of low upper mantle viscosity and important on-going ice-mass changes (likely due to CC) produces displacements that can only be explained by invoking a viscoelastic response. Although in this latter example a transient is not strictly necessary to justify the observed rates, it may be required once one tries to reconcile present day observations with past rates over longer timescales. Thus, it is reasonable to think that the unprecedented rise in temperature could lead to a larger number of extreme melting events, increasing the chance of observing transients in fast-evolving ice-covered regions.

For this reason, in this work, I analyse systematically the role that each variable (rheology, viscosity, ice history, load size) plays in the modeling of this phenomenon, starting from toy experiments and concluding with a study of more realistic scenarios

concerning Greenland. The aim is not finding evidence of transient deformations from data, rather outlining precisely which are the optimal observational conditions that could permit to detect them in the field.

The Thesis is organized as follows. Chapter 1 summarizes the state of the art of the two main topics of my research work, transient rheology in geophysics and the Surface Loading Problem. The last section is dedicated to a presentation of Greenland as a case study for the surface loading problem. In Chapter 2, focused on the "Andrade rheology", some results of my research on this particular rheological model are presented. This part constitutes the theoretical basis for the applications that are presented in the following. In Chapter 3, I present the calculation of Love Numbers for some cases of interest, and it includes several outcomes of my work that have been published in two academic journals, concerning respectively the study of "Andrade Love numbers" and the "Love Numbers of fluid planets". In Chapter 4, devoted to the "Surface Loading Problem", I present the methods I followed to run my tests, including the numerical calculation and analysis of Love numbers and the calculation of the Surface Response Function. In Chapter 5 the results of the experiments, presented in this Thesis sorted by increasing complexity, are shown and discussed point-by-point. Chapter 6 shortly draws the conclusions of my work, also suggesting future research directions.

1.1 Basics of rheology

Rheology is the branch of physics that studies the "flow" of matter, or the way in which matter is deformed after the application of a stress. This discipline lays the foundations for modern geophysics, building a bridge between the physical study of matter behaviour at the micro scale and its consequences at the macro scale (Kennett and Bunge, 2008). To further study the scope of rheology, the readers are referred to the fundamental books of Christensen (1982), Ranalli (1995), and Mainardi (2022).

Examples of well-known rheological models, largely used also outside the field of geophysics, are:

- **Hooke model**: the oldest rheological model, the linear elastic body shows an instantaneous deformation ϵ following the application of an instantaneous and constant stress $\sigma_0 H(t)$ (or, *creep test*). In one dimension, we can write:

$$\sigma(t) = \mu\epsilon\,, \quad \text{with} \quad \sigma(t) = \sigma_0 H(t)\,, \quad \Longrightarrow \quad \epsilon(t) = \frac{\sigma_0}{\mu} \quad \text{for} \quad t \geq 0\,, \tag{1.1}$$

  where μ is the elastic rigidity.

- **Newton model**: the simplest mathematical way to describe a fluid body. In a creep test, the Newtonian fluid exhibits a constant strain rate:

$$\sigma(t) = \eta\dot{\epsilon},\,, \quad \text{with} \quad \sigma(t) = \sigma_0 H(t)\,, \quad \Longrightarrow \quad \epsilon(t) = \frac{\sigma_0}{\eta} t \quad \text{for} \quad t \geq 0\,, \tag{1.2}$$

  where η is the Newtonian viscosity.

- **Maxwell model**: A linear combination of the Hooke and Newton models, in other words, the instantaneous elastic response is followed by a steady state flow:

$$\epsilon(t) = \frac{\sigma_0}{\mu} H(t) + \frac{\sigma_0}{\eta} t\,, \quad \text{for} \quad t \geq 0\,. \tag{1.3}$$

It is useful, for the purposes of this Thesis, to define two basic quantities in rheology: the *creep compliance* $J(t)$, that expresses the deformation that the body undergoes after the application of a Heaviside-type unit stress $\sigma(t) = \sigma_0 H(t)$, and the *relaxation modulus* $G(t)$, that describes the stress response following a Heaviside unit deformation $\epsilon(t) = \epsilon_0 H(t)$. For example, the creep compliance and the relaxation modulus of the Maxwell body read:

$$\begin{aligned} J_M(t) &= \frac{H(t)}{\mu} + \frac{t}{\eta}\,, \quad t \geq 0\,, \\ G_M(t) &= \mu e^{-\frac{t}{\tau_M}}\,, \quad \text{with} \quad \tau_M = \frac{\eta}{\mu}\,, \quad t \geq 0\,, \end{aligned} \tag{1.4}$$

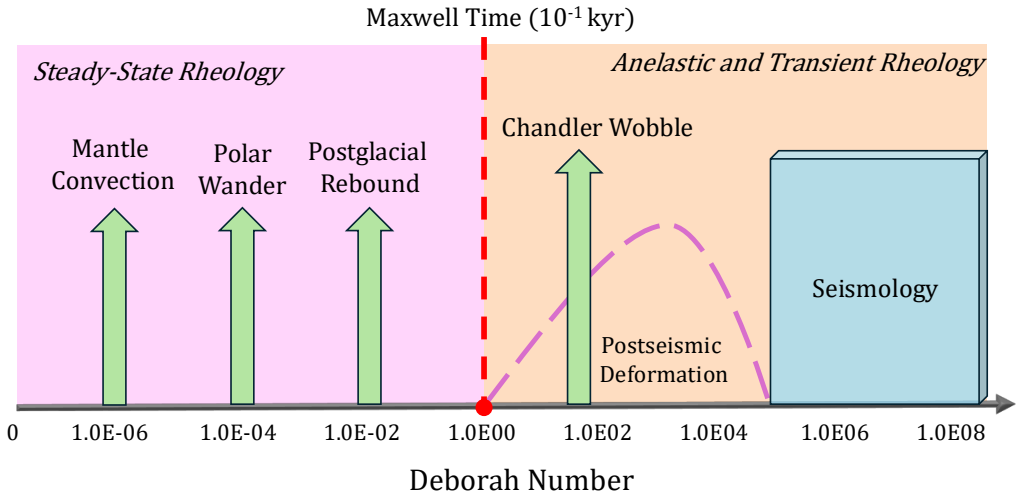

Figure 1.1: Deborah Number of some Geophysical phenomena assuming a relaxation time $\tau_M \sim 10^{-1} kyr$. This figure is inspired to Figure 1.1 of Sabadini et al. (2016).

respectively, where $\tau_M = \eta/\mu$ is called *Maxwell relaxation time*. Functions $J(t)$ and $G(t)$ are also referred to as *material functions* of the viscoelastic body (Christensen, 1982); they obey the causality principle and thus they vanish for negative times (Mainardi and Spada, 2011).

The main reason that makes rheology a pivotal discipline in geophysics is the existence of a wide range of rheological laws that can be attributed to different geophysical materials. Inside the Earth different compositions of minerals, pressure and temperature conditions lead to a vast range of rheological behaviours. However, what is interesting, when we specifically consider the case of the Earth's mantle, is that it can exhibit various "types" of rheological behaviour: in seismology, to study seismic waves propagation, it is appropriate to consider it as an elastic body, to a first approximation; on the contrary, many other phenomena like Glacial Isostatic Adjustment and polar wander require the mantle to behave in a viscoelastic way, and eventually, for mantle convection, a viscous fluid mantle is assumed. This underlines one of the most important features of rheology, that is its deep interconnection with *time scales*.

Time is of paramount importance in rheology (Ranalli, 1995). The propagation of seismic waves has characteristic times in the interval between 10^{-4} and 10^{1} s, those of GIA are traditionally estimated to be of the order of $10^{9 \div 11}$ s (*i.e.*, between 10^{-1} and 10^{1} *kyr*), and mantle convection is even slower (see the time scale diagram in Figure 2.1). These characteristic times must be compared to the *relaxation time*, τ_M, of the mantle (also referred to as Maxwell time), a parameter defined as the ratio between the Newtonian viscosity η and the elastic rigidity μ of a viscoelastic material. It gives an indication on the characteristic time scale on which steady-state behaviour occurs (Ranalli, 1995). The relaxation time of the mantle is generally considered to be approximately included in the range between 10^{-1} and 1 *kyr*. This means that, on the characteristic time scales of seismic waves propagation, the mantle is not able to relax, and it is crossed by seismic waves as it was effectively elastic, while on the other hand, the time and spatial scales of ice ages are large enough so that the mantle can manifest its viscoelastic features. Another important time parameter of rheology, is the *observation time*, τ_o, that could be defined as the time scale of the geophysical event, or, also, as the time span in which a geophysical phenomenon is observed. During the Fourth International Congress on Rheology, which took place in August 1964 in Providence, Markus Reiner (1964) merged together the concepts of relaxation time τ_M and observation time τ_o to further distinguish the notions of *solid* and *fluid*, introducing the *Deborah Number* as a useful parameter to disclose the apparent plurality of the mantle rheology:

$$De = \frac{\tau_M}{\tau_o} \,. \tag{1.5}$$

When the Deborah number is large ($De \gg 1$), the material shows elastic (or *solid*) features. As reported in Figure 1.1, the field of seismology fits perfectly this condition. On the other hand, when it is small ($De \ll 1$), considering a steady state rheology for the mantle is appropriate (as it is done in the modeling of mantle convection). Those simplifying assumptions are not possible when the Deborah number is $De \approx 1$, that is when the relaxation time τ_M is comparable with the observation time τ_o. In this

scenario, "transient deformations" gain great importance. The transient, often referred to as "*primary creep*" (Ranalli, 1995), is the phase of deformation that immediately follows the elastic response, in which the *strain rate varies with time*. Transient signals have been observed observed in the context of post-seismic deformation: after a large earthquake, a part of the stress changes induced by the event will gradually be released through time-decaying deformation. (see *e.g.*, Pollitz (2005); Weiss et al. (2019)).

Through the years, a large number of transient models have been proposed, and one of the most employed in geophysics, especially for describing Earth's mantle, is the bi-viscous Burgers model. The Burgers model, indeed, can account for both a fast transient response and for a Maxwell-style viscoelastic relaxation on longer timescales, thus being able to satisfactorily represent the behavior of the mantle in response both to seismic waves and post glacial rebound (Peltier et al., 1986). However, a drawback of Burgers model is the fact that it exhibits a discrete relaxation spectrum (Mainardi and Spada, 2011), contrary to laboratory evidence.

Another interesting rheological model which shows transient behavior is that of Andrade. Its creep compliance reads:

$$J_a(t) = \frac{1}{\mu} + \beta t^{\alpha}\,, \quad t \geq 0\,, \tag{1.6}$$

where μ is the elastic rigidity, and α and β are empirical parameters. This model was conceived at the beginning of the previous century from the English physicist Edward Neville Andrade da Costa, in his attempt of describing deformation of metal wires under a constant tensile stress (Andrade, 1910). The "Andrade law" (1.6) is particularly appreciated for its elegance and conciseness, and its transient features are due to its fractional power function time dependence $\sim t^{\alpha}$.

The Andrade law has been successfully employed to describe the behavior of several materials, including metals (Cottrell and Aytekin, 1947), silicate rocks (Tan et al., 1997; Gribb and Cooper, 1998; Jackson and Faul, 2010), poly-crystalline ices (McCarthy and Castillo-Rogez, 2013), and glass forming materials (Plazek and Plazek, 2021). In his

empirical stress-strain relationship for the transient "β-flow", Andrade originally suggested the exponent $\alpha = 1/3$, but subsequent laboratory investigations have indicated that values in the range $0 < \alpha \leq 1$ are indeed possible for some materials (Walterová et al., 2023). Further studies (Mott, 1953; Cottrell, 1996; Louchet and Duval, 2009) have attempted to justify the Andrade power law theoretically; in particular, Cottrell (2004) has developed a microscopic theory that can explain, under certain conditions, the "$t^{\frac{1}{3}}$ law of flow" suggested by Andrade (1910, 1962).

During last decade, Andrade model has gained a lot of popularity in planetary science (see the review of Walterová et al. 2023). An exhaustive list of works employing Andrade model for the study of satellites and planets is given in Gevorgyan et al. (2020). The underlying reason of adopting the Andrade rheology for Earth-like planets relies upon the existence of a power law scaling for dissipation, recognized both in seismic studies and geodetic experiments (Efroimsky, 2012*b*). Furthermore, it has been preferred to the traditional non-transient Maxwell model, having the potential of capturing the inelasticity that characterizes high-frequency deformations, such as those caused by solid tides (Castillo-Rogez et al., 2011; Efroimsky, 2012*a*; Steinbrügge et al., 2018; Renaud and Henning, 2018; Bagheri et al., 2019; Tobie et al., 2019). Although Maxwell rheology is appropriate for describing the relaxation of a planet for forcing time scales of the order of or exceeding the Maxwell time (*i.e.,* the viscosity to shear modulus ratio), it largely underestimates viscosity when it is employed to describe tidal deformations (Bierson and Nimmo, 2016; Tobie et al., 2019; Walterová et al., 2023).

Nevertheless, a drawback that Andrade model inherits from the Maxwell one is the inability to distinguish between the relaxed and unrelaxed values of the elastic part of the deformation. To overcome this limitation, more general transient laws have been proposed, such as the one by Sundberg and Cooper (2010). Nonetheless, the advantage of the Andrade rheology consists in a reduced number of material parameters, which makes it more convenient for modeling the tidal response of inaccessible planets for

which few constraints (if any) on the internal structure are available, as pointed out by Padovan et al. (2014).

For these reasons, following a renewed interest for transient deformation in Glacial Isostatic Adjustment studies (Ivins et al., 2020; Adhikari et al., 2021; Simon et al., 2022; Lau, 2023; Paxman et al., 2023; Pan et al., 2024; Lau, 2024; Boughanemi and Mémin, 2024), I have adopted Andrade rheology for the study of post glacial rebound. The aim of the work presented here is a systematic investigation of the differences in the velocity fields generated by Earth models which include Andrade transient rheology, and others based upon the traditional Maxwell rheology. The ultimate goal is to outline a list of scenarios in which, through geodetic observations, the presence of a transient response should be easier to detect.

1.2 The surface loading problem and the sea level equation

The surface loading problem (SLP) constitutes the physical basis over which the modeling of Glacial Isostatic Adjustment (GIA) and Elastic Rebound (ER) are built. It is a classical problem of continuum mechanics, whose formalism was largely borrowed from tidal studies. From this scientific field indeed, the SLP adopts the formalism of the Love Numbers (LNs), adimensional coefficients first introduced by Love (1909) to describe the deformation of the Earth under a tidal potential.

Before the LNs formalism was introduced, the first attempts to describe the deformation of an elastic half-space stressed by an impulsive point load is attributed to Boussinesq (1885), who addressed this problem at the end of the XIX century (Fung, 1965; Peltier, 1974). In the scope of the "geoelastic" problems in linear elasticity, Boussinesq's one comes together with two other similar problems, *i.e.,* the Cerruti's problem (Cerruti, 1882), which considers the equilibrium of an elastic half-space perturbed by

a horizontal force (Okumura, 1995), and the Kelvin's problem (Thomson, 1848), where the point force is acting inside an infinite elastic space (Lubarda and Lubarda, 2020).

Within the framework of flat half-spaces, the first attempt of describing post glacial rebound was made by Haskell (1935, 1937). These studies represent pivotal works in GIA modeling: Haskell assessed for the first time the bulk viscosity of the Earth's mantle ($10^{21}\ Pa \cdot s$; see *e.g.*, Spada, 2017; Whitehouse, 2018), a milestone result in this field. Haskell model consists in a highly viscous incompressible half-space subject to a symmetrical load applied to its surface. He obtained his estimate by applying his model to the case of the of the Angerman River in Sweden, whose post-glacial uplift rates were known (Mitrovica, 1996).

As reported by Whitehouse (2018), when Haskell deduced its estimate of the Earth's bulk viscosity, the scope of GIA studies was at its beginning: several works were already published, but they repeatedly missed fundamental elements, like the Earth's deformation due to the ice loading or the water redistribution, feedback effects such as the gravity change following mass migration, and also the mass conservation. A complete and exhaustive historical review is given in Spada (2017) and Whitehouse (2018). Among these studies, the first one introducing a basic idea of the Sea Level Equation (SLE) was Woodward (1888), who recognized the importance of the gravitational attraction of the ice sheet upon ocean water distribution (see Spada and Stocchi, 2007). However, his work considered a rigid Earth therefore neglecting its deformation in response to surface loading or unloading (Whitehouse, 2018).

Almost one century later, the SLE was improved by the fundamental work of Farrell (1972) and its modern formulation that appeared in Farrell and Clark (1976). The SLE can be considered as the ultimate application of SLP to a self-gravitating, spherical and layered Earth, accounting for the mutual interaction between surface loads evolution (cryosphere and hydrosphere) and Earth's interior (geosphere). The work of Farrell and Clark is actually a further implementation of Longman's work of 1963, who, in turn,

derived the formalism and equilibrium equations from the theory of the free oscillation of the Earth (Alterman et al., 1959; Kaula, 1963).

The SL (S) is defined as the difference between the sea surface height change (N) and the solid Earth vertical displacement (U), always referred to the Earth's centre of mass:

$$S = N - U \ . \tag{1.7}$$

The SLE, which describes the variation in the SL between a time t and some reference time t_0, at a given location in (θ, λ), can be explicitly written as:

$$S(\theta,\lambda,t) = \frac{\rho_i}{\gamma} G_s \otimes_i I + \frac{\rho_w}{\gamma} G_s \otimes_o S - \frac{m_i(t)}{\rho_w A_o} - \frac{\rho_i}{\gamma}\overline{G_s \otimes_i I} - \frac{\rho_w}{\gamma}\overline{G_s \otimes_o S}\,, \tag{1.8}$$

(Farrell and Clark, 1976; Spada and Stocchi, 2006), where:

- $I(\theta, \lambda, t)$ is the variation of ice thickness relative to an initial reference state;
- ρ_i and ρ_w are ice and ocean water density, respectively, and γ is the reference gravity acceleration at the Earth's surface;
- G_s represents the Green's function describing the perturbations to the displacement field and the gravitational potential caused by an impulsive surface loading;
- symbols $\otimes_i$ and $\otimes_o$ denote spatiotemporal convolutions over the ice sheets and the surface of the oceans, respectively;
- the third term on the r.h.s. of the SLE is the *eustatic* term, which accounts for a spatially uniform sea-level variation, where A_o is the ocean area and $m_i(t)$ is the variation in ice mass;
- the overlines in the last two terms represent averages over the surface of the oceans, as required by the mass conservation principle.

The LNs h (vertical), k (potential) and l (horizontal) are hidden inside the the Green's functions representing the response of the Earth model to an impulsive load (Peltier, 1974; Spada and Stocchi, 2006). LNs are strictly connected to the Earth's internal structure, particularly to the number of layers and their rheology.

One of the most important characteristics of the SLE (1.8) is the fact that it is an integral (implicit) equation and thus iterative methods are necessary to solve it. However, the initial formulation of the SLE in Farrell and Clark (1976) presented several limitations, like the fact that it did not account for the temporal variation in ocean area and it did not include the rotational feedback on sea level (Whitehouse, 2018). These limitations were later addressed by a number of authors (see *e.g.,* Wu and Peltier, 1984; Johnston, 1993).

During the years, the research on GIA and SL modeling has progressed fast: from the classical pseudo-spectral approach, a range of different methods have been used, like finite-elements, spectral finite-elements, and finite-volumes; again, for a comprehensive review on the topic, the readers are referred to the work of Whitehouse (2018). However, the aim of this Thesis is not to present them systematically. Instead, for the purpose of this work, two points are still important to mention: the implementation of transient rheology in Earth models and the Elastic Rebound (ER). Regarding the first one, we refer the reader to the next section.

ER is the instantaneous elastic response of the Earth to surface loading (or unloading). ER is thus included in GIA, and represents the primary creep phase of the deformation of the Earth induced by the ice melting. The ER triggered by the intense changes at the end of the last glacial maximum 21 *kyr* ago has already been exhausted, giving way to the viscous response that still persists in previously glaciated areas of the Northern Hemisphere and adjacent regions. While it is assumed that the mantle flow is the principal engine of the viscous displacements, ER is caused by the elasticity of the outermost layers of the Earth, that produces an immediate response to the variation

of surface loads (Bevis et al., 2012). In the context of GIA modeling, the study of ER is particularly important when the areas of interest are still covered with ice: this is, for example, the case of Antarctica and Greenland. There, both the seasonal and net variation of the ice masses that we observe today induce an elastic displacement (ER) that superimposes on the viscous patterns caused by the past ice evolution. In several locations, indeed, the magnitudes these two contributions are comparable (Spada et al., 2012). Therefore, modeling ER in response to present-day variations of ice loads is essential to correctly infer GIA. For the sake of completeness, I shall specify that from now on in this Thesis, I will use the term "ER" to indicate the instantaneous displacement of the Earth's surface due to *present day* ice mass variation.

While for the case of seasonal (annual) variations in ice volumes the elastic response is undeniable, its validity on multidecadal forcing can be questioned. As it will be explained in the next section, present day climate change has triggered a negative trend in the mass balance of many glaciers and ice sheets around the world. In Greenland, this record is at least twenty years long (The IMBIE team, 2020), and even longer in certain locations. Basically, in this Thesis work, *we are asking how much truly "elastic" is the response of the solid Earth to current ice loss*, when observations span over timescales of decades. The next section treats this topic in detail.

A final fundamental remark on ER due to ice unloading concerns its typical spatial scales, definitively smaller than those of GIA. It is indeed a well known rule of thumb, in GIA studies, assuming that the spatial extent of the load is proportional both to the depth of the Earth's layers having more influence on the resulting surface displacement pattern, and on its spatial area of influence (McKenzie, 1967). In this way, we can consider the displacements due to GIA as long wavelength features, which is superimposed with short wavelength patterns caused by ER. This has important consequences upon ER modeling: it is shown indeed in Spada et al. (2012) that, for the modeling of ER in Greenland, a full solution of the SLE can be unnecessary. This is an important point for

this thesis, being the solution of the SLE rather expensive from a computational point of view, on a high resolution grid (see Spada and Melini, 2019). In this way, instead of evaluating the sea level variation S, we will consider the vertical displacement of the solid Earth U.

1.3 Greenland

1.3.1 Overview

The unprecedented rise in temperature during the latest 50 years is widely recognized as one of the major societal challenges of the 21st century (see *e.g.,* Ruane, 2024). From the solid Earth point of view, one of the main issues caused by climate change is the systematic variation in the spatial and time distribution of water masses, in their gaseous, solid, and liquid states. As we have anticipated in previous section, the solid Earth responds to the loads acting on its surface, including the atmosphere. What makes difficult the study of these mass redistributions is the complexity of the Earth system, and particularly the mutual interaction between each part of the system; atmosphere, cryosphere, hydrosphere, geosphere and biosphere. When a certain quantity of ice melts and migrates from the glacier to a water reservoir, that could be a lake, a sea or the ocean, the state of the Earth system changes, and each part reacts to retrieve the equilibrium. An example of non-linear interaction could be the melting of a marine-terminating glacier. During a warmer period, ocean and air temperatures rise, increasing the ice melting rate. As a consequence, the glacier melts and retreats, causing the elastic uplift of the Earth and the SL fall near the grounding line. Moreover, some studies suggest that the retreat of the ice from the ocean may stabilize the glacier, thus providing a negative feedback mechanism. (Gomez et al., 2015; Barletta et al., 2018).

Greenland hosts the second largest ice sheet on Earth, with an equivalent sea level potential of (7.42 ± 0.05) m (Morlighem et al., 2017). A recent study estimates that

Greenland ice sheet lost 3902 ± 342 billion tonnes of ice between 1992 and 2018, causing the mean SL to rise by (0.011 ± 0.001) m in the same time period (The IMBIE team, 2020). It is interesting to remark that this study reveals that half of this loss has occurred during the period between 2006-2012. In 2011, the ice loss reached the record of (345 ± 66) Gt/yr, but since then, the rate decreased, until reaching (85 ± 75) Gt/yr in 2018.

The stability of the ice sheet and its peripheral glaciers are subjects of particular interest among scientists, and many efforts have been made to understand its role in the Earth's climate system. The main mechanisms through which Greenland ice sheet loses ice are surface melt water runoff and all those phenomena which involve *ice dynamics*, like the acceleration of the marine-terminating glaciers, the retreat of the front line or the iceberg calving. According to King et al. (2020), the increasing ice discharge of the last twenty years is to be mainly attributed to the retreat of the glacier fronts that occurred at the beginning of the 2000s, that could have eventually unlocked a condition of sustained mass loss. The study of Choi et al. (2021) forecasts that by the end of the century, $50 \pm 20\%$ of the total mass loss will be caused by ice discharge from marine-terminating glaciers. Understanding the mechanisms through which glaciers and ice sheets lose and gain mass is fundamental to model the Earth response in a correct way.

There are different methods to assess the health condition of Greenland's ices. A powerful tool is the computation of the "Mass Balance" (MB), *i.e.,* the difference between the accumulated and ablated ice during a specific time period. To assess a MB, a number of techniques and methods have been proposed: satellite altimetry, interferometry, gravimetry, surface mass balance model simulation and input-output method. Each method has its pros and cons, and efforts to retrieve a reconciling value have been successfully carried on recently (Shepherd et al., 2012; Barletta et al., 2013; Khan et al., 2015; The IMBIE team, 2020).

1.3.2 Glacial isostatic adjustment and elastic rebound in Greenland

The interest that the GIA community nurtures towards Greenland is then easily motivated: with the exception of the elastic response caused by present-day ice melting, the rest of the world's largest island observed deformation shall be mainly attributed to GIA. Greenland is indeed considered a stable cratonic region, and its seismic activity is very low and confined on its margins (Olivieri and Spada, 2015). The sole hindrance to a systematic campaign to assess surface displacements in Greenland is its unique environment: the presence of the ice sheets and the prohibitive weather conditions make it difficult to install instrumentation. For this reason, satellite missions like GRACE or ICESat allowed an important step forward in the monitoring of the ice sheet. On land, the largest and most recent effort of deploying a network of GNSS stations is GNET. It comprises a total of 58 stations situated around Greenland's coasts (Bevis et al., 2012). The oldest one dates back to 1995, but the vast majority was installed during 2007-2009 (Barletta et al., 2024). GNET represents a powerful tool to investigate Greenland both from a glaciological and geodynamical point of view. For example, in Barletta et al. (2024), GNET data are used to obtain constraints to probe GIA models; its records are also used to validate elastic rebound and glacial isostatic adjustment models (Spada et al., 2012; Berg et al., 2024) and to monitor local glacier dynamics (Liu et al., 2017). In addition, the GIA community disposes of several tide gauge records, that besides their scarcity in the territory, provide long period time series (Spada et al., 2014). Finally, to complete the picture of available data, we must mention also geomorphological ones like Holocene SL Curves (Bennike et al., 2002; Long et al., 2011).

The final aim of every GIA model should be the comparison with the GNSS data. Hypothetically, if we knew the exact ice history, and if we knew the right viscosity structure of the Earth, then the prediction of the GIA model should coincide with the GNSS records, once every other additional signal has been removed. For the specific case of

Greenland, this means (generally) removing the elastic component, that part of the displacement due to present day ice mass loss. However, recent works have underlined that this procedure has been often underestimated: the PREM model has been the standard model for this procedure, although more realistic and suitable models nowadays exist (Adhikari et al., 2021); as demonstrated in Swarr et al. (2024), indeed, the choice of the wrong elastic model can lead to very significant differences in the predicted displacement; also, ignoring possible sources of inelasticity in the crust can be the cause of biased estimates (Durkin et al., 2019).

To remove the elastic component from the GNSS record, the standard procedure consists in computing the displacement due to an unloading ΔH that is supposed to happen *instantaneously*. The unloading model, when is referred to the entire Greenland ice sheet, is generally derived using data collected through different techniques like Synthetic Aperture Radar (SAR, see Rignot and Kanagaratnam, 2006), satellite gravimetry (GRACE and GRACE-FO, see Wahr et al., 1998; Barletta et al., 2013), or satellite altimetry (ICESat and ICESat2, see Schutz et al., 2005; Sørensen et al., 2011).

On the other hand, load models for GIA are built in a very different manner. Clearly, the uncertainties connected to past ice evolution are significant, and the methods used to infer it are indirect. Through geomorphological studies it is possible to recognize typical features generated by the presence of former ice sheets, and thus reconstruct the old ice extent and flow. To infer the past ice thickness instead, the main technique is cosmogenic exposure dating. Another method is inverting the GIA problem and considering the ice evolution as unknown, tuning the model to reconcile its output with low latitude SL records (Whitehouse, 2018). Examples of ice models used in GIA studies are ICE-5G and ICE-6G developed by the Toronto school (*e.g.,* Peltier, 2004) and the ANU models developed by the Australian National University (*e.g.,* Lambeck et al., 2014).

It is clear then that the resulting loading models for GIA and ER are extremely different in terms of resolution and associated uncertainties. As discussed in Pan et al.

(2024), it was the attempt to reconcile these two kinds of load models using a 1-layer mantle Earth model that set off the hypotheses of transient deformations in Greenland (Peltier et al., 1986). In those years, the hypothesis of transient features in the Earth's mantle response to GIA gained much popularity (Peltier et al., 1980; Sabadini et al., 1985; Müller, 1986; Yuen et al., 1986). However, it was (temporarily) abandoned once it was clear that the two types of ice models could lead to reconciling output if multilayered mantle models where taken into account. The mantle has indeed a different resolving power for the two models representing past and present-day ice evolution, because of the different spatial scale of the associated surface loading (Mitrovica, 1996; Pan et al., 2024). Nevertheless, in recent years, an interest on the topic arouse again, with an increasing number of scientific publications regarding this topic.

In Ivins et al. (2020) it is shown that, for the case of a Boussinesq's half space loading problem, the effects of transient rheology are relevant on the sub-decadal time scales. Adhikari et al. (2021) recognizes that on sub-centennial time scales, the inferred viscosity of the Earth mantle results one order of magnitude smaller than the upper mantle viscosity inferred from GIA. They show that a more realistic rheological model than the Maxwell one, combined with a more complete ice history that accounts also for recent events like the Little Ice Age are sufficient to explain the majority of data-model misfit, if a reduced mantle strength is considered. Similar conclusions were found by Boughanemi and Mémin (2024), who argue that assuming a low-viscosity layer in the upper mantle and using transient rheologies (Andrade and Burgers) can reduce the misfit between the modeled displacement and the observed data in Antarctica. Also, the need of transient rheology in surface unload modeling arises in local field studies, *i.e.,* in all those works where the distance between the observation point and the former load is small (Simon et al., 2022). All these studies prove that, when the time resolution of the ice history increases, *i.e.,* when the description of the ice evolution becomes infra-decadal, transient rheologies are invoked (and required), otherwise it is necessary to lower

the Maxwell viscosity of the model to fit the data (Nield et al., 2014; Pan et al., 2024).

Chapter 2

The Andrade's rheology

2.1 Transient rheologies

Part of the results presented in this Chapter are taken from Consorzi et al. (2024), published on Earth and Space Science (Sept, 2024).

In rheology, a "transient" is that phase of deformation where the strain rate exhibits time-dependent features, i.e. the strain rate is $\dot{\epsilon}(t) \neq const$. If we consider a purely elastic body, no transient occurs: the response to a stress is virtually instantaneous. However, the typical outcome of a cyclic test (periodic succession of loading and unloading phases) performed on a general poly-crystalline material exhibits a smoother transition, in which the instantaneous response is followed by a transient (and thus temporary) phase, that eventually precedes a stage of steady-state creep, if temperatures and pressure conditions are suitable (Ranalli, 1995). This situation is sketched in Figure 2.1. The transient phase, often referred to as *primary creep*, is the macroscopical manifestation of microscopical creep mechanisms, which involve the motion of the lattice defects such as dislocations or vacancies. As argued by Karato (2021), the transient phase in plastic deformation is the result of the strain dependency of both defects density and their distribution, which

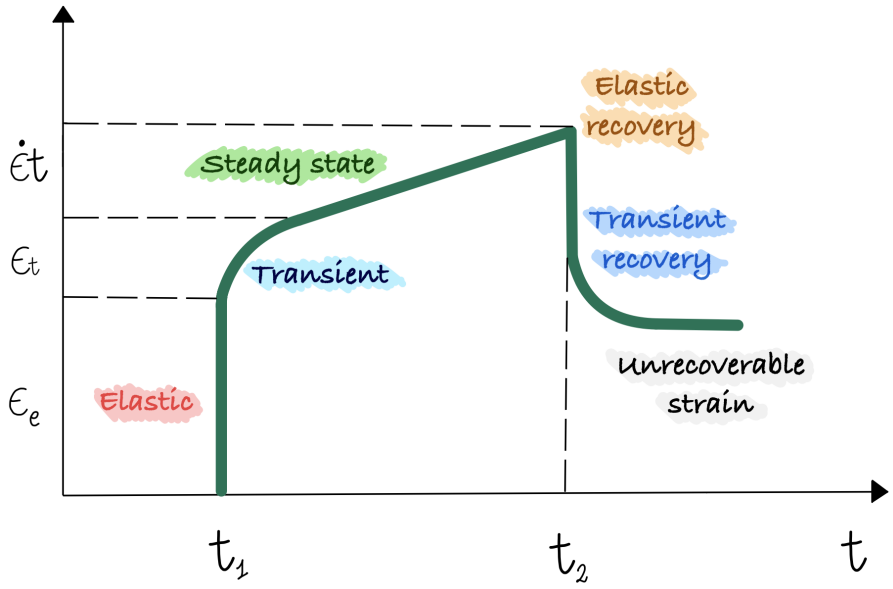

Figure 2.1: Sketched representation of creep in polycristalline materials (the figure is freely inspired to Ranalli 1995). The response is depicted in terms of strain $\epsilon(t)$ and it is assumed that a constant stress is applied between times $t = t_1$ and $t = t_2$ (*creep recovery test*).

in turn does not remain constant, but varies with the deformation.

At the beginning of the XX century, Andrade (1910) defined one of the first quantitative descriptions of deformation of metal and poly-crystalline materials at high temperature, studying the response of metal wires (Pb and Cu) under the application of tensile stresses. Andrade rheology, briefly introduced in the previous chapter (Eq. 1.6), will be studied in much greater detail in what follows. However, it represents just one of the many transient rheologies proposed: the time dependency of the transient varies from case to case, and each material has its own characteristics (Ranalli, 1995). Examples of other transient rheological models are:

- **Burgers model**: this model has seen vast applications in geophysics. Also known as bi-viscous model, it is the result of a series combination of a Maxwell element

with a Kelvin-Voigt element. The Burgers creep compliance, *i.e.,* the unit strain in response to the application of a unit stress, is:

$$J_B(t) = \frac{1}{\mu_M} + \frac{t}{\eta_M} + \frac{(1 - \mathrm{e}^{-\frac{t}{\tau_K}})}{\mu_K}\,, \qquad t \geq 0\,, \tag{2.1}$$

where μ_M and η_M are respectively the rigidity and viscosity of the Maxwell element, μ_K is the rigidity of the Kelvin-Voigt element, and τ_K is the ratio between the Kelvin-Voigt viscosity η_K and μ_K (retardation time).

- **Modified Lomnitz law**: a more general version of the Lomnitz law, proposed by Jeffreys and Crampin (1970). Originally conceived to describe deformation in fluid-like materials including igneous rocks, its creep compliance reads:

$$J_L(t) = J_0\,(1 + q\psi(t))\ , \quad t \geq 0\,, \tag{2.2}$$

where $q >$ is a dimensionless material constant and

$$\psi(t) = \frac{\left(1 + \frac{t}{\tau_0}\right)^{\alpha} - 1}{\alpha}\,. \tag{2.3}$$

In this model, the possible value of α, initially assumed in the range $0 \leq \alpha \leq 1$, was later extended to $\alpha \leq 1$ to yield a continuous transition from a linear elastic solid ($\alpha \to -\infty$), to a Maxwell body ($\alpha = 1$) (Mainardi and Spada, 2011).

- **Sundberg-Cooper model**: conceived by Sundberg and Cooper (2010) to address some drawbacks of the Andrade model, its creep compliance is:

$$J_{SC}(t) = \frac{1}{\mu} + \delta J(1 - \mathrm{e}^{-\frac{t}{\tau}}) + \beta t^{\alpha} + \frac{t}{\eta}\,, \quad t \geq 0\,, \tag{2.4}$$

where μ is rigidity, η is viscosity, α and β are the Andrade's parameters discussed in next section, δJ is the magnitude of the anelastic contribution, and τ is the time constant that governs the anelastic response (Bagheri et al., 2019).

There are several reasons for which, together with my supervisor, I decided to use the Andrade rheology to account for transient deformation: first, with respect to the Burgers model, it has less parameters; second, the planetary sciences community is not new to this rheology, which has been often employed to study tidal deformation of rocky planets; third, its simplicity makes it a more appealing model than the more complex Sundberg-Cooper and Lomnitz rheologies.

2.2 Material functions of the 1-D Andrade model

In the two subsections that follow I discuss the material functions of the 1-D Andrade model, namely the creep compliance $J_a(t)$ and the relaxation modulus $G_a(t)$. These two complementary quantities, related to ideal experiments, are fundamental to describe the behavior of any rheological model. The creep compliance represents the response of the body, in terms of strain, to the application of an instantaneous unit stress, kept constant afterwards; the relaxation modulus instead, is the stress response to the application of a stepwise unit strain.

2.2.1 Creep compliance

The creep compliance, that expresses the unit strain in response to the application of a unit stress, for the Andrade rheological law can be obtained from the original work of Andrade (1910) and reads:

$$J_a(t) = \frac{1}{\mu} + \beta t^{\alpha}\,, \quad t \geq 0\,, \tag{2.5}$$

where μ is the elastic shear modulus of the material, β is a parameter depending upon the sample properties and laboratory conditions and, according to Andrade's experiments, the time exponent is $\alpha = 1/3$. In subsequent laboratory investigations, values ranging between $\alpha = 0.2$ and $\alpha = 0.5$ have been suggested even for some non-metallic substances (see Walterová et al., 2023). Several attempts were made to explain Andrade's

parameters in terms of micro-physical processes (Cottrell and Aytekin, 1947; Mott, 1953; Louchet and Duval, 2009). In what follows, we will assume that α is expressed as a proper fraction $\alpha = p/q$, with p and q being integer numbers and $p < q$, which corresponds to $\alpha \in]0, 1]$.

In his treatise, Mainardi (2022) refers to Eq. (2.5) as a "fractional Maxwell model", since its mechanical analogue stems from the connection (in series) of a Hookean elastic element (a *spring*) of shear modulus μ with a Scott–Blair creep element characterized by a fractional power-law sometimes referred to as a *pot* (see Scott-Blair, 1951, 1970).

In modern applications to planets, the pure Andrade creep law expressed by Eq. (2.5) is generalized to account for a long-term steady state behaviour. This extension is performed by connecting a Newtonian element (a *dashpot*) in series with the elastic spring and the transient pot (Walterová et al., 2023). Accordingly, the complete form of the Andrade creep compliance reads:

$$J_a(t) = \frac{1}{\mu} + \beta t^\alpha + \frac{t}{\eta}\,, \quad t \geq 0\,, \tag{2.6}$$

where η is the Newtonian viscosity. To reduce the number of free parameters from four to three, Castillo-Rogez et al. (2011) proposed to define the β-factor as

$$\beta = \frac{\mu^{\alpha-1}}{\eta^\alpha}\,. \tag{2.7}$$

However, as pointed out by Walterová et al. (2023), the fractional dimension of the β-factor hinders the understanding of the physical meaning of (2.6). Therefore, it is more convenient to rewrite the creep compliance in the form

$$J_a(t) = \frac{1}{\mu}\left(1 + \left(\frac{t}{\tau_A}\right)^\alpha + \frac{t}{\tau_M}\right)\,, \quad t \geq 0\,, \tag{2.8}$$

where

$$\tau_M = \frac{\eta}{\mu} \tag{2.9}$$

is the "Maxwell time", *i.e.*, the characteristic timescale on which steady-state behavior occurs, while

$$\tau_A = (\beta\mu)^{-\frac{1}{\alpha}} \tag{2.10}$$

is the "Andrade time" *i.e.,* the transient response timescale. Efroimsky (2012*a*,*b*) introduced the non-dimensional ratio:

$$\zeta = \frac{\tau_A}{\tau_M}\,, \tag{2.11}$$

which allows to cast the Andrade creep law in the so called "$\alpha - \zeta$ parameterization"

$$J_a(t) = \frac{1}{\mu}\left(1 + \zeta^{-\alpha}\left(\frac{t}{\tau_M}\right)^{\alpha} + \frac{t}{\tau_M}\right)\,, \quad t \geq 0\,, \tag{2.12}$$

with $J_a(t)$ reducing to the Maxwellian creep compliance in the limit $\zeta \to \infty$ (*i.e.*, for an infinite Andrade time τ_A).

As pointed out by Castillo-Rogez et al. (2011) in their study about the tidal history of Iapetus, the constraint $\beta = \frac{\mu^{\alpha-1}}{\eta^{\alpha}}$ or, equivalently, $\zeta \approx 1$, should be regarded as a first-order approximation, awaiting for laboratory data of sufficient quality. Nowadays, the approximation $\zeta \approx 1$ is generally considered as outdated, with plausible values of ζ ranging between 10^{-2} and 1, although values as high as 10^5 have been shown to be consistent with the tidal response of the Earth (Walterová et al., 2023; Amorim and Gudkova, 2024).

In Figure 2.2a, the Andrade creep compliance $J_a(t)$ is shown as a function of the normalized time t/τ_M, for different values of $\alpha = 1/n$, where n is an integer, and $\zeta = 1$ is assumed. The original Andrade result ($n = 3$, or $\alpha = 1/3$) is depicted by a turquoise curve. The time scale characterizing the transient phase (*i.e.,* the time required to reach a constant creep rate) decreases with increasing n. For $\alpha = 1$, no transient occurs after the elastic step at $t = 0$, and the response is Maxwellian. In this case, the transient term in (2.12) duplicates the steady-state term, hence the response is that of a Maxwell body with Newtonian viscosity $\eta/2$. Figure 2.2b depicts $J_a(t)$ for different values of parameter

ζ, keeping the fractional exponent fixed to $\alpha = 1/3$. As expected from its definition, the value of ζ controls the relative importance of the steady-state and transient terms in (2.12), with large values of ζ producing a response increasingly similar to the Maxwellian one. Here the original Andrade result is represented by the orange curve.

The Laplace transform of the Andrade creep law (2.12) can be obtained by elementary methods and it reads

$$\tilde{J}_a(s) = \frac{1}{\mu\, s}\left(1 + \frac{\Gamma(1+\alpha)}{(\zeta\tau_M s)^\alpha} + \frac{1}{s\tau_M}\right), \tag{2.13}$$

where s is the complex Laplace variable and $\Gamma(x)$ is Euler's gamma function.

2.2.2 Relaxation modulus

To fully characterize the rheological behaviour of the Andrade model, it is also desirable to obtain the relaxation modulus $G_a(t)$, which physically represents the stress per unit strain in a relaxation experiment (Christensen, 1982). In the time domain, the relaxation modulus $G(t)$ of a general linear viscoelastic material is related with the creep compliance $J(t)$ through $J(t) * G(t) = t$, where $*$ denotes time-convolution (Mainardi, 2022). In the Laplace domain, this relation reads $\tilde{J}(s)\,\tilde{G}(s) = 1/s^2$, hence $s\,\tilde{G}_a(s) = 1/(s\tilde{J}_a(s))$. Therefore, using (2.13), the Laplace-transformed relaxation modulus is easily obtained:

$$\tilde{G}_a(s) = \frac{\mu\tau_M}{(s\tau_M) + \zeta^{-\alpha}\Gamma(1+\alpha)(s\tau_M)^{1-\alpha} + 1}\,. \tag{2.14}$$

Evaluating the Laplace inverse of Eq. (2.14) analytically is not straightforward. This issue challenged me for a while. In my master thesis (Consorzi, 2021) I briefly addressed the problem, without finding any elegant solution. Following the advice of my supervisor, I tackled again this topic during my PhD. With the help of *Mathematica©* symbolic manipulator (Wolfram Research, Inc., 2024), and after several attempts I finally managed to retrieve an analytical, still not elementary, expression (Eq. 2.23 below). As far as I know, this was an original and unpublished result. Once *Mathematica©* assured the

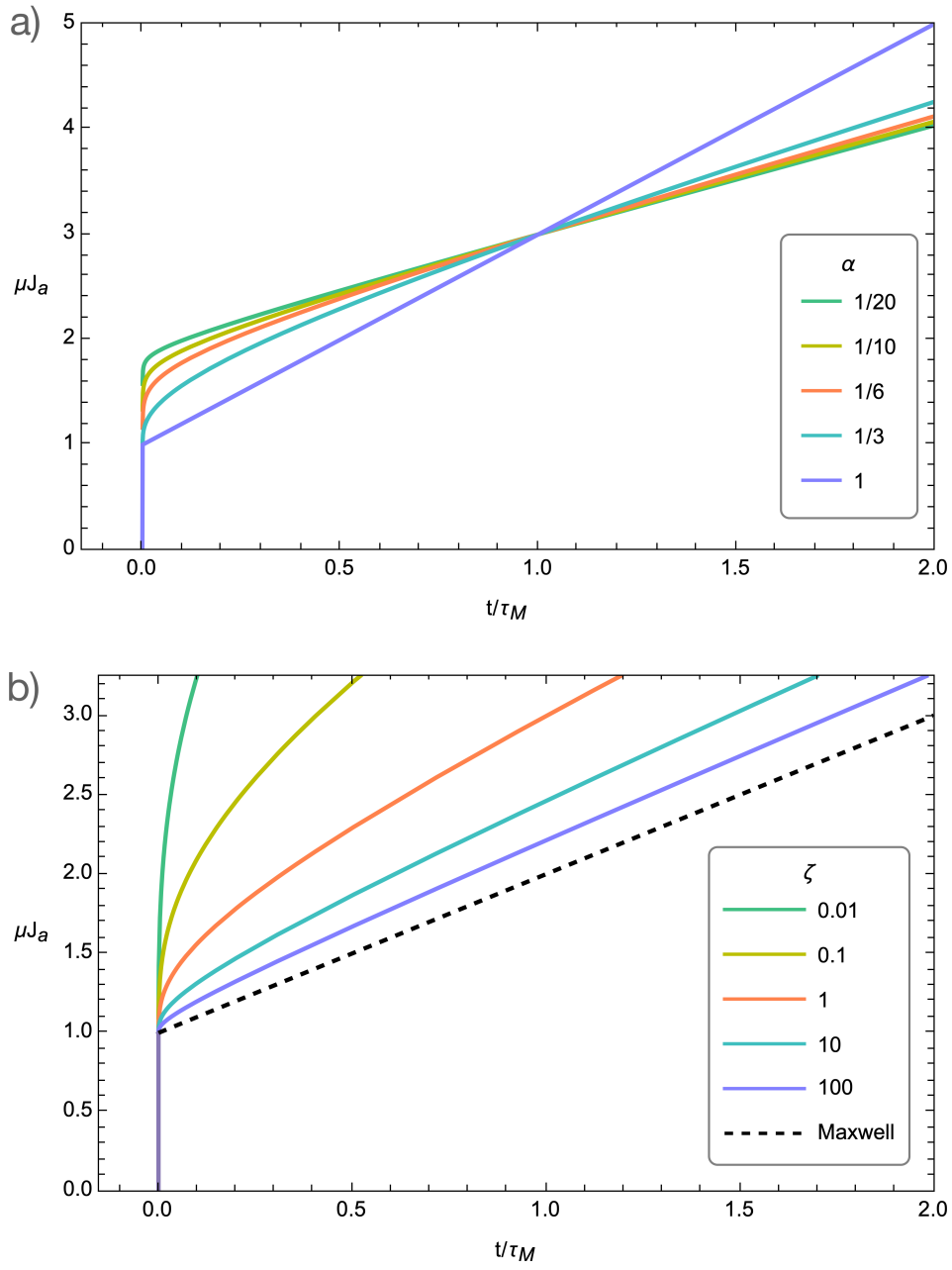

Figure 2.2: Andrade creep compliance $J_a(t)$, according to Eq. (2.12). In (a), $J_a(t)$ is shown for ζ=1 and $\alpha = 1/n$ (n=1, 3, 6, 10, 20), while in (b) α is set to 1/3 and different values of parameter ζ=τ_A/τ_M are considered, as indicated. The Maxwell response is attained for $\zeta \to \infty$.

existence of a closed-form solution, the new task was understanding how to gather it analytically. After some quick consultations, Prof. F. Mainardi perceived some formal analogies between this problem and the generalized Basset problem that concerns the motion of a particle within a viscous fluid. Some attempts later, following the method used in Mainardi et al. (1995), I finally managed to close the circle. Afterward, my computations were checked and published by other authors in (González-Santander et al., 2024). However, in what follows, I will present the details of this calculation.

Computation of the Andrade relaxation Modulus in the time domain

The main hindrance for the Laplace inversion of expression (2.14) is the presence of the fractional exponent α. To overcome this problem, I followed the strategy presented in (Mainardi et al., 1995), and I operated a change of variable $s\tau_M \to x^q$, where we recall that q is related to the definition of α as proper a fraction, namely $\alpha = \frac{p}{q}$, $p < q$. In this way, one obtains an expression for $\tilde{G}_a$ that does not contain any fractional exponents:

$$\tilde{G}_a(x) = \frac{\mu\tau_M}{x^q + \zeta^{-\alpha}\Gamma(1+\alpha)(x)^{q-p} + 1}\,. \tag{2.15}$$

Then, recognizing that the denominator $P_{p,q}(x)$ of Eq. (2.15) is a polynomial of degree q (shown in Figure 2.3), and naming x_k its roots,

$$P_{p,q}(x_k) = x_k^q + \zeta^{-\alpha}\Gamma(1+\alpha)(x_k)^{q-p} + 1 = 0\,, \tag{2.16}$$

it is possible to write $P_{p,q}(x)$ using the partial fraction decomposition method:

$$\frac{1}{P_{p,q}(x)} = \sum_{k=1}^{q} \frac{1}{P'_{p,q}(x_k)(x - x_k)} \tag{2.17}$$

where $P'_{p,q}$ is the derivative of $P_{p,q}$ with respect to x. In this way, the relaxation modulus can be written as:

$$\tilde{G}_a(x) = \mu\tau_M \sum_{k=1}^{q} \frac{1}{(qx_k^{q-1} + (q-p)\zeta^{-\alpha}\Gamma(1+\alpha)x_k^{q-p-1})(x - x_k)} \tag{2.18}$$

$$= \mu\tau_M \sum_{k=1}^{q} \frac{1}{P'_{p,q}(x_k)(x - x_k)}\,. \tag{2.19}$$

Now we can come back to the variable $s\tau_M$, obtaining:

$$\tilde{G}_a(s) = \mu\tau_M \sum_{k=1}^{q} \frac{1}{P'_{p,q}(x_k)((s\tau_M)^{\frac{1}{q}} - x_k)} \,. \tag{2.20}$$

In this form, the computation of the inverse transform turns out to be easier. We use the relation (E.53) from Mainardi (2022):

$$\mathcal{L}^{-1}\left[\frac{s^{\alpha-\beta}}{s^\alpha + \lambda}; t\right] = t^{\beta-1} E_{\alpha,\beta}\left(-\lambda t^\alpha\right) \,, \tag{2.21}$$

where

$$E_{\alpha,\beta}(z) \equiv \sum_{k=0}^{\infty} \frac{z^k}{\Gamma(\alpha k + \beta)} \,, \quad \text{with} \quad \alpha, \beta \in \mathbb{C},\, \mathrm{Re}(\alpha) > 0,\, z \in \mathbb{C} \,, \tag{2.22}$$

is the two-parameter Mittag-Leffler transcendental function (Mittag-Leffler, 1903), whose properties and fields of application are now well known (Mainardi, 2020; Gorenflo et al., 2020). The Mittag-Leffler function is considered the "Queen function" of fractional calculus (Gorenflo et al., 2020; Mainardi, 2020), given its crucial role in the field of linear viscoelasticity.

Considering that in this case $\alpha = \beta = 1/q$ and $\lambda = -x_k$, I obtained, making explicit the terms of $P'_{p,q}(x)$, one of the main results of this thesis:

$$G_a(t) = \frac{\mu}{\left(\dfrac{t}{\tau_M}\right)^{1-\frac{1}{q}}} \sum_{k=1}^{q} \left(\frac{E_{\frac{1}{q},\frac{1}{q}}\left(x_k \left(\dfrac{t}{\tau_M}\right)^{\frac{1}{q}}\right)}{q\, x_k^{q-1} + \frac{q-p}{\zeta^{p/q}}\, \Gamma\left(\dfrac{p}{q} + 1\right) x_k^{q-p-1}} \right) \,, \quad t \geq 0 \,, \tag{2.23}$$

Note that although some of the x_k's are complex, the properties of the Mittag-Leffler function ensure that in Eq. (2.23) the relaxation modulus $G_a(t)$ is a real function. Note also that, for $\zeta \gg 1$ (*i.e.* for $\tau_A \gg \tau_M$), the roots of polynomial (2.16) can be approximated by $x_k \approx e^{i(2k-1)\pi/q}$ for $k = 1, \ldots, q$. The result (2.23) is reported in Consorzi et al. (2024).

It is important to remark that, for the Andrade law in the fundamental form given by (1.6), the relaxation modulus can be expressed in terms of the classical (one index)

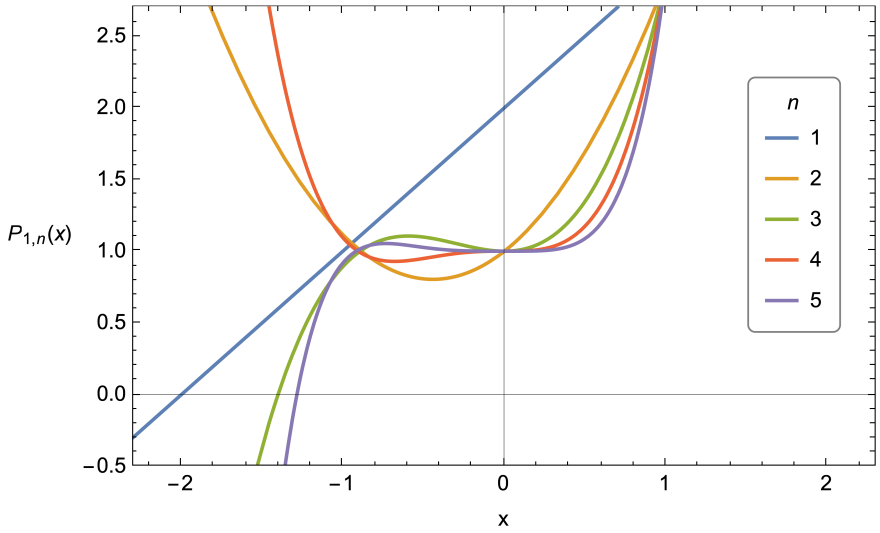

Figure 2.3: Plot of the $P_{1,n}(x)$ polynomial defined by Eq. (2.16), for some n values and ζ=1. One real and negative root is only found for odd values of n, as we have also verified for $n > 5$. For n=3, the value suggested by the original work of Andrade (1910), the three roots of the polynomial are $r_1 \approx -1.401$ and $r_{2,3} \approx (0.254 \pm i\,0.805)$.

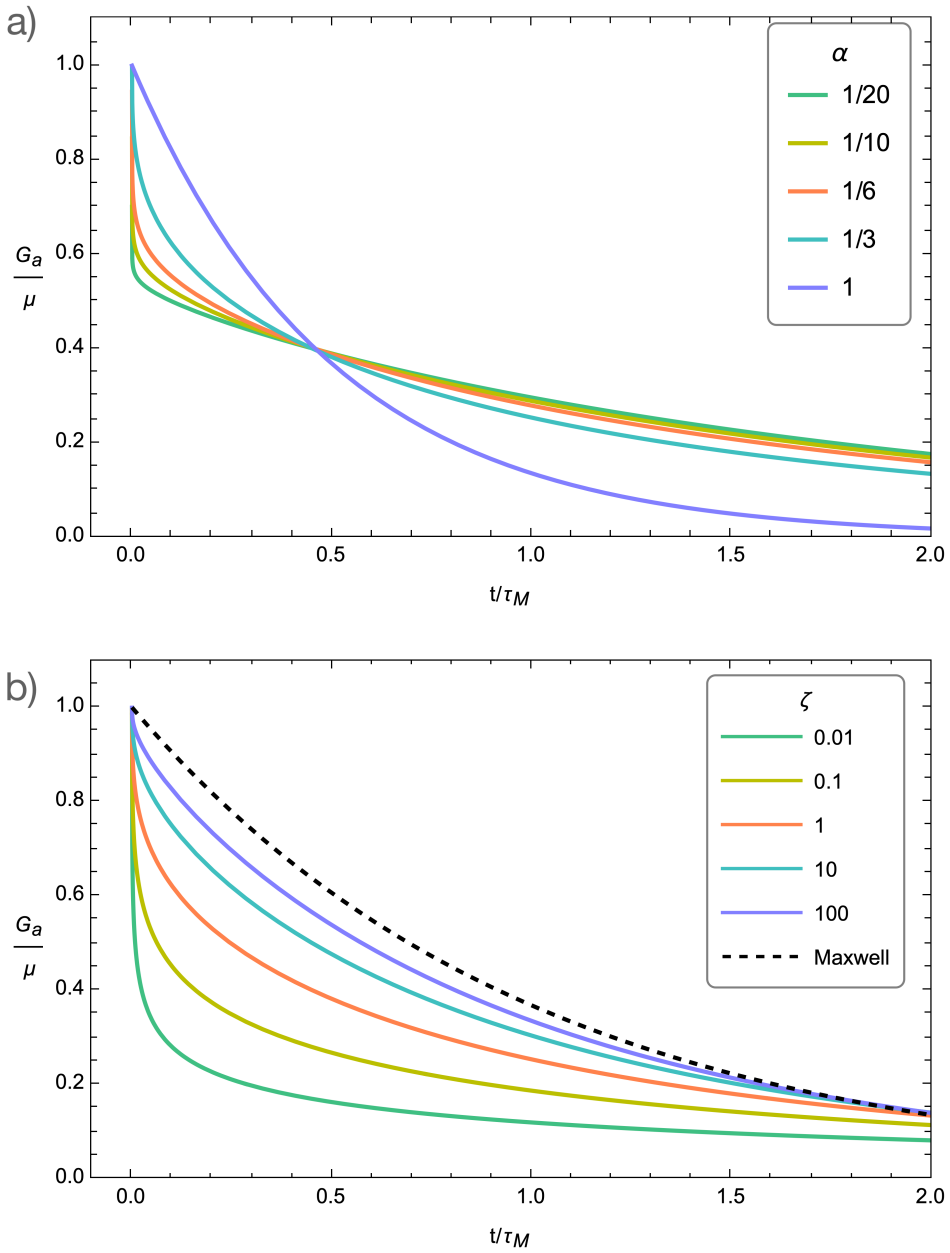

Figure 2.4: Relaxation modulus $G_a(t)$ for an Andrade body, according to Eq. (2.23). In (a), ζ=1 and α=1/n are assumed (n=1, 3, 6, 10, 20). For n=1 the decay is exponential, since $E_{1,1}(-x)$=e^{-x}. In (b), the modulus is shown for $\alpha = 1/3$, using different values of the ratio $\zeta = \tau_A/\tau_M$. The Maxwell case (dashed black) corresponds to $\zeta \to \infty$.

Mittag-Leffler transcendental function defined as $E_\alpha(z) = E_{\alpha,1}(z)$. Therefore, the result expressed by Eq. (2.23) can be considered as an extension of the previous findings of Mainardi and Spada (2011) to the case of the generalized Andrade model expressed by (2.8).

The Andrade relaxation modulus $G_a(t)$ in (2.23) is shown for $\zeta = 1$ in Figure 2.4a as a function of the normalized time t/τ_M, in the special case $\alpha = 1/n$ with $n = 1, \ldots, 5$; Figure 2.4b shows again the relaxation modulus but for a fixed $\alpha = 1/3$ and various values of ζ. From this figure it is apparent that, as expected, the relaxation modulus converges to that of a Maxwell solid as $\zeta \to \infty$ (black dashed curve). These figures include the original Andrade result, depicted by a turquoise curve in Figure 2.4a and by a orange one in Figure 2.4b.

In the next section, I will briefly examine some limiting cases of the expression of the Andrade relaxation modulus in the time domain Eq. (2.23).

2.2.3 Limiting cases of the Andrade relaxation modulus

In the following, I present the details of the computation of two notable limits of the Andrade relaxation modulus.

Case 1: $\zeta \to \infty$

Is it possible to foresee from Figure 2.4 that with increasing values of ζ, the behaviour of Equation (2.23) tends to those of the relaxation modulus of a Maxwell body. I checked graphically that this holds true for arbitrary values of p and q, as long as $p < q$ and both are integers.

To prove that, in the limit $\zeta \to \infty$, the Andrade relaxation modulus is equivalent to the Maxwell one, we must start considering which form assume the roots of the

polynomial $P_{p,q}$ in the aforementioned case. Being

$$\lim_{\zeta\to\infty} P_{p,q}(x) \equiv \lim_{\zeta\to\infty} F_q(x) = x^q + 1\,, \tag{2.24}$$

we can write the roots of Eq. (2.24) in the following way:

$$x_k = e^{\frac{i\pi(2k-1)}{q}} \quad k = 1, ...q\,. \tag{2.25}$$

Then, in the Maxwell limit $\zeta \to \infty$, Eq. (2.23) can be recast in the form:

$$\lim_{\zeta\to\infty} G_a(t) = \frac{\mu}{q} \underbrace{\frac{1}{\left(\frac{t}{\tau_M}\right)^{1-\frac{1}{q}}} \sum_{k=1}^{q} \left(\frac{E_{\frac{1}{q},\frac{1}{q}}\left(\left(\frac{t}{\tau_M}\right)^{\frac{1}{q}} x_k\right)}{x_k^{q-1}} \right)}_{\Delta_q(t)}\,. \tag{2.26}$$

Performing the Laplace-transform of $\Delta_q(t)$ and substituting the x_k's with their explicit values (2.25), it is possible to show that the following relation holds true:

$$\mathcal{L}\left[\Delta_q(t)\right] = \tilde{\Delta}_q(s) = \sum_{k=1}^{q} \frac{x_k^{1-q}}{(s\tau_M)^{1/q} - x_k} = \frac{q}{s\tau_M + 1}\,. \tag{2.27}$$

The demonstration of this last statement requires some work.

First of all, I start defining the index $k = h + 1$, so that the roots x_k may be recast in the following form:

$$x_{h+1} = (-1)^{1/q} e^{2\pi i h/q}\,, \tag{2.28}$$

from which, it follows that

$$x_{h+1}^{1-q} = (-1)^{(1-q)/q} e^{2\pi i h/q} e^{-2\pi i h}\,. \tag{2.29}$$

Thus, I obtain

$$\tilde{\Delta}_q(s) = \sum_{h=0}^{q-1} \frac{(-1)^{(1-q)/q} e^{2\pi i h/q} e^{-2\pi i h}}{(s\tau_M)^{1/q} - (-1)^{1/q} e^{2\pi i h/q}}\,, \tag{2.30}$$

which, with a little algebra, can be simplified in the following expression:

$$\tilde{\Delta}_q(\sigma) = -\sum_{h=0}^{q-1} \frac{e^{2\pi i h/q}}{\sigma^{1/q} - e^{2\pi i h/q}}\,, \tag{2.31}$$

where I have abbreviated $\sigma = (-s\tau_M)$. To better explain what follows, I consider the particular case $q = 2$. By developing each term of the sum, one finds:

$$\begin{aligned}
\tilde{\Delta}_q(\sigma) &= -\left[\frac{1}{-1+\sigma^{1/2}} - \frac{1}{1+\sigma^{1/2}}\right] \\
&= -\left[\frac{1}{-1+\sigma^{1/2}}\left(\frac{1+\sigma^{1/2}}{1+\sigma^{1/2}}\right) - \frac{1}{1+\sigma^{1/2}}\left(\frac{-1+\sigma^{1/2}}{-1+\sigma^{1/2}}\right)\right] \\
&= -\frac{1+\sigma^{1/2}+1-\sigma^{1/2}}{-1+(-s\tau_M)} \\
&= \frac{2}{s\tau_M+1}
\end{aligned} \tag{2.32}$$

which is exactly what we want to demonstrate, if we assume $q = 2$. By employing the same procedure for any generic q, that is, by multiplying each element of the sum for a suitable dummy term, one finds:

$$\tilde{\Delta}_q(\sigma) = -\frac{e^{2\pi i q h/q}\sigma^{\frac{0}{q}} + e^{2\pi i(q-1)h/q}s^{*1/q} + \ldots + e^{2\pi i(q-(q-1))h/q}\sigma^{(q-1)/q}}{-e^{2\pi i q h/q} + \sigma^{q/q}}\,. \tag{2.33}$$

Now, to continue, in view of what I have just shown in Eq. (2.33), I re-write the sum in Eq. (2.31) as:

$$\begin{aligned}
\tilde{\Delta}_q(\sigma) &= -\sum_{h=0}^{q-1} \frac{e^{2\pi i h/q}}{\sigma^{1/q} - e^{2\pi i h/q}} \\
&= -\sum_{h=0}^{q-1}\sum_{l=0}^{q-1} \frac{e^{2\pi i(q-l)h/q}\sigma^{l/q}}{e^{2\pi i h} + \sigma} \\
&= -\frac{1}{\sigma-1}\sum_{h=0}^{q-1}\sum_{l=0}^{q-1} e^{2\pi i l h/q}\sigma^{l/q}\,.
\end{aligned} \tag{2.34}$$

Since l ranges from 0 to $q-1$, by virtue of the identity

$$\sum_{h=0}^{q-1} e^{2\pi i h l/q} = \begin{cases} q & \text{if} \quad l = 0 \\ 0 & \text{if} \quad l \neq 0 \end{cases} \tag{2.35}$$

(see Mainardi (2022), Eq. E10), we can write:

$$\begin{aligned}\tilde{\Delta}_q(s) &= -\frac{1}{\sigma-1}\sum_{h=0}^{q-1}\sum_{l=0}^{q-1} e^{2\pi i l h/q}\sigma^{l/q} \\ &= -\frac{1}{\sigma-1} q\sigma^{0/q} \\ &= \frac{q}{s\tau_M+1}\,.\end{aligned} \tag{2.36}$$

Now that we have concluded this demonstration, from Eq. (2.27), it is straightforward to transform back to the time domain $\tilde{\Delta}_q(s)$:

$$\mathcal{L}^{-1}\left[\tilde{\Delta}_q(s)\right] = q e^{-\frac{t}{\tau_M}}\,, \tag{2.37}$$

that, inserted into Eq. (2.26) gives exactly the expression of the relaxation modulus of a Maxwell body

$$G_M(t) = \mu e^{-\frac{t}{\tau_M}}\,. \tag{2.38}$$

Case 2: $\alpha \to 1$

For the limiting case $\alpha \to 1$, inspecting the definition of the Andrade creep compliance (2.5), the final result I expect is the Maxwell relaxation modulus of a body with viscosity $\eta/2$. The case $\alpha \to 1$ includes the simplified case $(p,q) \to 1$ but also the more general one $p \to q$. I shall start with the first one, being the simplest to analyse.

If $(p,q) \to 1$, the relaxation modulus (2.23) assumes the form:

$$\lim_{(p,q)\to(1,1)} G_a(t) = \mu E_{1,1}\left(x_1\left(\frac{t}{\tau_M}\right)\right)\,, \tag{2.39}$$

with

$$x_1 = -\left(1+\frac{\Gamma(2)}{\zeta^{-1}}\right) = -\frac{1+\zeta}{\zeta}\,. \tag{2.40}$$

Using the properties of the Mittag-Leffler function we have:

$$G_a(t) = \mu e^{-\frac{1+\zeta}{\zeta}\left(\frac{t}{\tau_M}\right)}\,, \tag{2.41}$$

and finally, since for a Maxwell body $\tau_A = \tau_M \Rightarrow \zeta = 1$, I obtain:

$$G_a(t) = \mu e^{-2\left(\frac{t}{\tau_M}\right)} = \mu e^{-\left(\frac{t}{\eta/2\mu}\right)} . \tag{2.42}$$

If instead we impose only $p \to q$, we would find a situation very similar to that of **case 1** (previous paragraph, $\zeta \to \infty$), with the only difference that, in this limit, the polynomial $P_{p,q}(x)$ becomes:

$$P_{p,q}(x) = x^q + \frac{\Gamma(2)}{\zeta} + 1 = x^q + \frac{1+\zeta}{\zeta} , \tag{2.43}$$

and thus its roots x_k will be, considering that $\zeta = 1$.

$$x_k = 2e^{\frac{i\pi(2k-1)}{q}} \quad k = 1, ..., q , \tag{2.44}$$

Except for this difference, the rest of the calculation is basically the same.

These further computations support the validity of the result expressed in Eq. (2.23), which correctly reproduces a Maxwell (or Maxwell-like) behaviour under particular conditions of the parameters α and ζ.

Chapter 3

Love Numbers

A part of this Chapter, Section 3.4, largely follows Consorzi et al. (2023), published on Astronomy & Astrophysics in August 2023.

The *Love numbers* are coefficients first introduced by Love (1909) in the context of tidal deformation. A. E. H. Love was a British mathematician who produced, during his brilliant career, a number of works of fundamental importance for the theory of elasticity: we owe to him the mathematical description of the surface "Love" waves, the introduction of the Love strain function (Love, 2013) and, of course, Love numbers (LNs). LNs have been a central topic in my work, since they contain most of the information about the way in which a planetary body can be deformed by the effect of external potentials or surface loads.

The idea behind LNs consists of a simple *ansatz*. Let's consider the simplest case, a homogeneous spherical planet whose gravitational potential is perturbed by the presence of an external body (a parent star, or another planet). The total perturbation to the gravitational potential, evaluated at the surface of the planet, must be the sum of two contributions: a direct potential ϕ_0, and an indirect one ϕ', due to the planet

readjustment in response to the external forcing:

$$\phi_{tot} = \phi_0 + \phi'. \tag{3.1}$$

Love supposed that since the tidal deformation can be considered small, then the indirect potential should be proportional to the direct one:

$$\phi' = K(r)\phi_0 \tag{3.2}$$

so that

$$\phi_{tot} = (1 + K(r))\phi_0\,, \tag{3.3}$$

where $K(r)$ is a function of the radius r. Considering the geometry of the problem, it is convenient to switch to a description in spherical harmonics. Hence, the proportionality that Love assumed, applies to each coefficient of the series

$$\phi_{tot} = \sum_{n=0}^{\infty} (1 + K_n(r))\, \phi_{0,n}\,, \tag{3.4}$$

where, if a is the radius of the planet, then the value $K_n(a) = k_n$ is the LN of degree n for the gravitational potential.

Love applied the same strategy to the study of the vertical component of the displacements induced by a tidal perturbation, defining the h_n LN:

$$U_n = -h_n \frac{\phi_0}{g_0}\,, \tag{3.5}$$

where g_0 is the reference gravity acceleration at the surface ($r = a$). Later, T. Shida in 1912, introduced the LN l_n describing the horizontal component of the displacement:

$$V_n = -l_n \frac{\phi_0}{g_0}\,. \tag{3.6}$$

Later, the formalism of LNs was applied to the study of deformations induced by surface loads, and a new class of LN was introduced, often referred to as Load Deformation

Coefficients, or **Load** LNs. The only difference between the tidal (or **potential**) LNs and the load LNs lies in the definition of the boundary conditions, in which the latter include the term of the normal stress that, instead, is missing in the former (Farrell, 1972).

3.1 Love Numbers in the modeling of planetary interiors

The use of LNs is not limited to the study of the Earth. They have been largely employed in Planetary Science for the study of other planets of the Solar System. Moreover, recent works suggest that the study of transit light curves of extra-solar planets may provide information upon the value of their second degree fluid LN k_2 (Carter and Winn, 2010; Correia, 2014; Kellermann et al., 2018; Hellard et al., 2018, 2019; Akinsanmi et al., 2019; Barros et al., 2022). According to Padovan et al. (2018), estimates of k_2 for extra-solar planets may become available in the near future, in view of the expected improvements in the observational facilities and the increasing amount of data. Since the k_2 LN of a giant fluid-like planet is sensitive to the density layering (Ragozzine and Wolf, 2009; Kramm et al., 2011; Padovan et al., 2018), transit observations may potentially provide, in the upcoming years, new constraints on the internal structure of exoplanets. These will have important implications upon our knowledge of the internal planetary dynamics and the formation history (Kramm et al., 2011).

Similar motivations encouraged me to consider also the case of rocky planets: it is not necessary to invoke the case of exoplanets to dispose of many case studies still poorly examined. This is the case, for example, of the moons and minor satellites that populate the planetary systems of Uranus and Neptune, which, up to now, have been the target of only one mission, Voyager 2, respectively in 1986 and 1989. These systems, particularly Uranus, include several satellites which are considered good candidates for hosting liquid

water. The presence (or absence) of deep oceans can be inferred from the values of the k_2 LN and the quality factor Q (Castillo-Rogez et al., 2023), making once again the observation of these parameters a goal of uppermost importance.

For these reasons, I delved into the study of LNs, with a strong focus on three scenarios: the first, presented in Section 3.2, shows the calculation of LNs for a homogeneous sphere (Kelvin model); this first case is of great importance, since, in view of the *Correspondence Principle*, its results can be extended to investigate other linear viscoelastic rheologies (Section 3.3). The second case, in Section 3.4, concerns layered inviscid fluid planets, a perfect first-order approximation for gas giants. In this section I further investigate the possibility of an analytical relation between the k_2 LN and the moment of inertia N. Lastly, in Section 3.5, I consider a Kelvin model with Andrade rheology, whose versatility has already been described in the previous chapters. The models presented in this chapter, despite their simple structure (homogeneous, two-layer), have the advantage of allowing for a full analytical investigation. This fact is noteworthy, since it often permits to identify explicitly the relations between the LNs and each model parameter.

3.2 Love Numbers for the elastic Kelvin model

In this section I will present the computation of the LNs of an elastic Kelvin sphere (*i.e.,* an homogeneous, self-gravitating sphere). Here I would like to stress out that the calculations that will follow in this section 3.2 and the next 3.3 are not original, and for further details the reader is referred to Spada (1992) and Martens (2016). They are reported here for completeness and to ease the comprehension of the calculations that follows, the discussion on Love number and the results presented in the last chapter.

Let's start from the equation of motion for an elastic medium, which reads:

$$\boldsymbol{F} + \nabla \cdot \boldsymbol{T} = \rho \ddot{\boldsymbol{u}}\,, \tag{3.7}$$

where $\boldsymbol{F}$ is the sum of all the volume forces acting on the body, $\boldsymbol{T}$ is the stress tensor

and $\boldsymbol{u}$ is the displacement field. If we limit our analysis to quasi-static (*i.e.*, very slow) deformations, we can neglect the acceleration:

$$\boldsymbol{F} + \nabla \cdot \mathbf{T} = 0\,, \tag{3.8}$$

and we can define $\boldsymbol{T}$ as

$$\mathbf{T} = -p\mathbf{I} + \mathbf{T}^*\,, \tag{3.9}$$

with p and $\boldsymbol{T}^*$ being the pressure and the non-hydrostatic part of the stress tensor. In this dissertation, the only volume force we consider is that associated to the gravitational potential ϕ:

$$\boldsymbol{F} = -\rho\nabla\phi\,, \tag{3.10}$$

where we notice that

$$\boldsymbol{g} = -\nabla\phi \tag{3.11}$$

is gravity acceleration. In addition, the gravitational potential ϕ is a solution of Poisson's equation

$$\nabla^2\phi = 4\pi G\rho\,, \tag{3.12}$$

where G is the universal gravitational constant. Since at the equilibrium state, we assume a condition of perfect hydrostatic equilibrium, we have the following fundamental system of equations:

$$\begin{cases} \mathbf{F}_0 = -\rho_0\nabla\phi_0 & \text{Volume force} \\ \mathbf{T}_0 = -p_0\mathbf{I} & \text{Stress Tensor} \\ \nabla^2\phi_0 = 4\pi G\rho_0 & \text{Potential} \\ \nabla p_0 = -\rho_0 g_0\hat{r} & \text{Hydrostatic pressure}\,, \end{cases} \tag{3.13}$$

where subscript 0 denotes all fields in the initial unperturbed state. Substituting the expression for $\mathbf{T}_0$ and $\mathbf{F}_0$ in the Equation of motion (3.8), we obtain:

$$\rho_0 \nabla \phi_0 + \nabla p_0 = 0 \,. \tag{3.14}$$

Let's now assume that this system is subject to a deformation. In this case, the density field, the gravitational potential and the pressure field vary as

$$\rho = \rho_0 + \rho_1 \qquad \phi = \phi_0 + \phi_1 \qquad p = p_0 + p_1 \,, \tag{3.15}$$

where we have assumed that these variations are infinitesimal, so that $\rho_1 \ll \rho_0$, $\phi_1 \ll \phi_0$ and $p_1 \ll p_0$.

To define the density perturbation ρ_1, we apply the law of mass conservation to a portion of volume of the elastic medium, indicating by $\hat{\boldsymbol{n}}$ the normal direction to the surface Σ containing the volume V:

$$\int_V \rho dV = \int_V \rho_0 dV - \int_\Sigma \rho_0 \boldsymbol{u} \cdot \hat{\boldsymbol{n}} d\Sigma \tag{3.16}$$

and by applying the divergence theorem on the integral over Σ, we can derive an expression for ρ_1:

$$\rho - \rho_0 \equiv \rho_1 = -\nabla \cdot (\rho_0 \boldsymbol{u}) = -\left(\rho_0 \nabla \cdot \boldsymbol{u} + u_r \partial_r \rho_0\right). \tag{3.17}$$

Hence, in the perturbed state, neglecting the higher order term $\rho_1 \nabla \phi_1$, $\boldsymbol{F}$ becomes:

$$\begin{aligned} \boldsymbol{F} = -(\rho \nabla \phi) &= -(\rho_0 + \rho_1) \nabla (\phi_0 + \phi_1) \\ &= -\rho_0 \nabla \phi_0 + (\rho_0 \nabla \cdot \boldsymbol{u} + u_r \partial_r \rho_0) g_0 \hat{\boldsymbol{r}} - \rho_0 \nabla \phi_1 \,, \end{aligned} \tag{3.18}$$

and for the stress tensor, we have:

$$\mathbf{T} = -p\mathbf{I} + \mathbf{T}^* = -(p_0 + u_r \partial_r p_0)\mathbf{I} + \mathbf{T}^* \,. \tag{3.19}$$

Putting together Eq. (3.18) and Eq. (3.19) we have:

$$\nabla \cdot \mathbf{T}^* - \nabla(\rho_0 g_0 u_r) - \rho_0 \nabla \phi_1 + (\rho_0 \nabla \cdot \boldsymbol{u} + u_r \partial_r \rho_0) g_0 \hat{\boldsymbol{r}} = 0 \,. \tag{3.20}$$

The gravitational potential variation is also a solution of Poisson's equation

$$\nabla^2\phi_1 = 4\pi G\nabla\cdot(\rho_0\boldsymbol{u})\,. \tag{3.21}$$

Together with Eq. (3.20) and (3.21), we also must account for the constitutive equation for an elastic continuum

$$\mathbf{T}^* = \lambda(\nabla\cdot\boldsymbol{u})\mathbf{I} + 2\mu\mathbf{E}\,, \tag{3.22}$$

where the infinitesimal strain tensor is:

$$\mathbf{E} = \frac{1}{2}(\big(\nabla\boldsymbol{u} + (\nabla\boldsymbol{u})^T\big)\ . \tag{3.23}$$

Assuming incompressibility, thus $\nabla\cdot\boldsymbol{u} = 0$, the previous equations become:

$$\begin{cases} \nabla\cdot\mathbf{T}^* - \nabla(\rho_0 g_0 u_r) - \rho_0\nabla\phi_1 = 0 \\ \nabla^2\phi_1 = 0 \\ \mathbf{T}^* = \Pi\mathbf{I} + 2\mu\mathbf{E} \\ \mathbf{E} = \frac{1}{2}(\nabla\boldsymbol{u} + (\nabla\boldsymbol{u})^T) \\ \nabla\cdot\boldsymbol{u} = 0 \end{cases} \tag{3.24}$$

where the product $\Pi = \lambda\nabla\cdot\boldsymbol{u}$, is assumed to have a finite limit as $\nabla\cdot\boldsymbol{u}\to 0$ and $\lambda\to\infty$ (Love, 1911). We will now consider the case of an impulsive unit load perturbation applied on the surface of the sphere in $\theta = 0$:

$$\Gamma(\theta) = \delta(\theta)\,. \tag{3.25}$$

Given the symmetry of the problem, we can assume that the displacement vector depends only upon co-latitude, *i.e.* $\boldsymbol{u} = \boldsymbol{u}(r,\theta)$. In this way, the number of unknowns reduces from four to three: the two components of the displacement u_r and u_θ, and the perturbation of the gravitational potential ϕ_1. It is also convenient to seek for solutions that can be expressed in terms of Legendre polynomials. In this way, it will be possible

to transform the set of partial differential equations (3.24) into a system of ordinary differential equations Farrell (1972). Therefore we write

$$\begin{aligned} \boldsymbol{u}(r,\theta) &= \sum_{n=0}^{\infty} \left[U_n(r) P_n(\cos\theta)\hat{\boldsymbol{r}} + V_n \partial_\theta P_n(\cos\theta)\hat{\boldsymbol{\theta}} \right] \\ \phi_1(r,\theta) &= \sum_{n=0}^{\infty} \phi_n(r) P_n(\cos\theta)\,, \end{aligned} \tag{3.26}$$

and, by doing so, the unknowns become the functions $U_n(r)$, $V_n(r)$ and $\phi_n(r)$. Substituting Eqs. (3.26) into the system (3.24), after cumbersome calculations that I skip for the sake of simplicity (for a comprehensive treatise, the reader is referred to James (1991); Martens (2016)), one obtains a system of linear differential equations of the form

$$\frac{d}{dr}\boldsymbol{y}_n(r) = \mathbf{A}_n(r)\boldsymbol{y}_n(r)\,, \tag{3.27}$$

where the vector of the solutions $\boldsymbol{y}_n$ is defined by:

$$\boldsymbol{y}_n(r) = [U_n, V_n, T_{rrn}, T_{r\theta n}, \phi_n, Q_n] \equiv [y_1, y_2, y_3, y_4, y_5, y_6]\,, \tag{3.28}$$

and where U_n, and V_n are the radial and tangential part of the displacement field, T_{rrn} and $T_{r\theta n}$ are the horizontal and tangential stresses, ϕ_n is the perturbation of the potential and finally Q_n is an auxiliary variable, defined as

$$Q_n = -\frac{d\phi_n}{dr} - \frac{(n+1)}{r}\phi_n + 4\pi G\rho_0 U_n\,, \tag{3.29}$$

introduced to simplify the application of the boundary conditions (Sabadini et al., 2016). The matrix $\boldsymbol{A}_n(r)$ reads:

$$\boldsymbol{A}_n(r) = \begin{pmatrix} -\frac{2}{r} & \frac{L}{r} & 0 & 0 & 0 & 0 \\ -\frac{1}{r} & \frac{1}{r} & 0 & \frac{1}{\tilde{\mu}} & 0 & 0 \\ \frac{4}{r}\left(\frac{3\mu}{r} - \rho_0 g_0\right) & -\frac{L}{r}\left(\frac{6\mu}{r} - \rho_0 g_0\right) & 0 & \frac{L}{r} & -\frac{\rho_0(n+1)}{r} & \rho_0 \\ -\frac{1}{r}\left(\frac{6\mu}{r} - \rho_0 g_0\right) & -\frac{2}{r^2}(1-2L)\mu & -\frac{1}{r} & -\frac{3}{r} & \frac{\rho_0}{r} & 0 \\ -4\pi G\rho_0 & 0 & 0 & 0 & -\frac{(n+1)}{r} & 1 \\ -\frac{4\pi G\rho_0(n+1)}{r} & \frac{4\pi G\rho_0 L}{r} & 0 & 0 & 0 & \frac{(n-1)}{r} \end{pmatrix}, \tag{3.30}$$

where $L \equiv n(n+1)$. Before I delve into the final part of the calculation of LNs, I present in the following sub-section the boundary conditions (BCs) for case of a impulsive δ-like surface load, and those for the tidal loading.

Boundary conditions for the mass load

The surface load expression of an impulsive unit load, expanded in series of Legendre polynomials, can be written as:

$$\Gamma(\theta) = \sum_{n=0}^{\infty} \frac{2n+1}{4\pi a^2} \tag{3.31}$$

To solve the system (3.24) it is necessary to fix BCs respectively on the vertical and horizontal components of the stress field, and on the gravitational potential:

- On the surface, the vertical traction must compensate the load $\Gamma(\theta)$ defined in (3.31) and thus we have

$$T_{rrn} = -\frac{2n+1}{4\pi a^2} g_0 \,. \tag{3.32}$$

- The horizontal traction must become null on the surface: $T_{r\theta n} = 0$ in $r = a$.

- Through the application of the Gauss' law for the gravity field, one finds that the gravitational potential must satisfy

$$\frac{d\phi_n^{ext}}{dr} - \frac{d\phi_n^{int}}{dr} = 4\pi G \left(\rho_0 U_n + \frac{2n+1}{4\pi a^2} \right) , \tag{3.33}$$

  being the terms $\frac{2n+1}{4\pi a^2}$ and $\rho_0 U_n$ the contributions of the δ-like load mass and the induced mass redistribution within the Earth. Assuming the continuity of the gravitational potential $\phi_n^{ext} = \phi_n^{int}$, a possible solution for ϕ_n could be, taking also into account that it must satisfy the Laplace equation outside the planet

$$\phi_n = c_n \left(\frac{a}{r} \right)^{n+1} , \tag{3.34}$$

with c_n being an arbitrary constant. Thus, since

$$\frac{d\phi_n}{dr} = -\frac{n+1}{r}\phi_n\,, \tag{3.35}$$

Eq. (3.33) becomes:

$$\frac{d\phi_n}{dr} - \frac{n+1}{r}\phi + 4\pi G\rho_0 U_n = 4\pi G\left(\frac{2n+1}{4\pi a^2}\right)\,, \tag{3.36}$$

implying that, the definition of Q_n (Eq. 3.29) is, in $r = a$

$$Q_n = -4\pi G\left(\frac{2n+1}{4\pi a^2}\right) = -\frac{(2n+1)G}{a^2}\,. \tag{3.37}$$

In conclusion, the BCs for the unit δ-like load reads:

$$\begin{cases} T_{rrn} = y_3(a) = -\frac{2n+1}{4\pi a^2} g_0 \\ T_{r\theta n} = y_4(a) = 0 \\ Q_n = y_6(a) = -\frac{(2n+1)G}{a^2}\,. \end{cases} \tag{3.38}$$

Boundary conditions for the tidal load

The first aim of this thesis is the study of the Earth's response to surface unloading; however, for the sake of completeness and also to ease the discussion on fluid layered planets, I shall report here also the BCs for tidal loading. Once again, for a complete description of the calculation procedure, the reader is referred to the book of Sabadini et al. (2016). Thus, for the case of an impulsive tidal perturbation exerted by a point mass located along the z-axis, the BCs read:

$$\begin{cases} T^{Tidal}_{rrn} = y_3(a) = 0 \\ T^{Tidal}_{r\theta n} = y_4(a) = 0 \\ Q^{Tidal}_{n} = y_6(a) = -\frac{(2n+1)G}{a^2}\,, \end{cases} \tag{3.39}$$

which, with the exception of $y_3(a)$, are identical to those of the impulsive δ-like load: as a matter of fact, in tidal phenomena the disturbing mass is not in contact with the planet, and so the vertical (and the tangential) stresses at the surface must vanish.

Solution for the Homogeneous Elastic Planet

The general solution of the system (3.24) can be written in the following compact matrix form:

$$\boldsymbol{y}(r) = \boldsymbol{Y}(r)\boldsymbol{c}\,, \tag{3.40}$$

where $\boldsymbol{c}$ is a vector of arbitrary constants to be set through BCs and $Y(r)$ is the *fundamental matrix*

$$\boldsymbol{Y}(r) = \begin{pmatrix}
\frac{n}{2(2n+3)}r^{n+1} & r^{n-1} & 0 & \frac{n+1}{2(2n-1)}r^{-n} & r^{-(n+2)} & 0 \\
\frac{n+3}{2(n+1)(2n+3)}r^{n+1} & \frac{1}{n}r^{n-1} & 0 & \frac{2-n}{2n(2n-1)}r^{-n} & -\frac{1}{n+1}r^{-(n+2)} & 0 \\
\frac{n\rho_0 g_0 r+2\left(n^2-n-3\right)\mu}{2(2n+3)}r^n & \frac{(\rho_0 g_0 r+2(n-1)\mu)}{r^{2-n}} & \rho_0 r^n & \frac{(n+1)\rho_0 g_0 r-2\left(n^2+3n-1\right)\mu}{2(2n-1)r^{(n+1)}} & \frac{(\rho_0 g_0 r+2(n+1)\mu)}{r^{(n+3)}} & \rho_0 r^{-(n+1)} \\
\frac{n(n+2)}{(2n+1)(2n+3)}\mu r^n & \frac{2(n-1)}{n}\mu r^{n-2} & 0 & \frac{n^2-1}{n(2n-1)}\mu r^{-(n+1)} & \frac{2(n+2)}{n+1}\mu r^{-(n+3)} & 0 \\
0 & 0 & r^n & 0 & 0 & r^{-(n+1)} \\
2\pi G\rho_0\frac{n}{2n+3}r^{n+1} & 4\pi G\rho_0 r^{n-1} & (2n+1)r^{n-1} & 2\pi G\rho_0\frac{n+1}{2n-1}r^{-n} & 4\pi G\rho_0 r^{-(n+2)} & 0
\end{pmatrix}, \tag{3.41}$$

whose columns are six linearly independent solutions of (3.24).

For the specific case of an homogeneous elastic sphere (*i.e.,* the "Kelvin sphere") we need solutions that are regular at the centre of the planet. Thus, we must consider only the first three columns of the matrix $\boldsymbol{Y}(r)$: the other columns contain indeed singular terms in r, that would diverge for $r \to 0$. Denoting it by $\boldsymbol{Y}_R$, the solution we seek has the following form:

$$\boldsymbol{y}(r) = \boldsymbol{Y}_R(r)\boldsymbol{c} \tag{3.42}$$

To determine $\boldsymbol{c}$, we first notice that the BCs (3.38) and (3.39) can be written in matrix form as

$$\boldsymbol{P}_2\boldsymbol{y}(a) = \boldsymbol{b}\,, \qquad \boldsymbol{P}_2 = \begin{pmatrix} 0 & 0 & 1 & 0 & 0 & 0 \\ 0 & 0 & 0 & 1 & 0 & 0 \\ 0 & 0 & 0 & 0 & 0 & 1 \end{pmatrix}\,, \tag{3.43}$$

where $\boldsymbol{P}_2$ is the so-called "projector operator" (Spada, 1992), whose purpose is selecting the components of $\boldsymbol{y}$ on which we prescribe the boundary conditions (namely the third, the fourth and the sixth, as it is clear from its definition in Eq. (3.28)), and $\boldsymbol{b}$ is the vector containing the BCs (3.38). Then, in view of Eq. (3.42) and (3.43) we obtain:

$$\boldsymbol{c} = (\boldsymbol{P}_2\boldsymbol{Y}_R(a))^{-1}\boldsymbol{b}\,. \tag{3.44}$$

Now, recalling the definitions of LNs in Eqs. (3.4, 3.5, 3.6) and considering that, for the case of an impulsive unit load, the coefficients of the direct gravitational potential are:

$$\phi_{0,n}(a) = -\frac{G}{a} = -\frac{ag_0}{m_e}\,, \tag{3.45}$$

we have:

$$\boldsymbol{z} = \begin{pmatrix} y_1(a) \\ y_2(a) \\ y_5(a) \end{pmatrix} = \frac{a}{m_e}\begin{pmatrix} h_n \\ l_n \\ -(1+k_n)g_0 \end{pmatrix}\,. \tag{3.46}$$

By recasting these definitions in a matrix formalism, we can write, considering Eq. (3.42) and (3.44)

$$\boldsymbol{z} = \boldsymbol{P}_1\boldsymbol{y}(a) = \boldsymbol{P}_1\boldsymbol{Y}_R(a)\boldsymbol{c} = \boldsymbol{P}_1\boldsymbol{Y}_R(a)(\boldsymbol{P}_2\boldsymbol{Y}_R(a))^{-1}\boldsymbol{b}\,, \tag{3.47}$$

being $\boldsymbol{P}_1$ the projection matrix

$$\boldsymbol{P}_1 = \begin{pmatrix} 1 & 0 & 0 & 0 & 0 & 0 \\ 0 & 1 & 0 & 0 & 0 & 0 \\ 0 & 0 & 0 & 0 & 1 & 0 \end{pmatrix}\,. \tag{3.48}$$

After long calculations that have been handled with the use of a symbolic manipulator, it is possible to find an analytical expression for $\boldsymbol{z}$; Finally, inverting Eq. (3.46), we obtain the definition of the loading LNs for the elastic Kelvin sphere:

$$\boldsymbol{x}_n^E = \begin{pmatrix} h_n^E \\ l_n^E \\ k_n^E \end{pmatrix} = \frac{1}{1+c} \begin{pmatrix} -\frac{2n+1}{3} \\ \frac{1}{n} \\ -1 \end{pmatrix} , \tag{3.49}$$

with

$$c = \mu' \lambda_n \,, \quad \mu' = \frac{\mu}{\rho_0 g_0 a} \quad \text{and} \quad \lambda_n = \frac{2n^2+4n+3}{n} \,. \tag{3.50}$$

It is noteworthy to remark that from the definition of the elastic loading LNs (3.49) it is possible to draw the expression for the LNs in the "fluid limit" by imposing that the rigidity $\mu \to 0$:

$$\boldsymbol{x}_n^F = \begin{pmatrix} h_n^F \\ l_n^F \\ k_n^F \end{pmatrix} = \begin{pmatrix} -\frac{2n+1}{3} \\ \frac{1}{n} \\ -1 \end{pmatrix} . \tag{3.51}$$

In case of a viscoelastic model, the value of the LNs depends on time. In this case, as we will see in the following, the fluid limit of LNs is obtained by computing their limit for $t \to \infty$.

3.3 Viscoelastic Love numbers

The elastic solution found in previous Section 3.2 can be easily extended through the *Correspondence Principle* to any other linear viscoelastic rheology (Fung, 1965). The constitutive equations of linear viscoelastic bodies describe the relation between the stresses σ and the strain ϵ, and can be expressed as:

$$\boldsymbol{P}\sigma(\boldsymbol{x}, t) = \boldsymbol{Q}\epsilon(\boldsymbol{x}, t) \,, \tag{3.52}$$

where $\boldsymbol{x}$ indicates the position and $\boldsymbol{P}$, $\boldsymbol{Q}$ are differential operators of the form $F = \sum_{j=0}^{n} f_j \frac{d^j}{dt^j}$. In the Laplace domain, one obtains:

$$P(s)\tilde{\sigma}(\boldsymbol{x}, s) = Q(s)\tilde{\epsilon}(\boldsymbol{x}, s) \tag{3.53}$$

where P and Q have become polynomials in the variable s. Then, writing

$$\tilde{\sigma}(\boldsymbol{x}, s) = \frac{Q(s)}{P(s)}\tilde{\epsilon}(\boldsymbol{x}, s) = E(s)\tilde{\epsilon}(\boldsymbol{x}, s) \tag{3.54}$$

one obtains an expression that is formally identical to the Hooke linear elastic law, $\sigma(\boldsymbol{x}, t) = E(t)\epsilon(\boldsymbol{x}, t)$. In other words, we have shown that the solution of a viscoelastic problem can be found by solving in the Laplace domain the *corresponding* elastic problem, taking care of correctly substituting the constant E with the corresponding $E(s)$.

In the specific case of LNs, from the expressions for the elastic Kelvin sphere Eq. (3.49), one can easily get the Laplace-transformed viscoelastic ones just by substituting to the elastic rigidity the suitable complex modulus $\tilde{\mu}$:

$$\tilde{\boldsymbol{x}}_n(s) = \begin{pmatrix} \tilde{h}_n(s) \\ \tilde{l}_n(s) \\ \tilde{k}_n(s) \end{pmatrix} = \frac{\boldsymbol{x}_n^F}{1 + c\frac{\tilde{\mu}(s)}{\mu}} \,. \tag{3.55}$$

For example, the Laplace domain loading LNs of a Kelvin sphere with Maxwell's rheology can be obtained by substituting in (3.55) the Maxwell complex rigidity

$$\tilde{\mu}(s) = \frac{\mu s}{s + \frac{\mu}{\eta}} \,. \tag{3.56}$$

To recover the time domain LNs, the inverse Laplace transform of Eq. (3.55) must be computed. After some efforts, the time-domain LNs for a Kelvin model with Maxwell's rheology can be written as:

$$\begin{pmatrix} h_n^M(t) \\ l_n^M(t) \\ k_n^M(t) \end{pmatrix} = \boldsymbol{x}_n^E \delta(t) + H(t)\boldsymbol{x}_n^F \left(\frac{\frac{1}{\tau_M} - \frac{1}{\tau'_M}}{1 + c} \right) e^{(-t/\tau'_M)} \,, \tag{3.57}$$

with $\tau_M = \eta/\mu$ being the Maxwell time and $\tau'_M = \tau_M(1+c)$; more details about this calculation can be found in (Consorzi, 2021). The previous equation can be recast in a more compact form as:

$$\boldsymbol{x}_n^M(t) = \boldsymbol{x}_n^E \delta(t) + H(t)\boldsymbol{x}_n^V e^{-t/\tau'_M}\,, \tag{3.58}$$

where $\boldsymbol{x}_n^M$ indicates the vector containing the LNs. More in general, this definition can be extended to any other rheological model, and it is known as "multi-exponential form" of the LNs:

$$\boldsymbol{x}_n(t) = \boldsymbol{x}_n^E \delta(t) + H(t) \sum_{k=1}^{i} \boldsymbol{x}_{n,i}^V e^{-t/\tau_{n,i}}\,. \tag{3.59}$$

The multi-exponential form of LNs is introduced in the viscoelastic normal modes (VNM) method (Peltier, 1974), and as it is clear from above, it allows to write the LNs as the sum of two components: an elastic one $\boldsymbol{x}_n^E$, that depends on the density and elastic parameters, and the viscous one $\boldsymbol{x}_n^V$, that depends also on the rheology. A more detailed discussion on VNM method will be presented in Section 4.2.

3.4 Love Numbers for layered fluid planets

Part of this work was published on Astronomy and Astrophysics by Consorzi et al. (2023).

This section is dedicated to the study of LNs of a layered fluid planet, a model often employed in planetary sciences for applications to gas giants or exoplanets. Generally, LNs for multi-layered planets are computed numerically (Padovan et al., 2018; Melini et al., 2022), but in several special circumstances, optimal simplification of the equations could lead to analytical expressions. These fortunate cases offer the possibility to further investigate the role of each model parameter in the determination of LNs. This is the case of a two-layer model of a fluid planet, whose LN k_2 in closed-form was first published by

Ragazzo (2020). In parallel, the work of Padovan et al. (2018) shows that the mean polar moment of inertia (N) and the Love number (k_2) of a planet have a similar sensitivity to the mass concentration, supporting the results of Kramm et al. (2011).

With the purpose of refining the implicit approximation of Padovan et al. (2018), namely $N \approx k_2$, we delved into the N-k_2 relationship. Our two major findings are:

- a simple power-law relation (*rule of thumb*) exists between the normalized mean polar moment of inertia and the normalized k_2, namely $\overline{N} = \overline{k}_2^{0.4}$. This result was already reported by Ragazzo (2020), following other methods.

- for multi-layered models the *rule of thumb* determines an upper limit for N for a given, hypothetically observed k_2 value. Our work demonstrate that this rule is superior to the Radau-Darwin formula (Cook, 1980).

3.4.1 The homogeneous fluid planet

In the special case of a fluid planet, k_2 only depends upon the density profile. In the next lines, we shall demonstrate this statement. In the unperturbed state, the assumption of hydrostatic equilibrium implies:

$$\nabla p_0 = -\rho_0 \nabla \phi_0 \tag{3.60}$$

with p being the hydrostatic pressure, ρ the density and ϕ the gravitational potential, always obeying Poisson's equation. In the perturbed state, the previous equation becomes

$$\nabla(p_0 + p_1) = -(\rho_0 + \rho_1)\nabla(\phi_0 + \phi_1) \tag{3.61}$$

$$= -\rho_0 \nabla \phi_0 - \rho_0 \nabla \phi_1 - \rho_1 \nabla \phi_0 - \rho_1 \nabla \phi_1 \,. \tag{3.62}$$

Discarding the second order term and considering Eq. (3.60), we obtain:

$$\nabla p_1 = -\rho_1 \nabla \phi_0 - \rho_0 \nabla \phi_1 = -\rho_1 g_0 - \rho_0 \nabla \phi_1 \tag{3.63}$$

By making explicit the gradient in the previous expression, it is possible to demonstrate that

$$p_1 = -\rho_0 \phi_1 \,. \tag{3.64}$$

From the radial component of Eq. (3.63) we have

$$\frac{\partial p_1}{\partial r} = -\rho_0 \frac{\partial \phi_1}{\partial r} - \rho_1 g_0 \,, \tag{3.65}$$

and using Eq. (3.64) we find:

$$\frac{\partial \rho_0}{\partial r} \phi_1 = \rho_1 g_0 \,. \tag{3.66}$$

In this way, the perturbed gravitational field, that must obey to Laplace equation, can be recast as:

$$\nabla^2 \phi_1 = 4\pi G \rho_1 = \frac{4\pi G}{g_0} \frac{\partial \rho_0}{\partial r} \,. \tag{3.67}$$

With an approach identical to that presented in the previous Section 3.2, we seek for a solution that can be expressed in terms of Legendre Polynomials

$$\phi_1(r, \theta) = \sum_{n=0}^{\infty} \varphi_{1,n} P_n(\cos\theta) \,, \tag{3.68}$$

where $\varphi_{1,n}(r)$ are suitable radial functions, P_n is the $n^{th}-$degree Legendre polynomial and θ is co-latitude. Finally, substituting Eq (3.68) into Poisson's equation Eq. (3.67), the latter reduces to a second order differential equation for φ_1 that reads:

$$\varphi_1{}'' + \frac{2}{r}\varphi_1{}' - \left(\frac{n(n+1)}{r^2} + \frac{4\pi G}{g_0} \rho_0' \right) \varphi_1 = 0 \,, \tag{3.69}$$

where we have dropped the n subscript of φ_1 to lighten the notation, and the prime denotes the derivative with respect to radius r (Wu and Peltier, 1982)[1]. Assuming a layered model in which, inside each layer, the density remains constant (*i.e.*, $\rho_0' = 0$), Eq. (3.69) allows for a closed-form solution in terms of powers of r.

[1]Eq. (46a) of Wu and Peltier (1982) contains a misprint and ρ_0 should be substituted by ρ_0'.

As it has been done before, it is convenient to introduce an auxiliary variable that we shall call φ_2:

$$\varphi_2(r) = \varphi_1' + \left(\frac{n+1}{r} - \frac{4\pi G\rho_0}{g_0}\right)\varphi_1\,, \tag{3.70}$$

that is equivalent to:

$$\varphi_1'(r) = \varphi_2 - \left(\frac{n+1}{r} + \frac{4\pi G\rho_0}{g_0}\right)\varphi_1\ . \tag{3.71}$$

After some algebra, it is also possible to obtain:

$$\varphi_2'(r) = \frac{8\pi G\rho_0}{g_0 r}(n-1)\varphi_1 + \left(\frac{n-1}{r} - \frac{4\pi G\rho_0}{g_0}\right)\varphi_2\,. \tag{3.72}$$

The solutions of Eqs. (3.71) and (3.72) can be found in a straightforward way:

$$\varphi_1(r) = cr^n + c^* r^{-(n+1)} \tag{3.73}$$

$$\varphi_2(r) = c\left(\frac{2n+1}{r} - \frac{4\pi G\rho_0}{g_0}\right)r^n + c^*\left(\frac{4\pi G\rho_0}{g_0}\right)r^{-(n+1)} \tag{3.74}$$

where c and c^* are constants whose values must be determined by imposing suitable BCs. Finally, by casting the equations above into a 2×2 matrix, we find the analogue of the solution matrix $Y(r)$ in Eq. (3.24) for a homogeneous fluid shell:

$$\boldsymbol{Y}^f(r) = \begin{pmatrix} r^n & r^{-(n+1)} \\ \frac{2n+1}{r} - \frac{4\pi G\rho_0}{g_0}r^n & \frac{4\pi G\rho_0}{g_0}r^{-(n+1)} \end{pmatrix} \tag{3.75}$$

As argued before, in case of a homogeneous planet we must consider only the regular part of the solution (3.75). In this case, the gravitational acceleration is simply $g_0(r) = \frac{4}{3}\pi G\rho_0 r$, and thus the solution matrix can be compacted into the following solution vector:

$$\boldsymbol{I}^f(r) = \begin{pmatrix} r^n \\ 2(n-1)r^{(n-1)} \end{pmatrix}\ . \tag{3.76}$$

3.4.2 Analytical results for a fluid two-layer planet

In this Section we will delve into the detail of the computations of the k_2 LN for a fluid two-layer inviscid planet. I will denote by r_c and ρ_c the radius of the inner layer (the "core") and its density, respectively, and by r_m and ρ_m the corresponding quantities for the outer shell (to which I will refer to as "mantle"). In this case, we must take into account the BCs both at the layers interface, and at the surface. Across the density discontinuity at radius r we impose the continuity of φ_1 and φ_2:

$$\varphi_1(r^-) = \varphi_1(r^+) \tag{3.77}$$

$$\varphi_2(r^-) = \varphi_2(r^+) \tag{3.78}$$

Since we are only interested in the tidal LN k_2, the vector $\boldsymbol{z}$ can be compacted to a scalar including only the term $\varphi_1(r)$. Having just one unknown, the following BC, obtained from calculations analogous to those that yielded to the third element of vector Eq. (3.39), is sufficient for our purpose:

$$b = \varphi_2(r_m) = -\frac{(2n+1)G}{r_m^2}\,. \tag{3.79}$$

At this point, the procedure to compute the tidal LN k_2 is similar to that followed in the Section 3.2: the only difference is the presence of a density discontinuity, the "Core-Mantle Boundary" (CMB).

To find the solution for the k_2 LN, we start by noticing that the solution vector $\boldsymbol{y}(r) = (\varphi_1(r), \varphi_2(r))$ at $r = r_c$ must be:

$$\boldsymbol{y}(r) = \boldsymbol{I}^f(r)c_c \quad \text{with} \quad 0 < r \leq r_c\,, \tag{3.80}$$

where c_c is an unknown constant and we have used $\boldsymbol{I}^f$ since it is the regular part of the solution matrix, and we need the solution to be non-singular at the center of the planet. At the same time, inside the mantle we have:

$$\boldsymbol{y}(r) = \boldsymbol{Y}^f(r)\boldsymbol{c}_m \quad \text{with} \quad r_c < r \leq r_m \tag{3.81}$$

where $\boldsymbol{c}_m$ is a (two component) vector of unknown constants. The continuity at the CMB implies:

$$\boldsymbol{Y}^f(r_c)\boldsymbol{c}_m = \boldsymbol{I}^f(r_c)c_c\,, \tag{3.82}$$

from which we can express $\boldsymbol{c}_m$ as:

$$\boldsymbol{c}_m = \boldsymbol{Y}^f(r_c)^{-1}\boldsymbol{I}^f(r_c)c_c\,. \tag{3.83}$$

In this way, the solution vector at the surface becomes:

$$\boldsymbol{y}(r_m) = \boldsymbol{Y}^f(r_m)\boldsymbol{c}_m = \boldsymbol{Y}^f(r_m)\boldsymbol{Y}^f(r_c)^{-1}\boldsymbol{I}^f(r_c)c_c\,. \tag{3.84}$$

Now, applying the BC for φ_2:

$$\boldsymbol{P}_2\boldsymbol{y}(r_m) = b\,, \quad \text{with} \quad \boldsymbol{P}_2 = \begin{pmatrix} 0 & 1 \end{pmatrix}\,, \tag{3.85}$$

it follows that

$$b = \boldsymbol{P}_2\boldsymbol{Y}^f(r_m)\boldsymbol{Y}^f(r_c)^{-1}\boldsymbol{I}^f(r_c)c_c\,, \tag{3.86}$$

from which we obtain

$$c_c = \boldsymbol{R}^{-1}b\,, \quad \text{with} \quad \boldsymbol{R} = \boldsymbol{P}_2\boldsymbol{Y}^f(r_m)\boldsymbol{Y}^f(r_c)^{-1}\boldsymbol{I}^f(r_c)\,. \tag{3.87}$$

Finally, as we did in Eq. (3.47),

$$\begin{aligned} z \equiv \varphi_1(r_m) &= \boldsymbol{P}_1\boldsymbol{y}(r_m) \\ &= \boldsymbol{P}_1\boldsymbol{Y}^f(r_m)\boldsymbol{Y}^f(r_c)^{-1}\boldsymbol{I}^f(r_c)c_c \\ &= \boldsymbol{P}_1\boldsymbol{Y}^f(r_m)\boldsymbol{Y}^f(r_c)^{-1}\boldsymbol{I}^f(r_c)\boldsymbol{R}^{-1}b \\ &= \boldsymbol{Q}\boldsymbol{R}^{-1}b, \end{aligned} \tag{3.88}$$

where

$$\boldsymbol{Q} = \boldsymbol{P}_1\boldsymbol{Y}^f(r_m)\boldsymbol{Y}^f(r_c)^{-1}\boldsymbol{I}^f(r_c)\,, \quad \text{and} \quad \boldsymbol{P}_1 = \begin{pmatrix} 1 & 0 \end{pmatrix}\,. \tag{3.89}$$

To find the LN k_2, it is then sufficient set $n = 2$ in the computations and, at the end, recalling the third term of Eq. (3.46), we obtain:

$$k_2 = -1 - \left(\frac{m}{g r_m}\right) \varphi_1(r_m)\,. \tag{3.90}$$

With the aid of the *Mathematica©* symbolic manipulator (Wolfram Research, 2010), we find

$$\overline{k}_2 = 2\frac{5 + \alpha\left(5\alpha\beta^8 + 8\,(1-\alpha)\,\beta^5 + 3\alpha - 8\right)}{10 + \alpha\left(9\beta^5\,(\alpha-1) + 5\beta^3\,(5-3\alpha) + 6\alpha - 16\right)}\,, \tag{3.91}$$

where $\overline{k}_2$ is the normalized LN

$$\overline{k}_2 = \frac{k_2}{k_{2h}} \tag{3.92}$$

and

$$k_{2h} = \frac{3}{2} \tag{3.93}$$

is the LN for a homogeneous planet (Munk and MacDonald, 1975). In (3.91) we have introduced the non-dimensional core radius

$$\beta = \frac{r_c}{r_m}\,, \tag{3.94}$$

with $0 \leq \beta \leq 1$, and the ratio

$$\alpha = \frac{\rho_c - \rho_m}{\rho_c}\,. \tag{3.95}$$

Notice that the parameter α should not be confused here with Andrade's parameter. In case of a gravitationally stable planet ($\rho_c \geq \rho_m$) we have $0 \leq \alpha \leq 1$. The value $\alpha = 1$ corresponds to the limit case of a mass-less mantle ($\rho_m = 0$), whereas for a homogeneous planet ($\rho_m = \rho_c$), one has $\alpha = 0$.

Since the planet is fluid and inviscid, vertical displacement is interpreted as the displacement of equi-potential surfaces so that the vertical LN is $h_2 = 1 + k_2$. As the

tangential displacement is undetermined within a perfect fluid, the l_2 LN is undefined. Further, $k_2' = k_2 - h_2$, where k_2' is the loading LN for gravitational potential (Molodensky, 1977). Hence $k_2' + 1 = 0$, which manifests a condition of perfect isostatic equilibrium (Munk and MacDonald, 1975). It is worth to remark that, although in Eq. (3.91) $\overline{k}_2$ is written in terms of α and β, it depends implicitly upon the four parameters defining the model (namely, r_c, r_m, ρ_c and ρ_m). Thus, even assuming that the size of a hypothetical extra-solar planet is known and that we dispose of an observed value of $\overline{k}_2$, it is impossible to determine the remaining three quantities unambiguously.

As expected, the well-known result $\overline{k}_2 = 1$ valid for the Kelvin sphere (Thomson, 1863), is retrieved from Eq. (3.91) whenever one of the three limits $\alpha \mapsto 0$, $\beta \mapsto 0$ and $\beta \mapsto 1$ are taken. The smallest possible value of k_2 is met in the extreme condition of a point-like mass concentration at the planet centre (Roche model, see Roche, 1873). Indeed, with $\rho_m \ll \rho_c$ (hence $\alpha \mapsto 1$) and $\beta \mapsto 0$, Eq. (3.91) gives $k_2 \mapsto 0$, in agreement with Padovan et al. (2018). In Figure 3.1a, the normalized LN $\overline{k}_2$ is shown as a function of α and β for the two-layer model, according to Eq. (3.91). It is apparent that, for a given α value, the same value of $\overline{k}_2$ may be obtained for two distinct values of β. On the contrary, for a given β, knowledge of $\overline{k}_2$ would determine α unequivocally. However, due to the definition of this parameter (Eq. 3.95), knowledge of α would not suffice to determine the layers densities.

3.4.3 Moment of inertia and the k_2 fluid Love number

Two-layer models

The normalized polar moment of inertia of a spherical planet is defined as:

$$N = \frac{C}{MR^2}\,, \tag{3.96}$$

where C is the polar moment of inertia, M is the mass of the body, and R is the mean radius (see, *e.g.*, Hubbard, 1984). In case of a homogeneous body, N assumes the well-

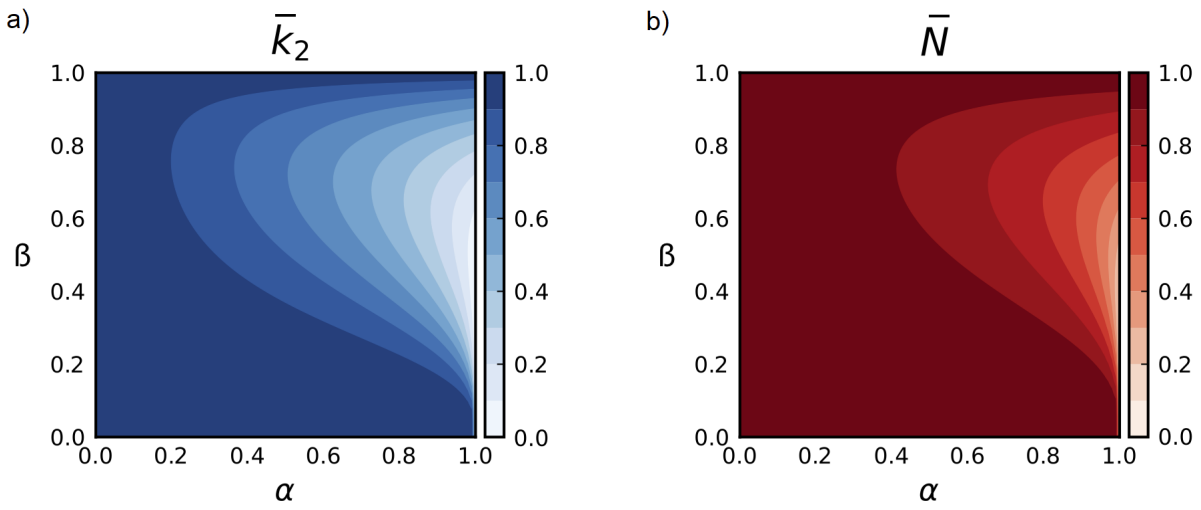

Figure 3.1: Contour plots showing $\overline{k}_2$ (a) and $\overline{N}$ (b) as a function of parameters α and β for a two-layer fluid planet, according to Eqs. (3.91) and (3.97), respectively. Since these variables are normalized to the values attained in the case of a homogeneous planet, they both range in the interval $(0, 1)$.

known value $N_h = 2/5$.

Now, defining $\overline{N} = N/N_h$, through elementary algebra it is possible to express the normalized moment of inertia $\overline{N}$ of a two-layer planet as:

$$\overline{N} = \frac{1 + \alpha\,(\beta^5 - 1)}{1 + \alpha\,(\beta^3 - 1)}\,. \tag{3.97}$$

Both $\overline{k}_2$ and $\overline{N}$ depend on the density profile of the planet, and comparing their definitions (3.97) and (3.91), one can see immediately that they depend on the same parameters α and β. In this context, following the work of Kramm et al. (2011), Padovan et al. (2018) have shown that for a planet with two constant density fluid layers, $\overline{N}$ and $\overline{k}_2$ are directly correlated, both decreasing with increasing mass concentration at depth. However, Padovan et al. did not propose explicitly a general relationship between these two quantities.

It has been long known that an approximate relationship between $\overline{N}$ and $\overline{k}_2$ is expressed by the Radau-Darwin (RD) formula, which is exact for a homogeneous body

but it only constitutes an approximation for layered planetary models (Kramm et al., 2011; Padovan et al., 2018). This motivates the search for alternatives. On one hand, by comparing Figure 3.1a with 3.1b it is apparent that, for our two-layer model, functions $\overline{k}_2$ and $\overline{N}$ have broadly similar shapes in the (α, β) plane, immediately suggesting a straightforward linear relationship $\overline{N} \simeq \overline{k}_2$. Such relation has been implicitly proposed by Padovan et al. (2018) and would be exact for a uniform sphere. On the other hand, if we limit ourselves to an inspection of the analytical expressions (3.91) and (3.97), it is not easy to guess whether an exact $\overline{N}$-$\overline{k}_2$ relation may exist in analytical form. *A priori*, for a non-homogeneous planet such relation might be non-univalent, with more $\overline{N}$ values corresponding to a given $\overline{k}_2$ and *viceversa*.

After some symbolic manipulations, we have verified that solving Eq. (3.97) for α and substituting into (3.91) would not provide insightful results. This suggests that an exact relationship $\overline{N} = \overline{N}(\overline{k}_2)$ not involving α and z explicitly and valid for all values of these parameters can be almost certainly ruled out. Nevertheless, simple relationships of partial validity could exist in some limiting cases where α or z take special values. For example, it is easy to show that for small core bodies ($\beta \mapsto 0$), $\overline{N} \simeq 1 + (2/5)(\overline{k}_2 - 1)$, which holds for all values of α and still implies that mass concentration at depth increases for decreasing $\overline{k}_2$. Along the same lines, for $\alpha \mapsto 1$, corresponding to case of a dense "core" surrounded by a "light mantle", Eq. (3.97) gives $\overline{N} \simeq \beta^2$ and since from Eq. (3.91) $\overline{k}_2 \simeq \beta^5$, by eliminating β we obtain an appealingly simple approximate power-law relationship $\overline{N} \simeq \overline{k}_2{}^{0.4}$. We notice that this last relationship is actually an exact result for a homogeneous sphere surrounded by an hypothetical zero-density mantle, and can be obtained analytically by rescaling the results for a Maclaurin spheroid (Hubbard, 2013) of radius a to the outer radius $r > a$ of the mass-less envelope (Hubbard, 2023, personal communication).

The approximate $\overline{N}$-$\overline{k}_2$ relationships discussed above are only valid for specific ranges of α and z. Certainly, a straightforward linear relationship captures the broad similitude

of the diagrams in Figures 3.1a and 3.1b, but it may represent a too simplistic solution. Here, we seek a more general *rule of thumb* (or ROT) providing, within a certain level of approximation, a relationship between $\overline{N}$ and $\overline{k}_2$ over all the points of the (α, β) plane. To quantify the error associated to a given ROT (say, $\overline{N}_{ROT}(\overline{k}_2)$), we introduce the non-dimensional root mean square

$$\mathrm{RMS} = \sqrt{\int_0^1 \int_0^1 \left[\overline{N} - \overline{N}_{ROT}(\overline{k}_2)\right]^2 d\alpha \, dz} \,, \tag{3.98}$$

where the double integral is evaluated numerically by standard methods.

First, we assume a direct proportionality

$$\overline{N} = c\,\overline{k}_2 \,, \tag{3.99}$$

where $c > 0$ is a constant. Figure 3.2a shows, as a function of c, the RMS obtained with $\overline{N}_{ROT} = c\,\overline{k}_2$. The minimum RMS (close to 0.1168) is obtained for $c \approx 1.08$, suggesting that the approximation $\overline{N} \simeq \overline{k}_2$ proposed by Padovan et al. (2018) and corresponding to $c = 1$, is indeed close to the best possible linear ROT.

Next, we consider a power-law relationship

$$\overline{N} = {\overline{k}_2}^{E} \,, \tag{3.100}$$

where $E > 0$ is an adjustable exponent. In Figure 3.2b we show, as a function of E, the RMS corresponding to $\overline{N}_{ROT} = \overline{k}_2^E$. It is apparent that the RMS is minimized for an exponent $E \approx 0.42$, close to the value of 0.4 found analytically for a zero-density mantle. The corresponding minimum RMS value is ≈ 0.0082. These findings suggest that the relationship

$$\overline{N} \approx {\overline{k}_2}^{0.4} \tag{3.101}$$

represents a simple and valid ROT expressing the link between $\overline{N}$ and $\overline{k}_2$ for a two-layer, fluid, stably layered planet characterized by arbitrary parameters α and z.

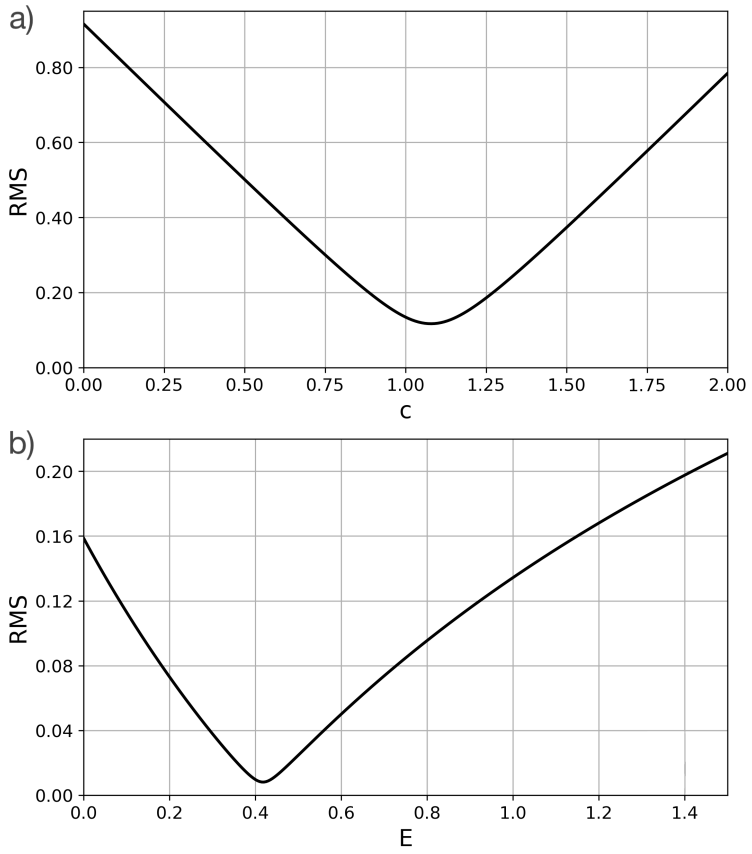

Figure 3.2: Non-dimensional RMS, evaluated according to Eq. (3.98), for a linear ROT $\overline{N} \approx c\overline{k}_2$ (frame a) and for a power law ROT $\overline{N} \approx \overline{k}_2^E$ (b), as a function of the parameters c and E, respectively. Integrals in Eq. (3.98) have been evaluated numerically by the `dblquad` function included in the SciPy library (Virtanen et al., 2020).

Arbitrarily layered models

Up to now, we have limited our attention to four-parameters models composed by two distinct fluid layers. To fully assess the validity of the ROT (3.101), it is important to consider the case of a planetary structure consisting of an arbitrary number L of homogeneous layers.

Due to the model complexity, in this general case an analytical expressions for $\overline{k}_2$ is not available; however, it is possible to evaluate $\overline{k}_2$ numerically, for instance following the propagator method outlined by Padovan et al. (2018) or employing numerical LNs calculators like `ALMA` (Melini et al., 2022). Conversely, an analytical expression for the normalized moment of inertia $\overline{N}$ is easily obtained also in the general case of an L-layer planet, and it reads

$$\overline{N} = \frac{\displaystyle\sum_{i=1}^{L}(1-\alpha_i)\left(\beta_i^5 - \beta_{i-1}^5\right)}{\displaystyle\sum_{i=1}^{L}(1-\alpha_i)\left(\beta_i^3 - \beta_{i-1}^3\right)}\,, \tag{3.102}$$

where $\beta_i = r_i/r_m$ is the normalized radius of the outer boundary of the i-th layer ($\beta_0 \equiv 0$) and

$$\alpha_i = \frac{\rho_1 - \rho_i}{\rho_1}\,, \tag{3.103}$$

where ρ_i is the density of the i-th layer. By definition, $\beta_1 \leq \ldots \leq \beta_L = 1$, while gravitational stability imposes $\rho_1 \leq \ldots \leq \rho_L$ so that $1 \geq \alpha_L \geq \ldots \geq \alpha_1 = 0$. It is easily shown that, for $L = 2$, Eq. (3.102) reduces to (3.97) with $\alpha \equiv \alpha_2$ and $\beta \equiv \beta_1$.

To test whether the ROT (3.101) can be of practical use also for general planetary structures, we have generated an ensemble of 5×10^5 models with a number of layers variable between $L = 2$ and $L = 10$, all characterized by a gravitationally stable density profile. For each of the planetary structures so obtained, we have computed $\overline{N}$ according to Eq. (3.102) and $\overline{k}_2$ with the numerical codes made available by Padovan et al. (2018). The corresponding values of $\overline{N}$ and $\overline{k}_2$ are shown in Figure 3.3 as gray dots. F3.3

For a given, hypothetically observed $\overline{k}_2$ value, the corresponding value of $\overline{N}$ is clearly not unique. Rather, $\overline{N}$ ranges within an interval, defined by the cloud of points, whose width represents the uncertainty associated to the degree of mass concentration at depth. It is apparent that the maximum relative uncertainty on $\overline{N}$ (up to $\sim 50\%$) occurs for $\overline{k}_2$ values $\lesssim 0.2$ and that, for $\overline{k}_2$ exceeding ≈ 0.5, the $\overline{N}$ value is rather well constrained (to within $\approx 10\%$). Of course, this does not imply that the density profile of the planet is actually constrained, since Eq. (3.102) cannot be inverted for α_i and β_i unequivocally without introducing further assumptions. The solid red line in Figure 3.3 represents the ROT (3.101), obtained in the context of the two-layer model in the previous paragraph. It is apparent that the ROT remains valid also in the general case of a L-layer planetary model and, for $\overline{k}_2 \gtrsim 0.5$, it provides a good estimate of $\overline{N}$ once $\overline{k}_2$ is known. For smaller values of $\overline{k}_2$, the ROT represents an upper bound to the normalized moment of inertia:

$$\overline{N} \lesssim \overline{k}_2^{0.4} \,. \tag{3.104}$$

In the context of planetary structure modeling, the polytrope of unit index (Chandrasekhar and Milne, 1933) has a particular relevance. This simplified model resembles the interior barotrope of a hydrogen-rich planet in the jovian mass range and, by virtue of the linear relation between mass density and gravitational potential, it allows for the derivation of exact results useful for calibrating numerical solutions. Hubbard (1975) obtained analytical expressions of the moment of inertia and of the k_2 fluid LN for a polytrope of index one, which are marked by a blue dot in Figure 3.3. More recently, Wahl et al. (2020) modeled the equilibrium tidal response of Jupiter through the concentric Maclaurin spheroid method; their results in the non-rotating limit are marked by a green triangle in Figure 3.3. It is evident that the ROT turns out to be in excellent agreement with these two particular cases. However, we remark that for a quantitative application of our results to real exoplanets, rotational effects and nonlinear responses to rotational and tidal terms should be also considered (see, *e.g.* Wahl et al., 2017, 2020).

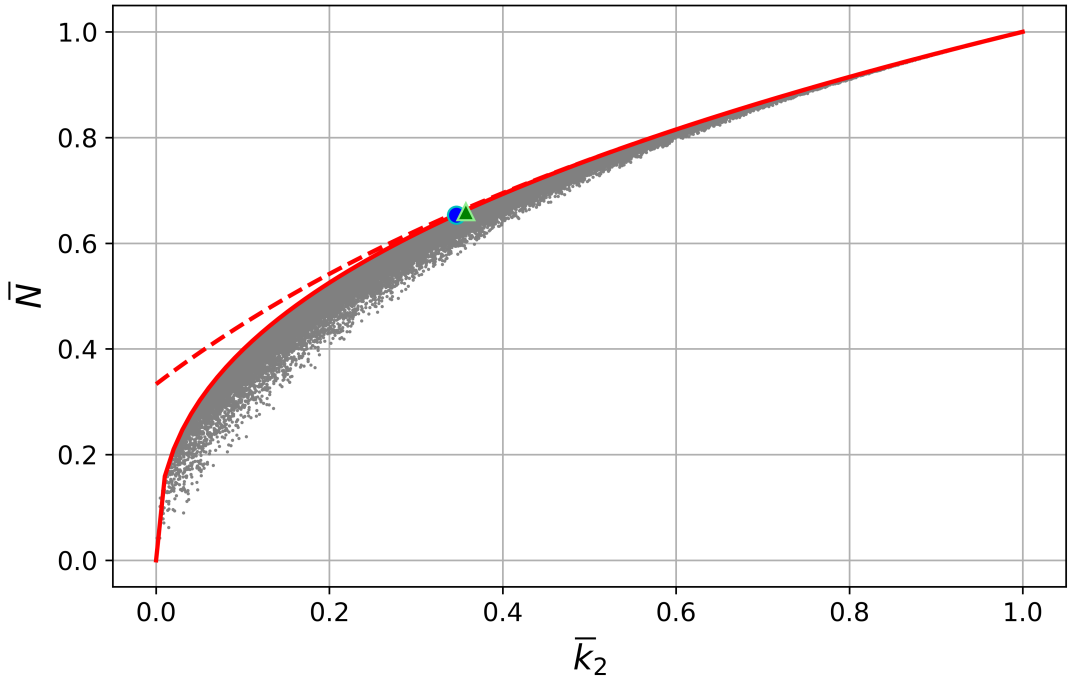

Figure 3.3: Fluid LN $\overline{k}_2$ and normalized moment of inertia $\overline{N}$ for a random ensemble of 5×10^5 models with a number of layers $2 \leq L \leq 10$. The solid line shows the ROT $\overline{N} = \overline{k}_2^{0.4}$. The dashed one represents the Radau-Darwin (RD) formula (*e.g.,* Cook, 1980; Padovan et al., 2018; Ragazzo, 2020). The RD formula is exact for a homogeneous body but it constitutes an approximation for layered planets (Kramm et al., 2011; Padovan et al., 2018). The ROT and the RD formula match for $\overline{k}_2 \gtrsim 0.3$; for smaller values, our ROT represents a more rigorous upper limit to $\overline{N}$. The blue dot corresponds to values of $\overline{k}_2$ and $\overline{N}$ for a polytrope of index one, while the green triangle corresponds to results by Wahl et al. (2020) for the equilibrium tidal response of Jupiter.

LN	x^F tidal forcing	x^F surface loading
Potential, k_n	$\frac{3}{2(n-1)}$	-1
Vertical, h_n	$1+\frac{3}{2(n-1)}$	$-\frac{2n+1}{3}$
Horizontal, l_n	$\frac{3}{2n(n-1)}$	$-\frac{1}{n}$

Table 3.1: Expressions of the fluid limits $x^F{=}x^F(n)$ in Eq. (3.105) for the LNs h_n, k_n and l_n, corresponding to tidal and surface loading boundary conditions, as a function of the harmonic degree n. These expressions are based upon Wu and Peltier (1982).

3.5 Love numbers of an Andrade planet

In this section, we discuss two different forms of the LNs for a uniform planet with Andrade rheology, namely the Laplace domain (subsection 3.5.1) and the time domain LNs (3.5.2), respectively. Here I remark that the result presented here, the analytical expression for the LNs of a Kelvin sphere in the time domain, was unpublished before Consorzi et al. (2023). This expression derives from the general form of the relaxation modulus $G_a(t)$ obtained in Section 2.2, which was previously unknown as well.

3.5.1 Andrade's Love numbers in the Laplace domain

We report here the general form of the Laplace transformed LNs for a homogeneous, incompressible, viscoelastic planet subject to an impulsive load (see Eq. 3.55):

$$\frac{\tilde{x}(s)}{x^F} = \frac{1}{1+c\left(\dfrac{\tilde{\mu}(s)}{\mu}\right)}\,, \tag{3.105}$$

where the values of x^F for both the tidal and loading LNs are summarized in Table 3.1. Similarly, to have an idea of the magnitude of the parameters, Table 3.2 lists numerical values for the bulk properties of some terrestrial bodies, along with the corresponding

Planet	a	ρ	μ	μ'	c
	km	kg/m^3	10^{11} Pa	–	$n=2$
Mercury	2439.7	5427	0.75	1.53	14.55
Venus	6051.8	5243	1.45	0.52	4.90
Earth	6370.9	5514	1.46	0.42	4.02
Moon	1737.1	3348	0.67	7.09	67.35
Mars	3389.5	3918	1.05	2.13	20.24

Table 3.2: Numerical values of the μ' and c constants (at degree n=2) for some terrestrial bodies in the Solar System. Average radii (a), densities (ρ) and elastic shear moduli (μ) are from Table 1 of Zhang (1992).

$\mu' = \mu/(\rho g a)$ and c values obtained at degree $n = 2$. For the Earth, $\mu' \approx 0.4$, about twice the value $\mu' \approx \frac{1}{5}$ estimated by Love (1911) in his seminal work.

According to (3.105), in order to evaluate the LNs explicitly, the expression for the Andrade complex shear modulus $\tilde{\mu}_a(s)$ is necessary. The modulus is related to the transformed creep compliance and relaxation modulus by $\tilde{\mu}_a(s) = 1/s\tilde{J}_a(s) = s\,\tilde{G}_a(s)$ (*e.g.,* Mainardi, 2022). Using, in particular, the second of these identities and recalling Eq. (2.14), the expression of the complex shear modulus for the Andrade rheology turns out to be

$$\frac{\tilde{\mu}_a(s)}{\mu} = \frac{(s\tau_M)^\alpha}{(s\tau_M)^\alpha + \zeta^{-\alpha}\Gamma(1+\alpha) + (s\tau_M)^{\alpha-1}}\,, \tag{3.106}$$

and is easily verified that, as expected, in the limit $\zeta \to \infty$ the complex shear modulus (3.106) reduces to that of a 1-D Maxwell body, *i.e.*

$$\lim_{\zeta\to\infty} \tilde{\mu}_a(s) = \frac{\mu\, s}{s + 1/\tau_M} \equiv \tilde{\mu}_m(s)\,. \tag{3.107}$$

Substitution of (3.106) into (3.105) yields, after some algebra,

$$\frac{\tilde{x}(s)}{x^F} = 1 - \frac{c(s\tau_M)^\alpha}{(1+c)(s\tau_M)^\alpha + \zeta^{-\alpha}\Gamma(1+\alpha) + (s\tau_M)^{\alpha-1}}\,, \tag{3.108}$$

which represents the Laplace transformed LN for a uniform Andrade planet subject to an impulsive forcing.

In Figure 3.4, we show the landscape of the complex-valued function $F(z) = \tilde{L}(z)/x^F$ in the Argand-Gauss plane, where variable z is defined as $z \equiv s\tau_M = x + iy$, with $i = \sqrt{-1}$. Here we have assumed the traditional Andrade power law with exponent $\alpha = 1/3$ and $\zeta = 1$, and we have set $c = 4$, a value representative of the Earth. Function $\mathrm{Re}(F(z))$, shown in Figure 3.4a, is continuous in the whole z plane and symmetric with respect to the x axis, where the extrema are attained for $x < 0$ (3.4c, solid line). Function $\mathrm{Im}(F(z))$ is anti-symmetric with respect to the x-axis and vanishes for $x \geq 0$ (see 3.4b); furthermore, it shows a jump discontinuity along the real negative axis (3.4d, solid lines). In Figures 3.4c-d, dashed lines show numerical results for the ratio between the h_2 tidal LN and its fluid limit for a compressible sphere, obtained by substituting the complex shear modulus (3.106) in the analytical expressions published by Love (1911) and assuming a Lamé first parameter $\lambda = \mu$, which corresponds to a Poisson ratio $\nu = \frac{1}{4}$. It is readily seen that, on the real negative axis, the differences between the LNs spectra in the compressible and incompressible cases are very small, of the order of a few percent. Conversely, on the real positive axis the compressible spectrum shows singularities related to the Rayleigh-Taylor instabilities, which for a layered Earth have been discussed by Hanyk et al. (1999) and Vermeersen and Mitrovica (2000) in the framework of the viscoelastic normal modes theory of Peltier (1974).

3.5.2 Andrade's Love numbers in the time domain

To describe the time-evolution of the LNs, instead of the impulsive solution (3.108) it is more meaningful and physically intuitive to consider a load imposed at time $t = 0$ and held in place thereafter, as it is customarily done in glacial isostatic adjustment studies (Spada et al., 2011). Since the Laplace transform of a Heaviside step function $H(t)$ is $1/s$, the corresponding LN is $\tilde{x}^H(s) = \tilde{x}(s)/s$. After multiplication of Eq. (3.108) by $1/s$,

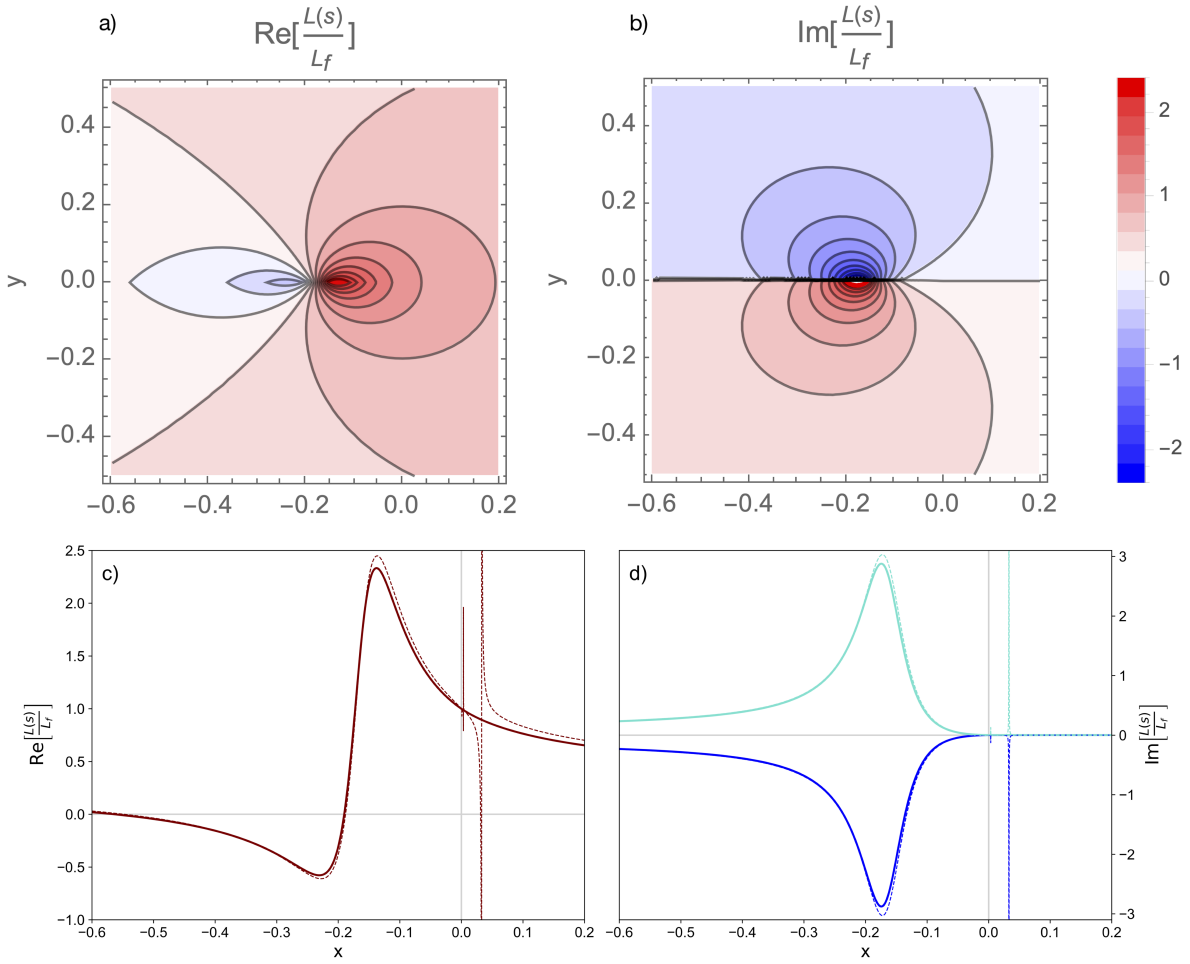

Figure 3.4: Contour plots of the real part (a) and of the imaginary part (b) of $F(z) = \tilde{L}(z)/x^F$, for an Andrade sphere with α=$\frac{1}{3}$, c=4 and ζ=1. In (c), the real part is shown along the real axis while in (d), the imaginary part is plotted along two axes just above and just below the x-axis, defined by y=$\pm 10^{-4}$. In (c) and (d), dashed lines show numerical results for the ratio between the h_2 tidal LN of a compressible sphere and its fluid limit.

it is possible to write the Heaviside LN in the computationally convenient form:

$$\frac{\tilde{x}^H(s)}{x^F} = \frac{1}{s} - \frac{c\tau_M}{(1+c)(s\tau_M) + \zeta^{-\alpha}\Gamma(1+\alpha)(s\tau_M)^{1-\alpha} + 1}\,, \tag{3.109}$$

and it is easily shown that, in the limit $\zeta \to \infty$, $\tilde{x}^H(s)$ reduces to the Laplace transform for the LN of a uniform Maxwell sphere, *i.e.*

$$\lim_{\zeta\to\infty} \frac{\tilde{x}^H(s)}{x^F} = \frac{1+s\tau_M}{(1+c)(s\tau_M)+1} = \frac{1}{s}\frac{1}{1+c\left(\dfrac{\tilde{\mu}_m(s)}{\mu}\right)}\,, \tag{3.110}$$

where $\tilde{\mu}_m(s)$, defined in (3.107), is the complex shear modulus appropriate for the 1-D Maxwell rheological body (*e.g.,* Mainardi and Spada, 2011).

Assuming that $\alpha = p/q \leq 1$, where p and q are integers, the r.h.s. of Eq. (3.109) can be Laplace-inverted in closed-form following the same approach adopted to invert $\tilde{G}_a(s)$ in Section 2.2. Indeed, with the aid of *Mathematica©* (Wolfram Research, Inc., 2024), we have verified that the time-domain Heaviside LN can be cast in the form:

$$\frac{x^H(t)}{x^F} = 1 - \Phi_{p,q}(t)\,, \quad t \geq 0\,, \tag{3.111}$$

where we have defined

$$\Phi_{p,q}(t) = \frac{c}{\left(\dfrac{t}{\tau_M}\right)^{1-\frac{1}{q}}} \sum_{k=1}^{q} \left(\frac{E_{\frac{1}{q},\frac{1}{q}}\left(\left(\dfrac{t}{\tau_M}\right)^{\frac{1}{q}} z_k\right)}{\frac{q-p}{\zeta^{p/q}}\Gamma\left(1+\frac{p}{q}\right) z_k^{q-p-1} + q(1+c) z_k^{q-1}} \right)\,, \tag{3.112}$$

and where the z_k's are the (distinct) roots of the algebraic equation $F_{p,q}(x) = 0$, with $F_{p,q}(x) = P_{p,q}(x) + cx^q$, with polynomial $P_{p,q}(x)$ defined by Eq. (2.16). Notice that the z_k's are themselves depending upon parameters c and ζ. Since the properties of the Mittag-Leffler function ensure that $\lim_{t\to+\infty} \Phi_{p,q}(t) = 0$, in Eq. (3.111) condition

$$\lim_{t\to+\infty} x^H(t) = x^F \tag{3.113}$$

is met, as it is expected for consistency. We have also verified that, through a repeated application of De L'Hôpital's rule and some cumbersome calculations, that

$$\lim_{t\to 0^+} \Phi_{p,q}(t) = \frac{c}{1+c}\,, \tag{3.114}$$

and thus, in other words, the elastic limit reads:

$$x^H(0^+) = \frac{x^F}{(1+c)}\,. \tag{3.115}$$

To corroborate the mathematical result given by Eqs. (3.111) and (3.112), we have obtained independent numerical results by the `ALMA`^{3} planetary LNs calculator (Melini et al., 2022). `ALMA`^{3} is a code that implements the Post-Widder Laplace inversion technique (Post, 1930; Widder, 1934) for spherically symmetric models with general incompressible linear viscoelastic rheology (Spada and Boschi, 2006; Spada, 2008). Figure 3.5, obtained using a uniform model whose parameters are listed in the caption, considers various combinations of the α and ζ parameters. The match between the analytical (solid curves) and numerical results (dotted) is very satisfactory, with a relative error never exceeding the 0.1% level. Notice that the LNs are characterized by short timescale (elastic) and long timescale (fluid) asymptotes that are not influenced by the value of parameter α. However, the transition from elastic to fluid regimes is controlled by the value of α, with the response becoming slower for decreasing α.

To study the sensitivity of the LNs to the model parameters, in Figure 3.6 we consider the tidal LN $k_2^H(t)$, a quantity of fundamental importance in planetary studies since it characterizes the tidal response of the body. Figure 3.6a shows the LN $k_2^H(t)$, obtained from Eq. (3.111) with $\alpha = 1/3$ and $\zeta = 1$ as a function of time, for various values of the normalized shear modulus μ' characterizing distinct hypothetical planetary models. Since $\mu' \propto \mu/(\rho\, a)^2$, a small μ' may correspond to a low-rigidity planet (small μ) or to a body with with large a and/or ρ (hence a large gravity at the surface). Conversely, a large μ' value may correspond to an elastically stiff planet (large μ) and/or to a small-radius and a low-density body. We notice that for an Earth-like planet, $\mu' \approx 0.4$ (see Table 3.2).

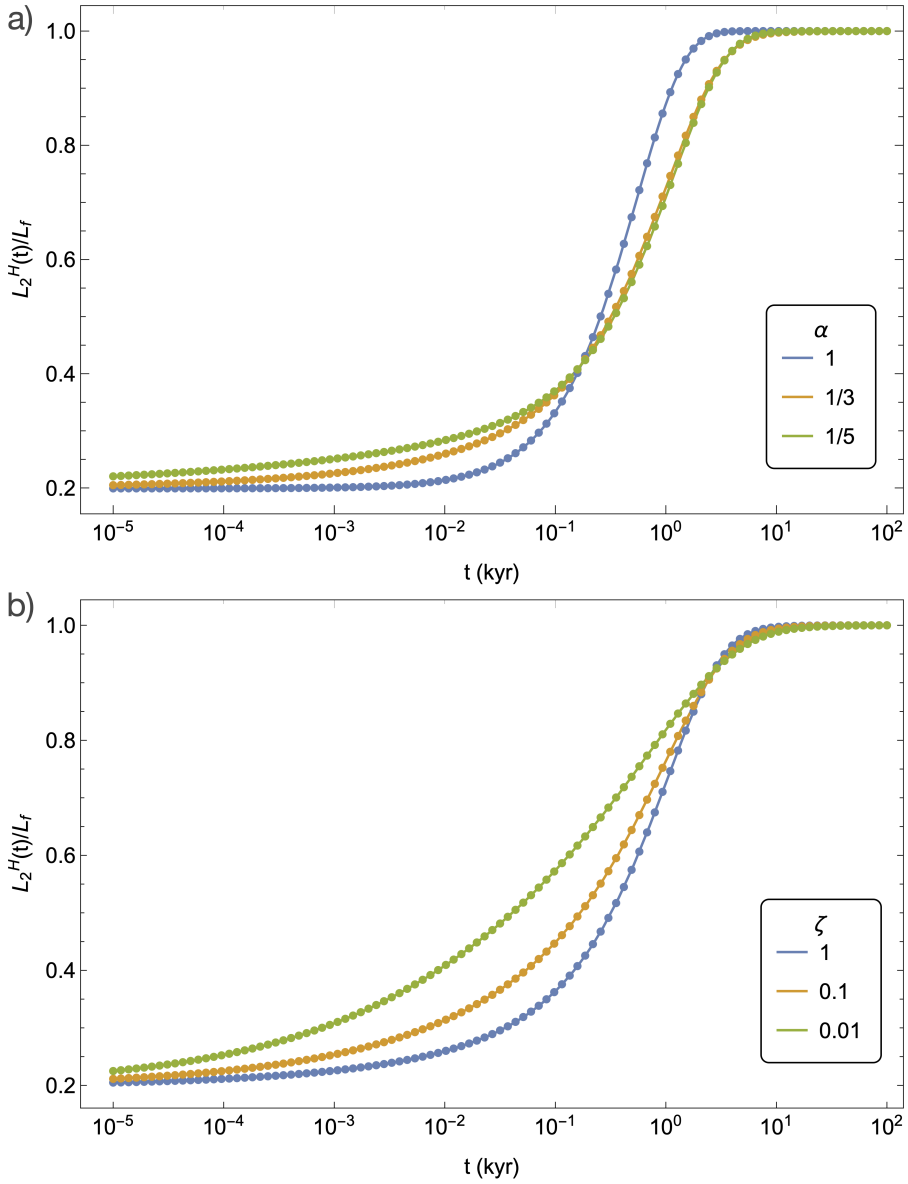

Figure 3.5: Comparison between LNs obtained analytically (solid curves) and numerically by the ALMA^3 code (dotted). A homogeneous Andrade planet is assumed, with radius $a = 6371\ km$, elastic shear modulus $\mu = 1.46 \times 10^{11}\ Pa$, Newtonian viscosity $\eta = 10^{21}\ Pa \cdot s$ and density $\rho = 5514 kg \cdot m^{-3}$. Curves in (a) and (b) are obtained by setting $\zeta = 1$ and $\alpha = 1/3$, respectively. All numerical experiments with ALMA^3 have been carried out in a multi-precision environment using 128 digits.

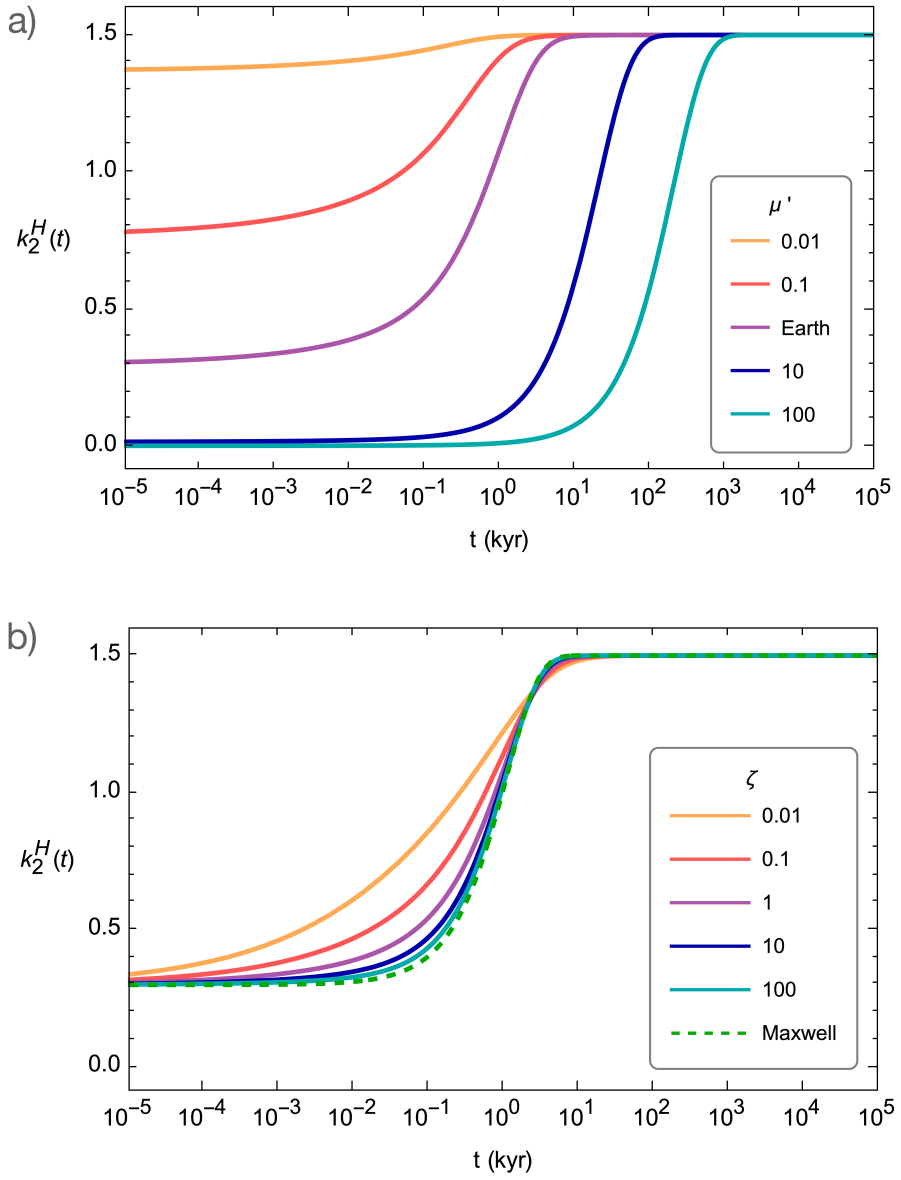

Figure 3.6: Tidal Heaviside LN $k_2^H(t)$ for a uniform Earth-like planet with viscosity $\eta = 10^{21}\ Pa \cdot \mathrm{s}$ and $\alpha = 1/3$. In (a), $\zeta = \tau_A/\tau_M = 1$, and results for different values of the normalized shear modulus μ' are shown. In (b) we have used $c = 4$, corresponding to $\mu' \approx 0.4$, and curves for different values of parameter ζ are shown. The dashed curve shows the Maxwell response, attained for values of $\zeta \gg 1$.

From Figure 3.6a it is apparent that the value of μ' has a strong influence on the evolution of $k_2^H(t)$. In particular, the elastic response $k_2^H(0)$ increases with decreasing μ', which is expected since the initial deformation is large for a low-rigidity body. Furthermore, the transition to the fluid limit $k_2^H(\infty) = 3/2$ is characterized by a time scale that increases with increasing μ', since stiff bodies relax slowly. However, Figure 3.6 shows that, as expected, the fluid limit attained for $t \to \infty$ is not dependent upon μ'.

In Figure 3.6b, the $k_2^H(t)$ LN is shown for an Earth-like planet, assuming $\alpha = 1/3$, $c = 4$ and varying ζ in the range between 10^{-2} and 10^2. As expected, the choice of ζ does not affect the elastic and fluid limits, which are controlled by the μ' parameter, but it affects significantly the transition between the two regimes. Indeed, as we have discussed in Section 2.2, the values of ζ control the relative importance of the transient and steady-state terms, with the former becoming negligible for increasing values of ζ. The dashed curve in Figure 3.6b shows the $k_2^H(t)$ Heaviside LN for a Maxwell rheology. As ζ increases, the response of the Andrade rheology approaches the Maxwell curve, with a close match for $\zeta = 10^2$. We have also verified analytically that, by virtue of the properties of the Mittag-Leffler functions, the expression (3.111) for $x^H(t)$ reduces to that of a Maxwell rheology for $\zeta \to \infty$. The procedure is formally identical to that followed in Section 2.2.3 for the calculation of the limit for $\zeta \to \infty$ of the relaxation modulus, with the exception of the presence of a multiplicative factor $(1 + c)$.

Chapter 4

Methods

This chapter is devoted to the description of the methods I followed to obtain the final results presented in Chapter 5. More specifically, I delve into the main steps of the computation of the horizontal and vertical components of the displacement field at the surface and the geoid height variation in response to surface unloading. These fields, also referred to as Surface Response Functions (SRFs), are the result of three-dimensional convolutions between suitable Green Functions (GFs), representing the Earth's model characteristics, and proper "Load Functions" (LFs), that describe the load evolution in space and time. For more details about these calculations the reader is referred to Spada (2003).

First, in Section 4.1, I describe the Earth's models that I have employed for the experiments presented in the next chapter. All the models include a elastic lithosphere, a viscoelastic shallow upper mantle and deep upper mantle, a viscoelastic lower mantle and a fluid core. Hence, in view of the complexity of the Earth's models, to compute the LNs I relied on `ALMA` (Melini et al., 2022), a LNs calculator that will be briefly presented in Section 4.2. Also, in this same Section, I show several examples of `ALMA`'s output: indeed, already from the LNs, it is possible to draw useful preliminary information about the Earth's models response. Finally, I briefly expose the main step needed to compute

the Surface Response Function (SRF) in Section 4.3. For the sake of completeness, in Section 4.4, I report the time convolutions needed for the computation of the SRF concerning two particular types of load history which are of interest for this Thesis, namely the Heaviside and Ramp unloading ice histories.

4.1 Earth's models

In this section I briefly describe the Earth's models that I have considered in my ensuing experiments. I remark that for these computations, I have considered a spherically symmetric incompressible Earth (1D models). All the models are composed of five layers, that is (from the outermost to the innermost):

- An Elastic Lithosphere, whose thickness d_l varies in some experiments (90, 110, 130 and 150 km),
- A Viscoelastic Shallow Upper Mantle (SUM), i.e. the outermost part of the mantle. In many experiments I employed different values for the viscosity, ranging between $5 \cdot 10^{18}$ and $1 \cdot 10^{20}$ $Pa \cdot s$,
- A Viscoelastic deep upper mantle (DUM), with a fixed viscosity of $1.0 \cdot 10^{20} Pa \cdot s$,
- A Viscoelastic lower mantle (LM), with a fixed viscosity of $1.0 \cdot 10^{22} Pa \cdot s$,
- A fluid, inviscid and homogeneous core.

In addition to the thickness of the lithosphere and the viscosity of the SUM, I also tested the sensitivity of the SRF to the rheological *configuration* of the mantle, i.e. the various combinations of rheological laws (Andrade or Maxwell) employed to describe the mantle layers. In particular, I considered three different cases:

- "Maxwell": SUM; DUM, and LM are all characterized by a Maxwell's rheology.

Layer	Radius (10^6 m)	Dens. (kg/m^3)	Rig. (10^{10} Pa)	Visc. ($Pa \cdot s$)	Rheo.
Litho.	6.371	2854.6	4.49	-	Elastic
SUM	6.371− $\boldsymbol{d_l}$	3550.0	7.12	$\boldsymbol{\eta_{SUM}}$	**And/Max**
DUM	5.951	3801.7	14.5	$1.0 \cdot 10^{20}$	**And/Max**
LM	5.701	4877.9	22.0	$1.0 \cdot 10^{22}$	**And/Max**
Core	3.480	10931.7	-	-	Fluid

Table 4.1: Scheme used for the implementation of the Earth's models. Each column reports the radius (upper boundary), density, rigidity, viscosity and rheology relative to the indicated layer. The parameters in blue are those which were varied in the experiments: the lithospheric thickness, d_l, which can assume the values 90, 110, 130 and 150 km, the viscosity of the SUM, η_{SUM}, which can assume the values in a range included between $5.0 \cdot 10^{18}$ and or $1.0 \cdot 10^{20}$ $Pa \cdot s$, and the rheology of the mantle, which could be set by choosing between the Maxwell (Max) and the Andrade (And) model.

- "Andrade": SUM; DUM, and LM are described by Andrade rheology. Andrade parameters are set to $\alpha = 1/3$ and $\zeta = 1$ respectively.
- "Andrade+Maxwell": Andrade's rheology describes the SUM, while the rest of the mantle is characterized by a Maxwell's rheology.

In the following, I will use the terms "Maxwell", "Andrade" and "Andrade+Maxwell" to refer to one of these rheological *configurations*. These models are summarized by the scheme of Table (4.1), where the entries in blue are those which could change in the various experiments.

A remarkable weakness of this approach is the low degree of details of the lithosphere. Of course, especially for loads of small to medium spatial scale, the layering of the lithosphere is important to correctly assess the SRF. A thinner lithosphere allows the load to be "more in contact" to the viscous layer of the Earth, which, consequently, lay

closer to the surface. As we will see later in Chapter 5, this has important consequences on the magnitude of the observed rates. However, assuming a uniform, compact *purely elastic* lithosphere allows us to attribute, if present, any transient or inelastic feature of the SRF directly to the viscoelastic mantle. I made this choice to focus the attention on the viscoelastic layers of the Earth's model rather than on the elastic parameters of the lithosphere. For this reason, I remark here that the effects of the rigidity of the lithosphere are not investigated in this Thesis. Instead, the role of the lithospheric thickness d_l is considered since it has direct consequences both on the thickness of the underlying SUM and on the distance of the latter from the surface.

4.2 ALMA: the plAnetary Love nuMbers cAlculator

In the previous chapter we saw that the existence of closed-form or analytical solutions for LNs is limited to very few fortunate cases, concerning extremely simple models. As already argued, these formulae are important to understand the role of the model parameters, but when it comes to the study of more sophisticated models, numerical solutions are necessary. This is the case of GIA studies: in this field, a minimum of three layers is necessary (elastic lithosphere, viscoelastic mantle, fluid outer core) to suitably model the Earth response (see *e.g.,* Whitehouse, 2018). For this reason, in this thesis work in which I consider 5-layer Earth's models, I employed `ALMA` (Melini et al., 2022) for the numerical computation of LNs. In this section, I briefly illustrate the ideas behind this program, also showing and discussing some out the outputs obtained.

4.2.1 Some words about `ALMA`

In 1974, W. Peltier introduced the "Viscoelastic Normal Modes" method (Peltier, 1974). For a basic introduction about this topic, let's consider a layered incompressible viscoelastic planet subject to an impulsive δ-like load: once again, we seek for the solutions

at the surface of the vertical and horizontal components of the displacement field and the incremental potential. To do so, as I have shown in Section 3.3, that through the application of the correspondence principle, one can solve the corresponding elastic problem in the Laplace domain. The solution vector $\tilde{\boldsymbol{z}}(s) = (\tilde{y}_1, \tilde{y}_2, \tilde{y}_5)^T$ reads:

$$\tilde{\boldsymbol{z}}(s) = (\boldsymbol{P}_1 \boldsymbol{\Lambda}(s) \boldsymbol{J}) \, (\boldsymbol{P}_2 \boldsymbol{\Lambda}(s) \boldsymbol{J})^{-1} \, \boldsymbol{b} \,, \tag{4.1}$$

where $\boldsymbol{J}$ is a matrix that accounts for the BCs at the CMB (*e.g.,* Sabadini et al., 2016), $\boldsymbol{b}$ is the vector containing the loading or tidal BCs (see Eqs. 3.38 and 3.39), and

$$\boldsymbol{\Lambda}(s) = \prod_{k=N}^{1} \boldsymbol{Y}_k(r_{k+1}, s) \boldsymbol{Y}_k^{-1}(r_k, s) \,, \tag{4.2}$$

with N being the number of layers in addition to the core, r_k is the radius of the interface between the $(k-1)$-th and the k-th layer, with $r_1 \leq ... \leq r_N$, $r_1 = r_c$ and $r_{N+1} = r_c$ and $r_{N+1} = a$ is the planet radius (Melini et al., 2022). The similarity between Eq. (4.1) and Eqs. (3.88), (3.47) is clear: these formulae express the *propagation* of the solution from the centre of the planet to the surface, accounting for all the BCs between each internal interface. For the Kelvin model, this method allows to find a solution that simultaneously respects the BCs at the surface and does not diverge at $r = 0$, while for the two-layered fluid planet, the solution accounts for the presence of a density discontinuity. However, seen the small number of layers (one and two respectively), a formal definition of the propagation matrix was indeed not necessary. Here, by means of $\boldsymbol{\Lambda}(s)$, the solution is propagated from the fluid core, whose BCs are imposed through the interface matrix $\boldsymbol{J}$, to the outer layers, up to the surface, where the BCs are set via $\boldsymbol{b}$.

From the solution of Eq. (4.1), one can obtain the LNs in the Laplace domain:

$$\tilde{h}_n(s) = \frac{m}{a} \tilde{u}_n(s) \,, \tag{4.3}$$

$$\tilde{l}_n(s) = \frac{m}{a} \tilde{v}_n(s) \,, \tag{4.4}$$

$$\tilde{k}_n(s) = -\left(1 + \frac{m}{ag} \tilde{\varphi}_n(s)\right) \,. \tag{4.5}$$

Then, using Cauchy's residue theorem, we can recast the last three equations in the following form:

$$\tilde{x}_n(s) = x_n^E + \sum_{k=1}^{M} \frac{x_{n,k}^V}{s - s_n^k} \tag{4.6}$$

where $\tilde{x}_n(s)$ is any of the three LNs, x_n^E is the corresponding elastic limit, $x_{n,k}^V$ and M are the viscoelastic components of LNs and the number of viscoelastic normal modes respectively, and the s_n^k are the (real and negative) roots of the secular equation $Det(\boldsymbol{P}_2\boldsymbol{\Lambda}(s)\boldsymbol{J}) = 0$ (see, *e.g.*, Melini et al., 2022). In the time domain the previous equation reads (as previously presented in Section 3.3):

$$x_n(t) = x_n^E \delta(t) + H(t) \sum_{k=1}^{M} x_{n,k}^V e^{s_n^k t} \tag{4.7}$$

Unfortunately, the application of this model gets increasingly difficult as the planet layering becomes thinner and/or when more realistic rheologies are employed (more details can be found in Melini et al. (2022), Spada (2008), Spada and Boschi (2006)).

The calculation of the LNs for the Earth's model of interest of this thesis was performed with `ALMA`, the plAnetary Love nuMbers cAlculator (Melini et al., 2022; Spada, 2008), a program based upon the Post-Widder formula, that represents an alternative to the VNM method. However, for the purpose of this thesis, by courtesy of my co-supervisor Dott. D. Melini, I used a newer version of `ALMA`, still under development. This new version implements the so called "Collocation Method", introduced by Schapery (1962*a*,*b*), which is based on an approximation of the multi-exponential form of LNs (3.59):

$$\boldsymbol{x}(t) = \boldsymbol{x}^E \delta(t) + \boldsymbol{x}^{*V}(t)\,, \tag{4.8}$$

where each component of $\boldsymbol{x}^{*V}(t)$ shall be written as

$$x^{*V}(t) = \sum_{i=1}^{n} a_i e^{-t/\alpha_i}\,, \tag{4.9}$$

where the a_i coefficients are numerically determined to minimize the misfit between x^{*V} and x^V, and where the number of n terms and α_i are fixed *a priori* (Mitrovica and Peltier, 1992). Thus, differently from the previous versions of `ALMA`, whose output consisted in Real and Complex LNs, with the collocation analysis the results are the elastic and viscoelastic parts of the LNs for a set of selected time steps. As we will see later, this form of LNs greatly facilitates the implementation of the convolutions that I will present in Section 4.4.

4.2.2 Computing the Love numbers with `ALMA`

In this section I present the LNs of some Earth's models used to obtain the results presented in the next chapter. Here I consider the standard form of LNs ($k_n(t)$, $h_n(t)$, $l_n(t)$) in the time domain, since for the aims of this thesis, showing their evolution through time at each harmonic degree could help in the interpretation of the final result presented in the next chapter. Even if the full response to a particular input load is to be obtained through the SRF, we can foresee its main features (in general terms, at least) already from the time evolution of its LNs.

General features of Love Numbers in the time domain

Figure 4.1 shows the LNs $k_n(t)$, $h_n(t)$, and $l_n(t)$ in the time domain for the "Andrade" configuration with $\eta_{SUM} = 5.0 \cdot 10^{19} Pa \cdot s$ and $d_l = 110\ km$. The purpose of this figure is showing the general features of time domain LNs. With the exception of higher degrees LNs ($n \geq 400$, third row), we can distinguish three phases: an initial one, characterized by a constant value, followed by a transition that leads to a third and final phase, characterized again by a constant behavior. The initial and final phase are called "elastic" and "fluid" regimes, respectively. Basically, since the model has viscoelastic layers, if the characteristic time t of the perturbation is too short, the model will respond in an elastic way (elastic regime). On the contrary, on sufficiently long time-scales, the

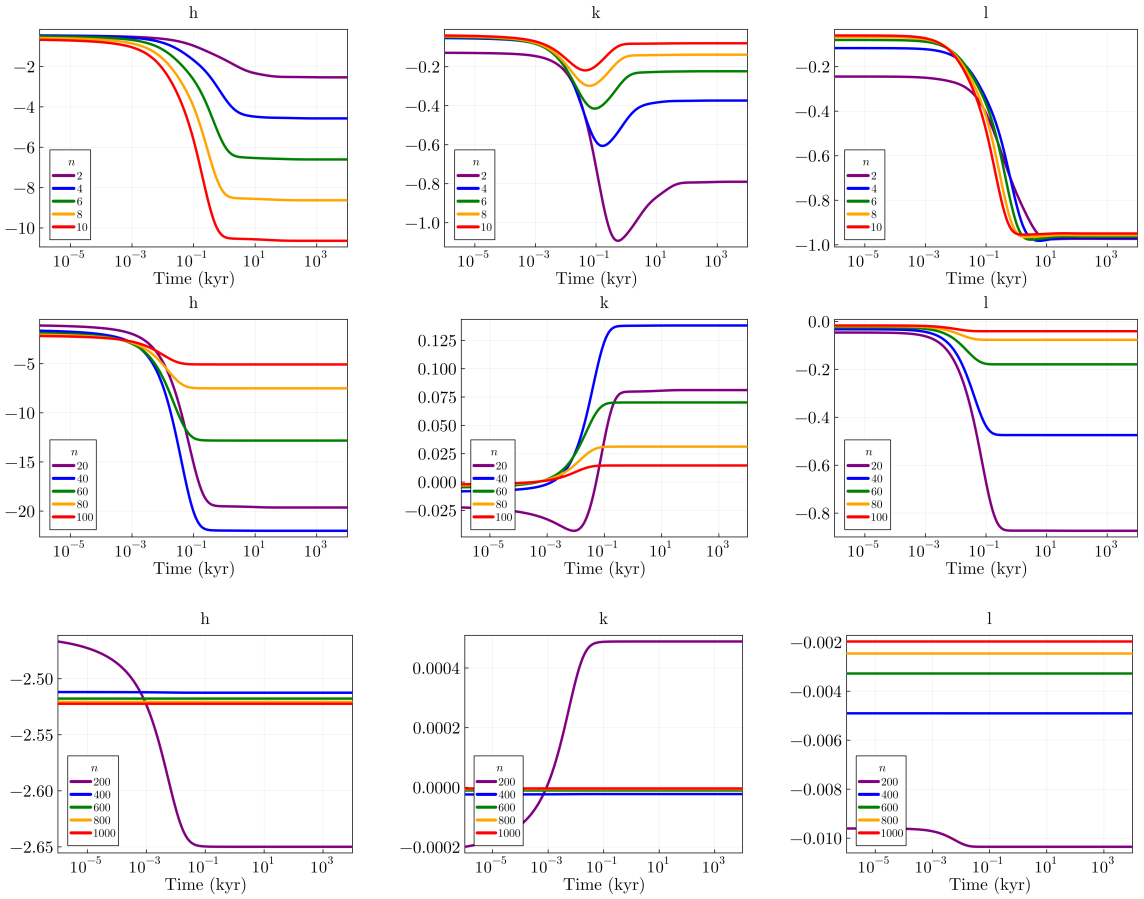

(a) $h(t)$ (b) $k(t)$ (c) $l(t)$

Figure 4.1: **LNs $h(t)$, $k(t)$, $l(t)$ of the "Andrade" configuration** with SUM viscosity $\eta_{SUM} = 5.0 \cdot 10^{19} Pa \cdot s$ and $d_l = 110\ km$ for various values of harmonic degree n.

model exhibits a fluid behavior (fluid regime).

On the other hand, for high harmonic degrees ($n \geq 400$, third row), it seems that the fluid limit coincides with the elastic one. It is important to recall that each harmonic degree is connected to a spatial scale. Lower degrees are associated to longer wavelengths, while larger degrees are connected to more local features. Since the first 110 km of the Earth's model are composed by an elastic lithosphere, we can expect that all the harmonic degrees exceeding a certain value, will only "see" this layer, exhibiting thus the characteristic constant trend represented by the elastic limit value. Similar results were found in Boughanemi and Mémin (2024), who considered an elastic lithosphere 100 km thick. This fact is confirmed also by a Rule of thumb known as "the Jeans rule" Jeans (1923), that relates the spatial scale λ (or wavelength) to the harmonic degree n:

$$\lambda = \frac{2\pi a}{n + 1/2}\,, \tag{4.10}$$

where a is the radius of the planet. With λ set to 110 km, it turns out that $n \sim 360$.

Effects of the rheological law

Figure 4.2 scopes the role of the mantle rheology on LNs $h(t)$, $k(t)$ and $l(t)$. The three configurations presented in Section 4.1 are considered: "Maxwell" in the first row, "Andrade" in the second and "Andrade+Maxwell" in the third. I chose to plot the LNs of degrees $20, 30, 40, 80$, since they should reflect contribution mainly due to the mantle layers. By comparing each row, we should not be surprised by the similarity of the curves obtained for the different rheological configurations. The main differences between them, especially between "Andrade", "Andrade+Maxwell" *and* "Maxwell" occur during the elastic phase and the "transitory" phase (hereafter, the term "transitory" is used to describe the phase in between the elastic and fluid regimes, and it has nothing to do with the rheological "transient"). By a careful examination, it is possible to see that Andrade's model have a shorter elastic phase, that with respect the Maxwell one,

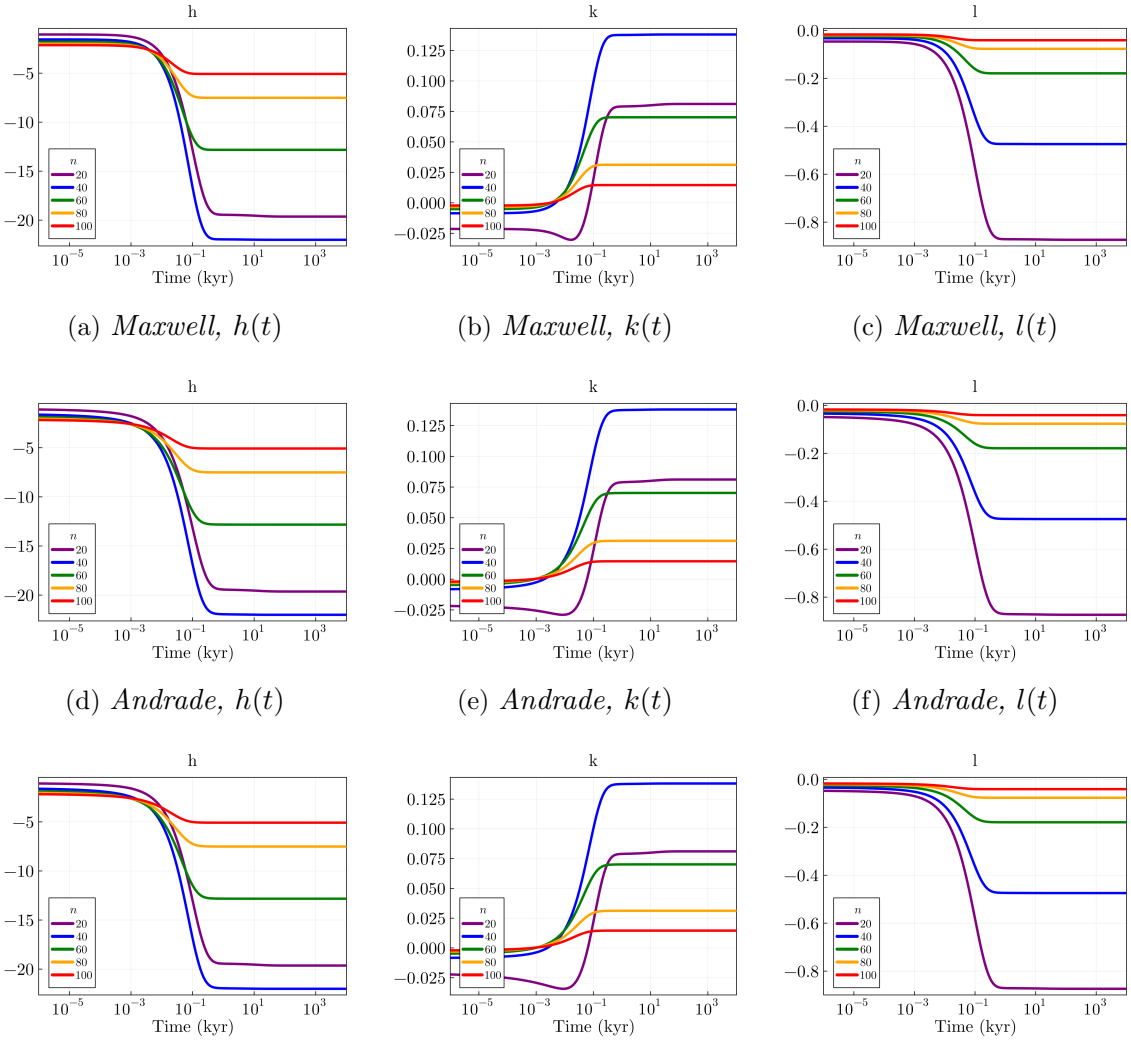

(a) *Maxwell*, $h(t)$ (b) *Maxwell*, $k(t)$ (c) *Maxwell*, $l(t)$

(d) *Andrade*, $h(t)$ (e) *Andrade*, $k(t)$ (f) *Andrade*, $l(t)$

(g) *Andrade+Maxwell*, $h(t)$ (h) *Andrade+Maxwell*, $k(t)$ (i) *Andrade+Maxwell*, $l(t)$

Figure 4.2: **LNs $h(t)$, $k(t)$, $l(t)$ of the three rheological configurations "Maxwell"** (first row), **"Andrade"** (second row) and **"Andrade+Maxwell"** (third row). The lithospheric thickness is set to $d_l = 110\ km$ and the viscosity $\eta_{SUM} = 1.0 \cdot 10^{20}\ Pa \cdot s$. The models with Andrade's rheology in the SUM have a slightly smother transition between the elastic and fluid regime. Although the differences seem negligible, I remark that the time axis is logarithmic and that the time-scales of interest of the tests shown in the next chapter are of the order of $10^{-3}, 10^{-2}\ kyr$.

starts immediately (even if slowly) to evolve. Basically, we see that while the Maxwell configuration is still in its elastic regime, the Andrade's ones are already in a *anelastic* stage, which, in principle, should be responsible of the transient phase that we will see in the SRF. This is more evident in $h(t)$ and $k(t)$ than in $l(t)$.

Effects of Viscosity

As we can see from Figure 4.3, the effects of viscosity on LNs are extremely evident. The shape of the curves remains the same, but the *transition* between the elastic and fluid regime is shifted in time: lower viscosities mean earlier transitions. The reason is easily said: changing the magnitude of mantle's viscosity means modifying the relaxation time of the model. Less viscous models will start *flowing* earlier. Except from this, viscosity does not cause any other significant modifications. However, as we will see later, this variation is the one that produces the most evident consequences in the SRF.

Effects of Lithospheric Thickness

The sensitivity of LNs to the thickness of the lithosphere d_l is considered in Figure 4.4. The values accounted are $d_l = 90\ km$, $110\ km$, $130\ km$ and $150\ km$. It is important to remark that, differently from the other cases presented earlier, in this one the total mass of the Earth's model changes, since the lithospheric density is kept constant. However, these results appear quite interesting: the elastic limit does not change significantly following a variation in the lithosphere's thickness, while this is not the case for the fluid limit, that exhibits different values. This finding is true for the LNs $h(t)$ and $k(t)$, while $l(t)$ does not seem to be very sensitive to the lithospheric thickening. To explain this trait, I could speculate that, as regard the horizontal displacement, Jean's rule may be a little different: even the shallowest model considered ($d_l = 90\ km$) is already too thick to allow these displacements to be sensitive to any other parameters. Another feature that we can appreciate concerns the amplitude of the transitory phase: as the lithosphere

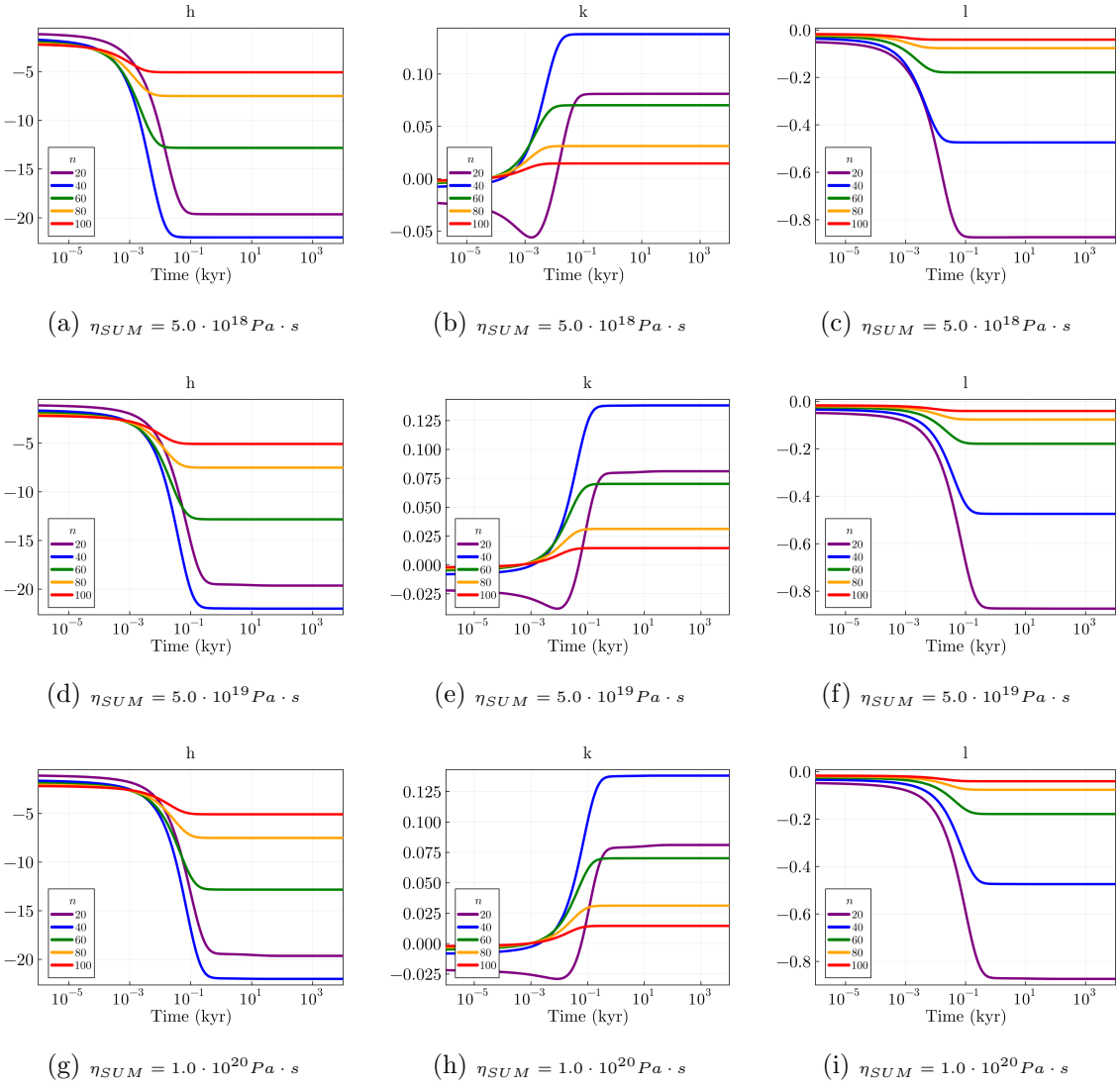

(a) $\eta_{SUM} = 5.0 \cdot 10^{18} Pa \cdot s$ (b) $\eta_{SUM} = 5.0 \cdot 10^{18} Pa \cdot s$ (c) $\eta_{SUM} = 5.0 \cdot 10^{18} Pa \cdot s$

(d) $\eta_{SUM} = 5.0 \cdot 10^{19} Pa \cdot s$ (e) $\eta_{SUM} = 5.0 \cdot 10^{19} Pa \cdot s$ (f) $\eta_{SUM} = 5.0 \cdot 10^{19} Pa \cdot s$

(g) $\eta_{SUM} = 1.0 \cdot 10^{20} Pa \cdot s$ (h) $\eta_{SUM} = 1.0 \cdot 10^{20} Pa \cdot s$ (i) $\eta_{SUM} = 1.0 \cdot 10^{20} Pa \cdot s$

Figure 4.3: **LNs $h(t)$, $k(t)$, $l(t)$ of "Andrade" model, with lithospheric thickness $d_l = 110\ km$ for different values of η_{SUM}.** More precisely, $\eta_{SUM} = 5.0 \cdot 10^{18} Pa \cdot s$ in the first row, $\eta_{SUM} = 5.0 \cdot 10^{19} Pa \cdot s$ in the second and $\eta_{SUM} = 1.0 \cdot 10^{20} Pa \cdot s$ in the third. Here we can appreciate that the viscosity "shifts" (in time) the transition between the elastic and fluid regimes.

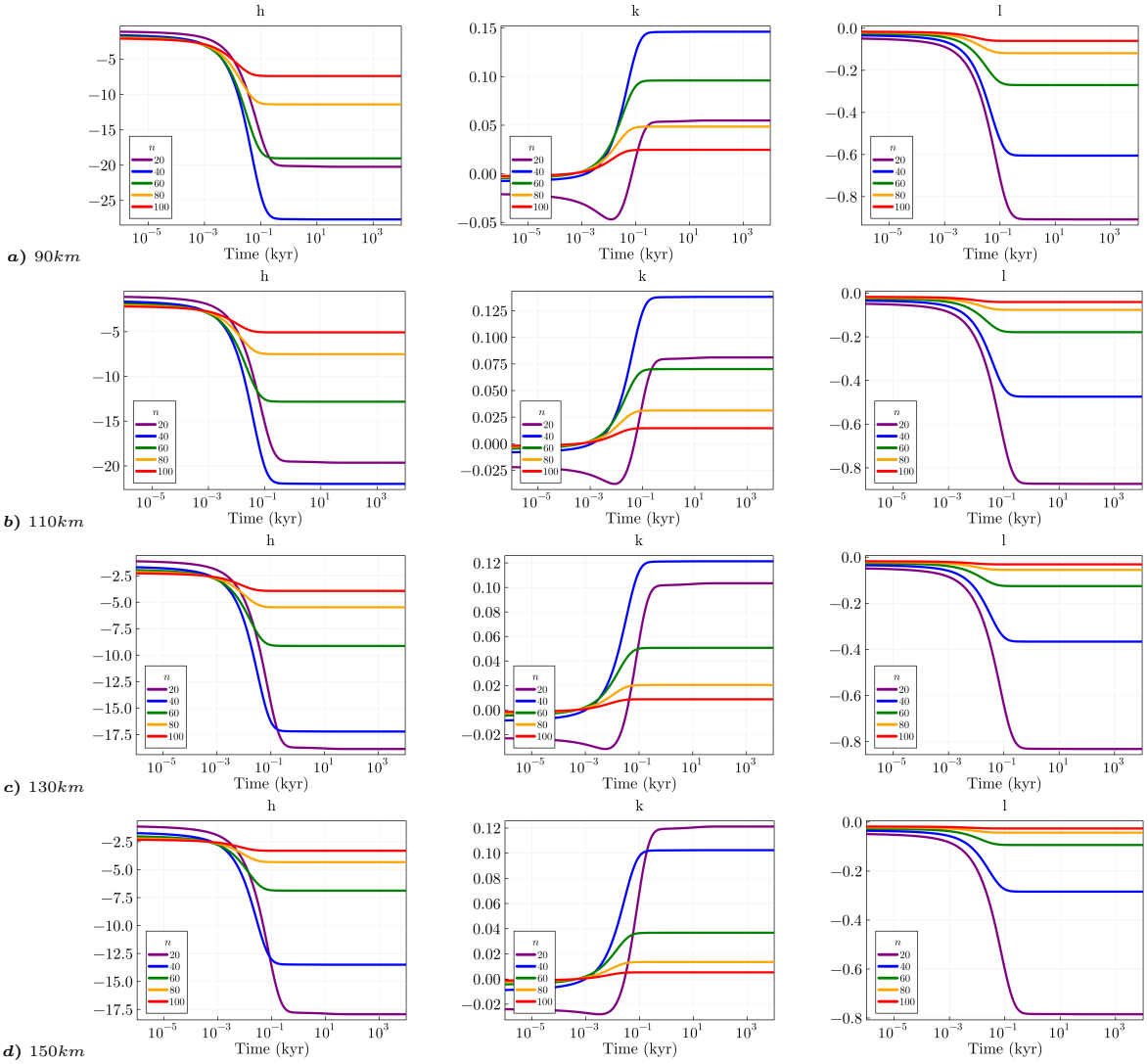

Figure 4.4: **LNs $h(t), k(t), l(t)$ of "Andrade" model, with $\eta_{SUM} = 5.0 \cdot 10^{19} Pa \cdot s$ for different values of the lithospheric thickness.** Each row shows a different case, *i.e.*, $d_l = 90\ km$, $110\ km$, $130\ km$ and $150\ km$.

width increases, the gap between the fluid and elastic regime diminishes, making the value of the fluid limit more and more similar to that of the elastic one. In other words, thicker lithospheres make the Earth's models more elastic and less viscous.

4.3 Surface response functions

The calculation present in this section follows Spada et al. (2003). For more details, the reader is referred to the book "The theory behind TABOO" distributed with the code at https://github.com/danielemelini/TABOO.

In mathematics, given a linear differential operator $\mathcal{D} = \mathcal{D}(x)$ acting on the collection of distributions over a subset Ω of some Euclidean space $\mathbb{R}^n$, a Green's function $\Gamma = \Gamma(x, s)$ at the point s in Ω corresponding to $\mathcal{D}$, is any solution of

$$\mathcal{D}\Gamma(x, s) = \delta(x - s)\,, \tag{4.11}$$

where δ denotes the Dirac's delta function. More generally, we can see the GF as the response of a system to a unit impulse at a certain time $t = t'$ (Boas, 2006).

In the scope of the surface load problem, the GFs express the response (in terms of a certain observable, such as the displacement field) of the Earth's model to a impulsive unit load. Through a convolution with a suitable function that describe the load evolution (*i.e.,* the "Load Function") , it is possible to obtain the so called "Surface Response Function" (SRF). In other words:

$$\mathrm{SRF}(\gamma, t) = (\Gamma \otimes \mathcal{L})(\gamma, t) = \int_{-\infty}^{\infty} dt' \int_{earth} \Gamma(\psi, t - t')\mathcal{L}(\gamma', t')dA'\,, \tag{4.12}$$

where $\gamma = (\theta, \lambda)$ is the point at which the SRF is evaluated, Γ is the GF, $\mathcal{L}$ is the load function describing the load geometry and history, ψ is the angular distance between the impulsive point load of the GF and γ, and the $\int_{earth}$ stands for the integration over the Earth's surface. The SRF is the final product of the calculations, that includes all the information regarding how the Earth's model responds to the load evolution. In the

following, we will see how to obtain a SRF for a *compensated* disc-shaped ice load, *i.e.* a type of load which accounts for the principle of mass conservation (PMC).

In view of the geometry of the problem, to ease the calculations that will follow, we start by writing the GFs in the following way (Spada, 2003):

$$\Gamma(\alpha, t) = \frac{a}{m_e} \sum_{n=0}^{\infty} x_n(t) P_n(\cos\psi)\,, \tag{4.13}$$

with the x_n indicating one of the three loading LNs:

$$x_n(t) = \begin{cases} \delta(t) + k_n(t)\,, & \Gamma = \Gamma^g \quad \text{Geoid height} \\ h_n(t)\,, & \Gamma = \Gamma^u \quad \text{Vertical displacement} \\ l_n(t)\,, & \Gamma = \Gamma^g \quad \text{Horizontal displacement} \end{cases} \tag{4.14}$$

where in the particular case of the horizontal displacement I remark that it is necessary to substitute $P_n(\cos\psi)$ with its derivative with respect to with respect to ψ. Similarly, we will consider a general load function that can be expanded in complex spherical harmonics, such as:

$$\mathcal{L} = \sum_{nm} \mathcal{L}_{nm} \mathcal{Y}_{nm}\,, \quad \text{with} \quad \mathcal{L}_{nm} = \frac{1}{4\pi} \int_{\gamma} \mathcal{L}(\gamma, t) \mathcal{Y}^*{}_{nm}(\gamma) d\gamma\,, \tag{4.15}$$

being $\mathcal{Y}_{nm}$ the spherical harmonic function of degree n and order m, and $\mathcal{Y}^*{}_{nm}$ its complex

conjugate. In this way, we can decompose the SRF as follows:

$$
\begin{aligned}
\mathrm{SRF}(\gamma,t) &\equiv \int_{-\infty}^{\infty} dt' \int_e \Gamma\left(\psi, t-t'\right) \mathcal{L}\left(\gamma', t'\right) dA' \\
&= \int_{-\infty}^{\infty} dt' \int_\gamma \left(\frac{a}{m^e} \sum_{n=0}^{\infty} x_n\left(t-t'\right) P_n(\cos\psi) \right) \cdot \left(\sum_{n'm'} \mathcal{L}_{n'm'}\left(t'\right) \mathcal{Y}_{n'm'}\left(\gamma'\right) \right) a^2 d\gamma' \\
&= \frac{a^3}{m^e} \int_{-\infty}^{\infty} dt' \int_\gamma \left(\sum_{n=0}^{\infty} \frac{x_n\left(t-t'\right)}{2n+1} \sum_{m=-n}^{n} \mathcal{Y}^*_{nm}\left(\gamma'\right) \mathcal{Y}_{nm}(\gamma) \right) \cdot (\cdots) d\gamma' \\
&= \frac{a^3}{m^e} \sum_{nm} \frac{\mathcal{Y}_{nm}(\gamma)}{2n+1} \int_{-\infty}^{\infty} dt' x_n\left(t-t'\right) \sum_{n'm'} \mathcal{L}_{n'm'}\left(t'\right) \int_\gamma \mathcal{Y}^*_{nm}\left(\gamma'\right) \mathcal{Y}_{n'm'}\left(\gamma'\right) d\gamma' \\
&= \frac{4\pi a^3}{m^e} \sum_{nm} \frac{\mathcal{Y}_{nm}(\gamma)}{2n+1} \int_{-\infty}^{\infty} x_n\left(t-t'\right) \mathcal{L}_{nm}\left(t'\right) dt' \\
&= \sum_{nm} SRF_{nm}(t) \mathcal{Y}_{nm}(\gamma)\,,
\end{aligned}
\tag{4.16}
$$

where

$$
SRF_{nm}(t) = \frac{3\left(x_n(t) * \mathcal{L}_{nm}(t)\right)}{\rho_e(2n+1)} \tag{4.17}
$$

and where $\rho_e = \frac{3m^e}{4\pi a^3}$ is the Earth's average density, and $*$ indicates a time convolution. In this way we have reduced the original 3-D convolution to a simpler $1-D$ time convolution between the LNs and the Load Function.

From now on, we will assume that the load stems from two contributions:

$$
\mathcal{L}(\gamma,t) = \mathcal{L}_i + \mathcal{L}_w\,, \tag{4.18}
$$

where the first term, $\mathcal{L}_i$, accounts for the variations of the ice load, and $\mathcal{L}_w$ mimics complementary water-covered region needed to ensure the PMC. According to Spada (2024), we have:

$$
\mathcal{L}_i(\gamma,t) = \rho^i d^i(\gamma) \chi^i(\gamma) f^i(t)\,, \tag{4.19}
$$

where ρ^i, is the ice density (917 kg/m^3), $d^i(\gamma)$ is the ice thickness, $f^i(t)$ is the time history (a function describing the time evolution of the load), and $\chi^i(\gamma)$ is the ice mask function

$$\chi^i(\gamma) \equiv \begin{cases} 1\,, & \text{if} \quad \gamma \in i \\ 0\,, & \text{otherwise}\,. \end{cases} \tag{4.20}$$

As regard $\mathcal{L}_w(\gamma, t)$, one can write

$$\mathcal{L}_w(\gamma, t) = \rho^w d^w(t) \chi^w(\gamma)\,, \tag{4.21}$$

where ρ^w, is the water density (1000 kg/m^3), the water mask function is

$$\chi^w(\gamma) \equiv \begin{cases} 1\,, & \text{if} \quad \gamma \in w \\ 0\,, & \text{otherwise}\,, \end{cases} \tag{4.22}$$

and $d^w(t)$, the water thickness, is a variable to be determined in order to ensure the PMC. For this reason, $d^w(t)$ is time dependent and relies upon function $f^i(t)$.

I remark that this modeling approach is quite basic since during the experiments we assume that the areas of the two regions - ice and water - do not change and do not overlap. Now, in compliance with the PMC, for which the average of the load variation over the Earth surface must be zero,

$$\langle \mathcal{L}(\gamma, t) \rangle^{earth} = 0\,, \tag{4.23}$$

and by switching to the representation in terms of complex spherical harmonics, already introduced in Eq. (4.15), we can express the Load Function in the following way:

$$\mathcal{L}_{nm} = \rho^i f^i(t) d^{iw}_{nm} \mathcal{Y}_{nm}(\gamma)\,, \tag{4.24}$$

where d^{iw}_{nm} are suitable coefficients that account for both the ice and water part of the Load Function (that is why we have introduced the superscript ^{iw}) and the PMC:

$$d^{iw}_{nm} = d^i_{nm} - \left(\frac{d^i_{00}}{\chi^w_{00}} \right) \chi^w_{nm}\,. \tag{4.25}$$

By doing so, we are describing the so called "compensated load". Also, in the latter equation, d^i_{nm} and χ^w_{nm} are suitable coefficients of the expansion in complex spherical harmonics of the ice term $d^i(\gamma)\chi^i(\gamma)$ and the water-region mask $\chi^w(\gamma)$.

By substituting this expression into the convolution Eq. (4.16), we can recast it in the following way:

$$\begin{Bmatrix} \mathcal{U} \\ \mathcal{V}_\theta \\ \mathcal{V}_\lambda \\ \mathcal{G} \end{Bmatrix} (\gamma, t) \equiv \frac{3\rho^i}{\rho^e} \sum_{nm} \frac{d^{iw}_{nm}}{2n+1} \begin{Bmatrix} c^h_n(t) \\ c^\ell_n(t) \\ c^k_n(t) \end{Bmatrix} \cdot \begin{Bmatrix} 1 \\ \nabla_\theta \\ \nabla_\lambda \\ 1 \end{Bmatrix} \mathcal{Y}_{nm}(\gamma)\,, \tag{4.26}$$

where the time-convolutions are:

$$\begin{Bmatrix} c^h_n \\ c^\ell_n \\ c^k_n \end{Bmatrix} (t) \equiv \int_{-\infty}^{\infty} dt' \begin{Bmatrix} h^L_n \\ \ell^L_n \\ \delta + k^L_n \end{Bmatrix} (t-t')\, f^i\,(t')\ , \tag{4.27}$$

and where $\mathcal{U}$ is the vertical displacement SRF, $\mathcal{V}_\theta$ and $\mathcal{V}_\lambda$ are the co-latitudinal and longitudinal component of the horizontal SRF and $\mathcal{G}$ is the geoid height variation SRF.

We will now consider a disc-shaped load: this case is of particular interest, since it is one of the possible "axis-symmetric" loads. This scenario is schematically depicted by Figure 4.5. It consists of a disc of half-amplitude α (angle between the centre of the load and its border, measured *w.r.t* the geometrical centre of the Earth) over which height d^i is constant, and whose area defines the mask function

$$\chi^i(\theta) \equiv \begin{cases} 1 & 0 \le \theta \le \alpha \\ 0 & \alpha < \theta \le \pi\,. \end{cases} \tag{4.28}$$

As a consequence, the complementary mask function of the ocean will be:

$$\chi^w(\theta) \equiv \begin{cases} 0 & 0 \le \theta \le \alpha\,, \\ 1 & \alpha < \theta \le \pi\,. \end{cases} \tag{4.29}$$

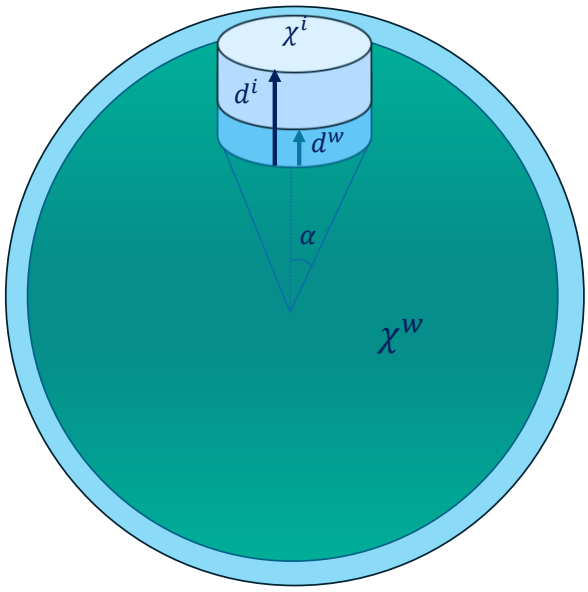

Figure 4.5: Sketch representation of a compensated disc load of half-amplitude α.

In this circumstance, the independence from the longitudinal coordinate γ allows us to access to a sequence of simplifications leading to a description of the SRF in term of Legendre polynomials, instead of complex spherical harmonics. The details on these calculations can be found in Spada (2003). The final result reads:

$$\left\{ \begin{array}{c} \mathcal{U} \\ \mathcal{V}_\theta \\ \mathcal{V}_\lambda \\ \mathcal{G} \end{array} \right\} (\theta, t) \equiv \frac{3\rho^i}{\rho^e} \sum_{n=0}^{\infty} \frac{d_n^{iw}}{2n+1} \left\{ \begin{array}{c} c_n^h(t) \\ c_n^\ell(t) \\ c_n^k(t) \end{array} \right\} \cdot \left\{ \begin{array}{c} 1 \\ \nabla_\theta \\ \nabla_\lambda \\ 1 \end{array} \right\} P_n(\cos\theta)\,, \tag{4.30}$$

with the term d_n^{iw} defined as:

$$d_n^{iw} \equiv \begin{cases} 0 & \text{if} \quad n = 0\,, \\ -d^i \dfrac{P_{n+1}(\alpha) - P_{n-1}(\alpha)}{1+\cos\alpha} & \text{otherwise}\,. \end{cases} \tag{4.31}$$

where here, for the sake of simplicity, we have abbreviated $P_n(\cos\alpha)$ by $P_n(\alpha)$, and d^i is

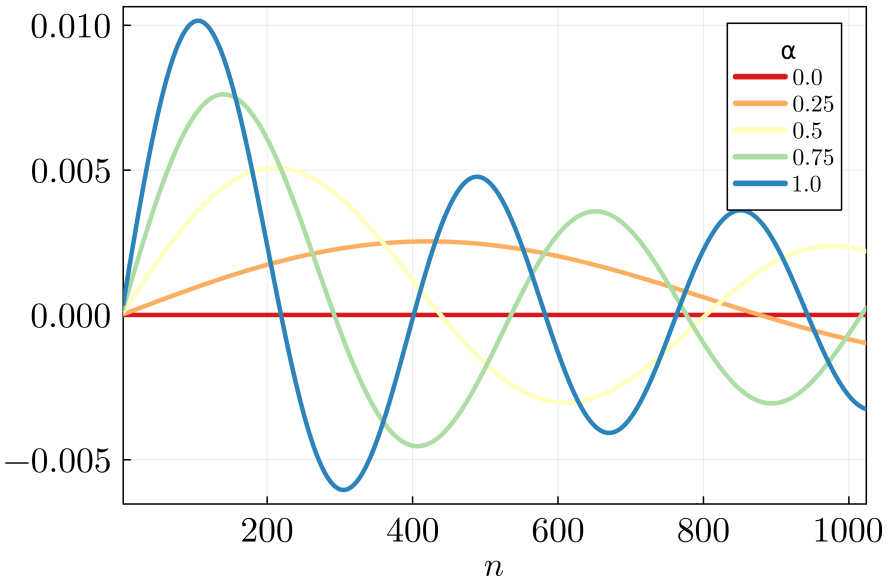

Figure 4.6: **Load coefficient d_n^{iw}** as a function of the harmonic degree n of a disc load of unit height d^i for various half-amplitudes α.

the height of the disc.

In Figure 4.6 the load coefficient d_n^{iw} is shown as a function of n (from 0 to 1024), for different half-amplitudes ($\alpha = 0°, 0.25°, 0.5°, 0.75°, 1.0°$). As we can see, the size of the load determines which harmonic degree (and thus which LNs) will contribute more to the final displacement. For example, the disc load of $\alpha = 0.25°$ will promote mostly the coefficients of the harmonic degrees between 200 and 600, so that the SRF will be mainly sensitive to the LNs at those harmonic degrees.

4.4 Evaluation of the convolutions

To compute the SRF, it is necessary to solve for the time convolutions in Eq. (4.27). To this end, it is extremely useful to consider their transformation in the Laplace domain, where they became mere multiplications between the ice history $\tilde{f}(s)$ and the Laplace-domain LNs. The results, expressed in the time domain and ready-to-use, for a notable

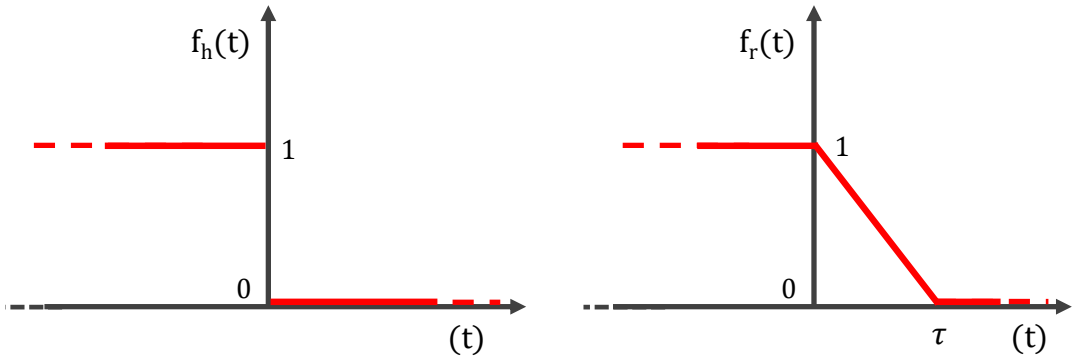

Figure 4.7: Sketch representation of the Heaviside and the ramp unloading ice histories.

number of ice histories are reported in Spada (2003). In the following I expose, for the sake of completeness, only the results of the two cases of interest of this thesis: the Heaviside and the ramp ice histories, represented in Figure 4.7. The following expressions are taken from Spada (2003). These results, together with the expressions of the SRF of the vertical displacement, horizontal displacement and geoid height variation were implemented in my Julia code. Instead, the computation of LNs has been performed through `ALMA`.

Heaviside unloading

The Heaviside unloading ice history describes an instantaneous unloading of the ice mass. For the unloading, we assume that the load was present since $t = -\infty$, and that at $t = 0$ kyr it disappears entirely. This kind of model is the most basic possible, but it can still offer some food for thought. When the information and data about the load evolution are insufficient, or when we can assume that the time-scale of the unloading is much smaller than the characteristic time of response of the Earth's model, this simple ice history is still largely used (this is the case of ER, for instance). In the time domain,

the Heaviside unloading $f_{h\downarrow}(t)$ and its derivative $\dot{f}_{h\downarrow}(t)$ read:

$$\begin{cases} f_{h\downarrow}(t) = 1 - H(t)\,, \\ \dot{f}_{h\downarrow} = 0\,. \end{cases} \tag{4.32}$$

Likewise, one can also define the Heaviside loading ice history $f_{h\uparrow}(t)$:

$$\begin{cases} f_{h\uparrow}(t) = H(t)\,, \\ \dot{f}_{h\uparrow} = 0\,. \end{cases} \tag{4.33}$$

Recalling that each LN can be separated into a elastic x^E and a viscoelastic $x_i^V(t)$ component, and that the fluid limit satisfies:

$$x^F = x^E - \sum_i \frac{x_i^V}{s_i}\,, \tag{4.34}$$

The result of the convolution $c_{h\downarrow}(t)$ and its derivative $c'_{h\downarrow}(t)$ read:

$$\begin{cases} c_{h\downarrow}(t) & = x(t) * f_{h\downarrow}(t) = x^F - H(t)\left(x^F + \sum_i \frac{x_i^V}{s_i} e^{s_i t}\right)\,, \\ \dot{c}_{h\downarrow}(t) & = x(t) * \dot{f}_{h\downarrow}(t) = -H(t) x_i^V e^{s_i t}\,, \end{cases} \tag{4.35}$$

while for $c_{h\uparrow}(t)$ and $\dot{c}_{h\uparrow}(t)$ we have:

$$\begin{cases} c_{h\uparrow}(t) & = x(t) * f_{h\uparrow}(t) = H(t)\left(x^F + \sum_i \frac{x_i^V}{s_i} e^{s_i t}\right)\,, \\ \dot{c}_{h\uparrow}(t) & = x(t) * \dot{f}_{h\uparrow}(t) = H(t) x_i^V e^{s_i t}\,. \end{cases} \tag{4.36}$$

These convolutions allow to compute the SRF presented in the previous section (Eq. 4.30), and their time derivatives.

Ramp unloading

The ramp unloading ice history represents a load that melts at a constant rate. In this case, it is assumed that the load was present at $-\infty \leq t < 0$, and then, in a time period

τ, it decreases at a constant rate. Finally, for $t \geq \tau$, it is absent. Thus, the ice history and its time derivative are:

$$\begin{cases} f_{r\downarrow}(t) = 1 - H(t) + (1 - t/\tau)\left[H(t) - H(t-\tau)\right] , \\ \dot{f}_{r\downarrow}(t) = -(1/\tau)\left[H(t) - H(t-\tau)\right] . \end{cases} \tag{4.37}$$

Instead, in the case of a ramp loading, the ice grows at a constant rate: the load is absent for $-\infty \leq t < 0$, it starts to accumulate at a constant rate for a time τ, and then remains unchanged for $t \geq \tau$. The ice history $f_{r\uparrow}(t)$ and its derivative $f'_{r\uparrow}(t)$ are:

$$\begin{cases} f_{r\uparrow}(t) = 1 - f_{r\downarrow}(t) = H(t) - (1 - t/\tau)\left[H(t) - H(t-\tau)\right] , \\ \dot{f}_{r\uparrow}(t) = (1/\tau)\left[H(t) - H(t-\tau)\right] . \end{cases} \tag{4.38}$$

The convolutions of the previous ice history with the LNs yield:

$$\begin{aligned} c_{r\downarrow}(t) =& h^F - \\ & H(t)\left[x^E \frac{t}{\tau} - \sum_i \frac{x_i^V}{s_i}\left(\frac{t}{\tau} + \frac{1 - e^{s_i t}}{s_i \tau}\right)\right] \\ & + H(t-\tau)\left[x^F\left(\frac{t}{\tau} - 1\right) - \sum_i \frac{x_i^V}{s_i}\frac{1 - e^{s_i(t-\tau)}}{s_i \tau}\right] \\ \dot{c}_{r\downarrow}(t) =& - H(t)\left[\frac{x^E}{\tau} - \sum_i \frac{x_i^V}{s_i}\left(\frac{1}{\tau} - \frac{e^{s_i t}}{\tau}\right)\right] \\ & + H(t-\tau)\left[\frac{x^F}{\tau} + \sum_i \frac{x_i^V}{s_i}\frac{e^{x_i^V(t-\tau)}}{\tau}\right] \end{aligned} \tag{4.39}$$

and

$$
\begin{aligned}
c_{r\uparrow}(t) = & \\
& H(t)\left[x^E\frac{t}{\tau}-\sum_i\frac{x_i^V}{s_i}\left(\frac{t}{\tau}+\frac{1-e^{s_it}}{s_i\tau}\right)\right] \\
& -H(t-\tau)\left[x^F\left(\frac{t}{\tau}-1\right)-\sum_i\frac{x_i^V}{s_i}\frac{1-e^{s_i(t-\tau)}}{s_i\tau}\right], \qquad (4.40)\\
\dot{c}_{r\uparrow}(t) = & H(t)\left[\frac{x^E}{\tau}-\sum_i\frac{x_i^V}{s_i}\left(\frac{1}{\tau}-\frac{e^{s_it}}{\tau}\right)\right] \\
& -H(t-\tau)\left[\frac{x^F}{\tau}+\sum_i\frac{x_i^V}{s_i}\frac{e^{x_i^V(t-\tau)}}{\tau}\right].
\end{aligned}
$$

Chapter 5

Results and Discussion

In this chapter I present and discuss the main outcomes of my work. While other original results regarding rheology and LNs were already shown in the previous chapters, here I focus the attention on the findings of the experiments I ran concerning surface unloading. The goal of this section, and the aim of Thesis in general, is to obtain a list of "guidelines" useful for the recognition of the optimal conditions for the observation of a transient regime in unloading phenomena. This list could be considered by geodesists and geophysicists as a sort of "zero-order reference" for setting up a campaign which aims to detect transient effects caused by natural or anthropogenic unloading. Thus, even if the focus of the Thesis is the response to ice unloading in Greenland, the conclusions of this chapter can be extended to any other case studies.

Here I examine how different parameters like depth, thickness, viscosity, distance from the load, size of the load, or the ice history of the load can enhance (or even hide) transient responses. From these results, I try to sum up which of the aforementioned variables plays a major role, and which not. Given the high number of variables, I have intentionally kept the Earth's models as simple as possible. Indeed, the introduction of many Earth's layers, and thus the increase of the number of model parameters, makes the interpretation of the results more complicated.

The results discussed in this chapter have been obtained through a Julia code that mimics the TABOO "task 2" functionality: the code relies upon ALMA for the computation of an approximate form of multi-exponential Love numbers, and then uses the formulas obtained in Section 4.3 to compute the SRF of the displacements and the geoid height variation, as well as their time derivatives. To check the validity of my code, I ran a comparison test with TABOO (Spada et al., 2011), whose results are presented in Section 5.1. The need of a new code was due to the fact that TABOO *does not include*, in its native version, transient rheological models. Still, the code I developed has some drawbacks *w.r.t.* TABOO, like the fact that it includes just two type of ice histories (Heaviside and Ramp), while TABOO implements a total of eight different ice histories. However, for the aims of this Thesis, this was sufficient to run comprehensive experiments.

The case studies examined are sorted by increasing complexity, but they all refer to compensated disc-loads. The first experiments concern the case of the instantaneous unloading of a disc-like glacier: a large ice mass is removed at t_0, assuming a pre-existing condition of equilibrium. This scenario, which could appear extremely simplicistic, is instead largely used by the scientific community: in GIA studies, to implement ER (Elastic Rebound) corrections to GNSS records, the ice model representing present-day ice melting is discretized on a set of disc load with an associate amplitude α and mass loss Δm (Spada et al., 2012). Scoping pro and cons of this approach is instead notably useful to understand the limit of ER modeling. Then, always considering a disc load, I have investigated the effects of a "ramp" unloading, *i.e.,* a constant rate unloading, that is particularly suited to describe present day ice loss. Indeed, many glaciers and ice sheets around the globe are experiencing negative trends over the years. Usually, those trends are well described by a ramp with a negative slope, or even by a sequence of ramps. This evolution is a bit more realistic that the Heaviside one, and we shall see that it should be recommended when the time period of the unloading becomes significant ($> 10yr$).

Radius (10^6 m)	Density (kg/m^3)	Rigidity (10^{11} Pa)	Viscosity ($Pa \cdot s$)	Rheology
6.371	2689	0.282	-	Elastic
6.281	4430	0.837	10^{21}	Maxwell
5.701	4919	2.17	10^{22}	Maxwell
3.480	10927	-	-	Fluid

Table 5.1: Description of the model used to compare my code with `TABOO`. The model, described at page 113 of the "Taboo User Guide" (Spada et al., 2003), was originally designed by Yuen et al. (1982).

Finally, a more realistic case study is presented: the aim of the last experiment is modeling the Earth's response in the neighborhood of Helheim Glacier, a peripheral glacier in South-east Greenland. For this experiment I used a fine grid of $\sim 47,000$ points representing the evolution of the Glacier from year 2007 to 2022, courtesy of Dr. V.R. Barletta and Dr. C. Gong. Each grid point, which is associated to an area and a height loss rate, has been converted into an equivalent disc, and then the contribution of each disc is computed in two points, representing the location of two GNSS stations, HEL2 and KULU.

5.1 Numerical benchmark

This section presents the results of the benchmark test done by comparing the output of my code with those of `TABOO` (Spada et al., 2004). The tests include two toy-scenarios describing the time evolution of the vertical displacement and the vertical velocity following two different types of ice history, respectively an instantaneous unloading and a ramp unloading. These two kinds of ice histories, depicted in Figure 4.7, are the simplest possible: they describe an ice mass that instantaneously disappears at a given time $t_0 = 0$ yr, and a mass that is kept constant from $-\infty < t < 0$, then decreases linearly

between $0 < t < \tau$, and then is absent for $t > \tau$, with $\tau = 3\ kyr$. The Earth's model used for this computation is reported in Table 5.1, and it has been chosen among those available in `TABOO` (it was originally introduced by Yuen et al. (1982)). In both cases, the ice load is a compensated disc, with an angular half amplitude of 1°, whose total ice height loss is 100 m, and the computations refer to a time window of 20 kyr. These tests are fundamental to check the validity of the results that will follow.

The outcomes of this test are reported in the following, in Figures 5.1, 5.2, 5.3 and 5.4. Each of them shows, on the left, the results of the computations performed by my Julia code (red, dashed curves) and `TABOO` (green solid curve) and, on the right, the relative differences $(\texttt{output}_{TABOO} - \texttt{output}_{Julia})/\texttt{output}_{TABOO}$. From the latter, we can see that the relative differences are always below $\sim 5\%$. We can also notice, by comparing the four panels of each figure, representing the output observed at various observation distances, that they are more relevant underneath and in the proximity of the load, and they decrease with increasing distance. Nevertheless, it is undeniable that the relative differences increase with time. However, this does not represent a problem for the aims of this Thesis, since the typical time scale of the experiments that I present reaches a range of 100 yr utmost. In this time range the relative differences are even lower than the aforementioned $\sim 5\%$: this is clearly shown in Figure 5.3 and 5.4, panel (b) (that zooms panel (a) on the time period $(0, 1000)$ yr of the ramp unloading experiment).

5.2 Heaviside unloading experiments

This section is dedicated to the presentation and discussion of the tests ran using a compensated disc load described by a Heaviside unloading ice history (see Figure 4.7, (left)). In the following I discuss the role of the rheological law and viscosity of the SUM, the lithospheric thickness and the size of the load.

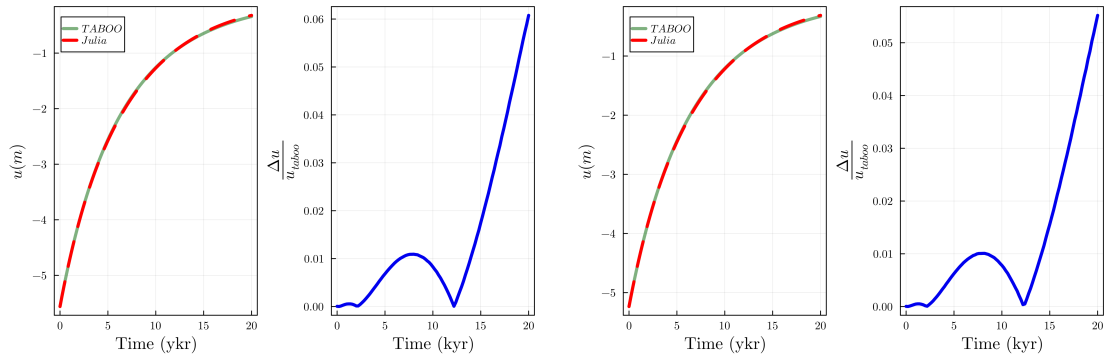

(a) *Observation distance:* 0.1°

(b) *Observation distance:* 0.5°

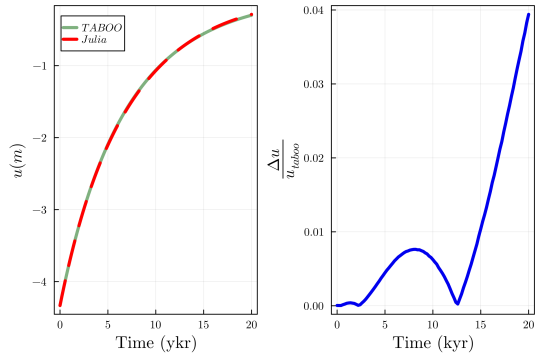

(c) *Observation distance:* 1°

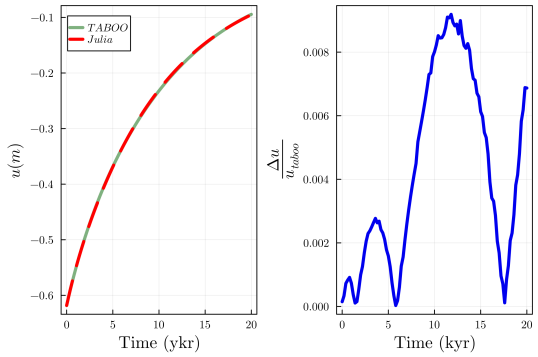

(d) *Observation distance:* 3°

Figure 5.1: **Displacement - Heaviside unloading case**. Each box shows, on the left, the time evolution (from 0 to 20 *kyr*) of vertical displacement and on the right (in blue) the relative difference between `TABOO` and my computations, based upon an ad-hoc Julia code, at different distances from the centre of the disc load (0.1°, 0.5°, 1° and 3°). For this experiment, I used a disc load of height 100 m, half-amplitude of 1° and the Earth model described in Table 5.1. The relative differences tend to decrease with increasing distance. They remain under the threshold of 1.2% in the first 10 *kyr*, while from 12.5 *kyr* they increase up to 6%. However, for the purpose of this work, which focuses on the Earth's response on centennial time scales, I have verified that the relative differences are of $\sim 0.1\%$.

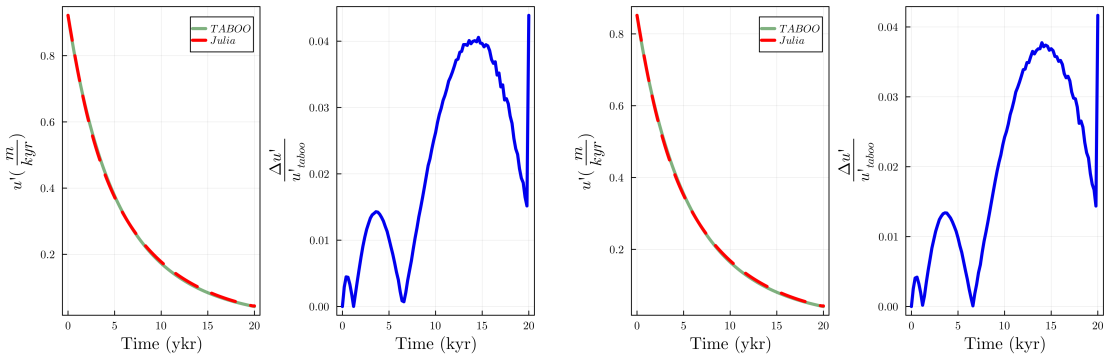

(a) *Observation distance:* 0.1°

(b) *Observation distance:* 0.5°

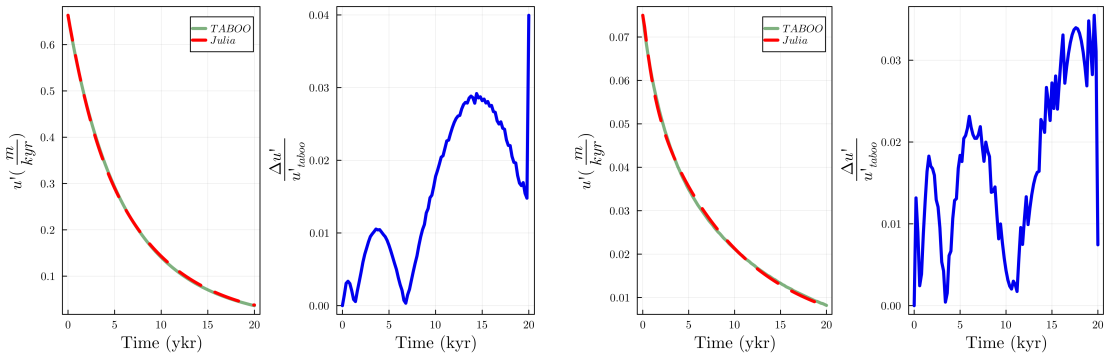

(c) *Observation distance:* 1°

(d) *Observation distance:* 3°

Figure 5.2: **Displacement rates - Heaviside unloading case**. Same as Figure 5.1, but for the displacement rate.

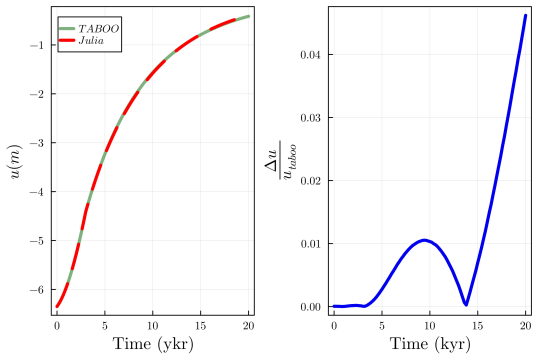

(a) *Observation distance:* 0.1°

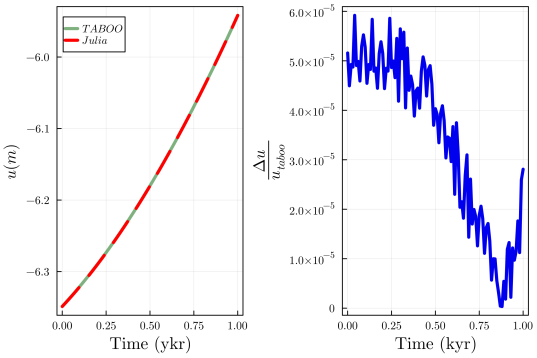

(b) *Zoom of Figure (a)*

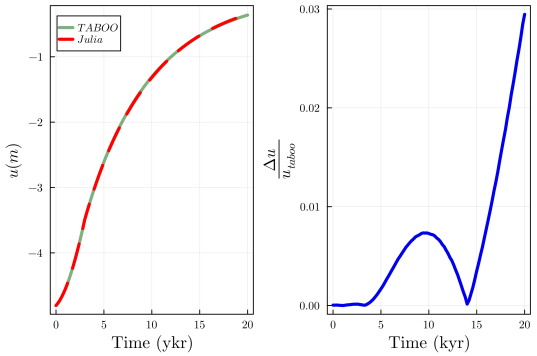

(c) *Observation distance:* 1°

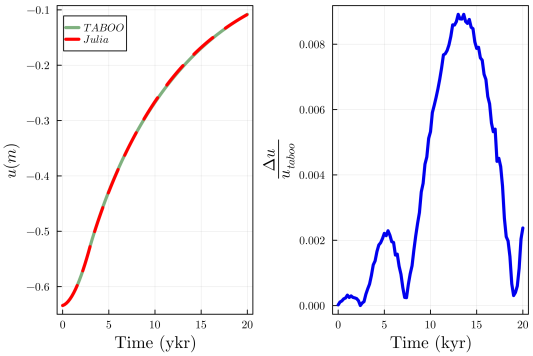

(d) *Observation distance:* 3°

Figure 5.3: **Displacement - Ramp unloading case**. Each box shows the time evolution, in the time range between 0 to 20 *kyr*, of the vertical displacement (left, green and red) and the relative differences between my computations ("Julia") and TABOO's output (right, in blue), at various distances from the centre of the disc load (0.1° in the first raw and 1° and 3° in the other). For this experiment I used a disc load of semi-amplitude 1°, and the Earth's model of Table 5.1. During the melting phase, between 0 and 3 *kyr* the load decreases at a constant rate from a height of 100 *m* to 0 *m*. As shown in (b), in this phase the relative differences are significantly low ($< 0.1\%$). These results show that the relative differences remain globally below the 1.2% level in the first 10 *kyr*.

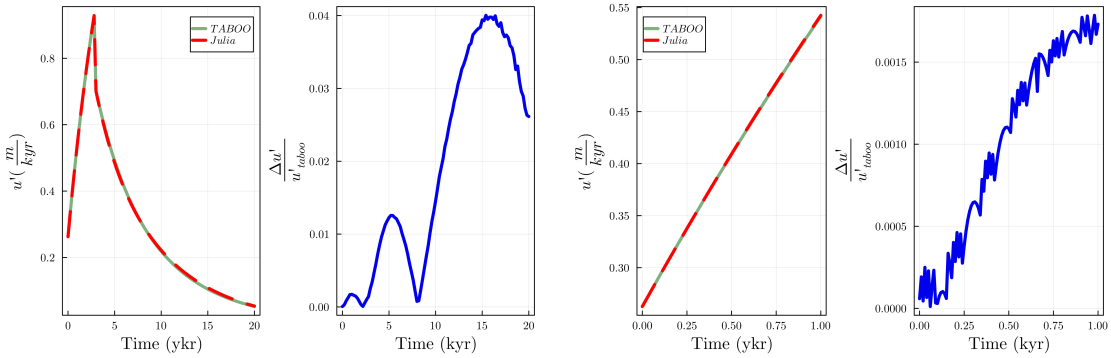

(a) *Observation distance:* 0.1° (b) *Zoom of Figure (a)*

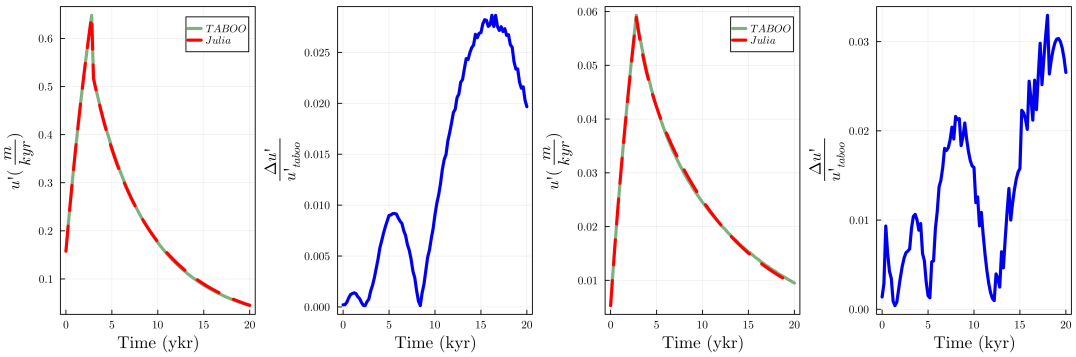

(c) *Observation distance:* 1° (d) *Observation distance:* 3°

Figure 5.4: **Displacement rates - Ramp unloading case**. Same as Figure 5.3, but for the displacement rate. From panel (b) we can see that in the first 1 *kyr*, during the melting phase, the relative differences are significantly low, $< 0.15\%$.

5.2.1 Role of rheology and viscosity

This experiment is the first of a group of three performed with an instantaneous unloading ice history. The aim is understanding the role of rheology and viscosity in the determination of the displacement and velocity profile. I consider two cases:

- **case (a)**: Load half-amplitude α of 1°. In scale, it could represent a toy-model of a portion of an ice-sheet ($\alpha = 1° \simeq 100\ km$).
- **case (b)**: Load half-amplitude of 0.3°, representing a medium size glacier ($\alpha = 0.3° \simeq 30\ km$).

I remind here that, as we have saw in Figure 4.6, the size of the load acts as a "filter" in the SRF, promoting the contribution of certain harmonic degrees at the expense of some others.

The results of this test are shown in Figures 5.6, 5.5, and 5.7. In Figures 5.6 and 5.5 the time evolution of the displacement rate is displayed from two different observation points located at the centre of the load ($\theta_o = 0°$, left) and at an angular distance of $\theta_o = 1°$ (right). The two figures show the response caused by a disc-shaped load of half amplitude $\alpha = 1°$ and $\alpha = 0.3°$ respectively, that instantaneously disappears at $t = 0\ yr$. Instead, Figure 5.7 represents the displacement rates as a function of the angular distance from the centre of the load at the observation time $t = 0\ yr$. The Earth's models considered in this experiment include the three rheological configurations reported in Section 4.1 and consider three different values for the SUM viscosity η_{SUM}, namely $5.0 \cdot 10^{18} Pa \cdot s$, $5.0 \cdot 10^{19} Pa \cdot s$ and $1.0 \cdot 10^{20} Pa \cdot s$. As expected, the models including the lowest values of η_{SUM} (light colors) are those which produce the highest velocities.

The first conclusion that we can draw is that transient models allow to retrieve, without changing the viscosity profile, higher displacement rates. This fact is consistent with the findings of Boughanemi and Mémin (2024). The presence of a transient assures an earlier departure from the elastic regime, as we have observed in the figures concerning

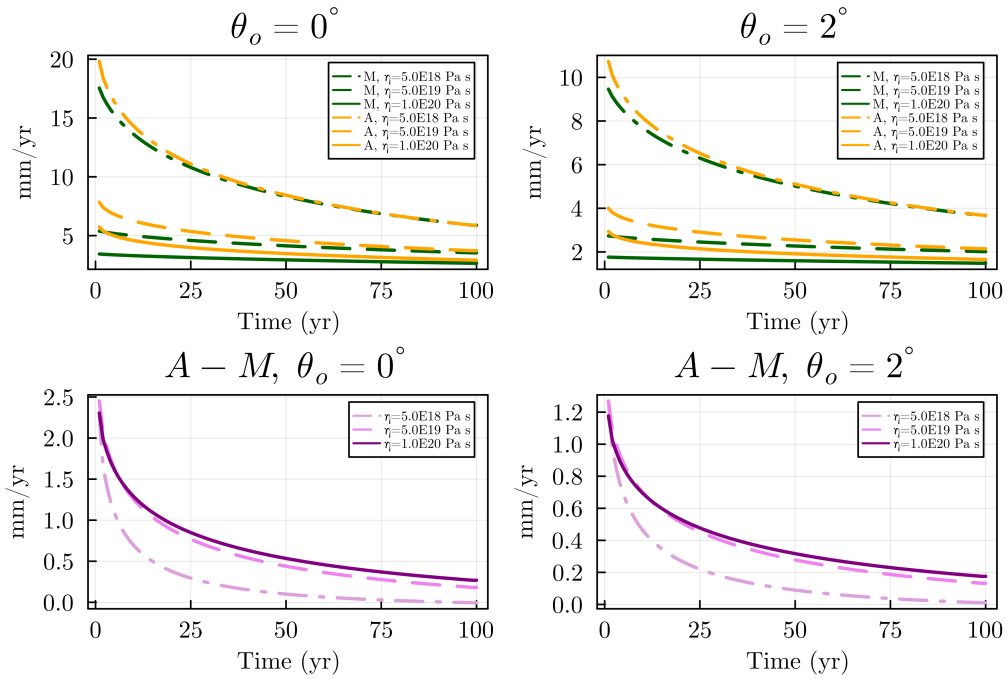

Figure 5.5: (TOP) **Vertical displacement rates**, as a function of time for various Earth models observed at $\theta = 0^\circ$ and $\theta_o = 2^\circ$, for a disc load of half-amplitude $\alpha = 1^\circ$. (BOTTOM) **Difference between pairs of equivalent "Maxwell" and "Andrade" models**, always as a function of time. From this latter we can see that the configurations which include the layers with the highest viscosity values ($\eta_{SUM} = 5.0 \cdot 10^{19} Pa \cdot s$ and ($\eta_{SUM} = 1.0 \cdot 10^{20} Pa \cdot s$) are those which remain distinguishable for longer times.

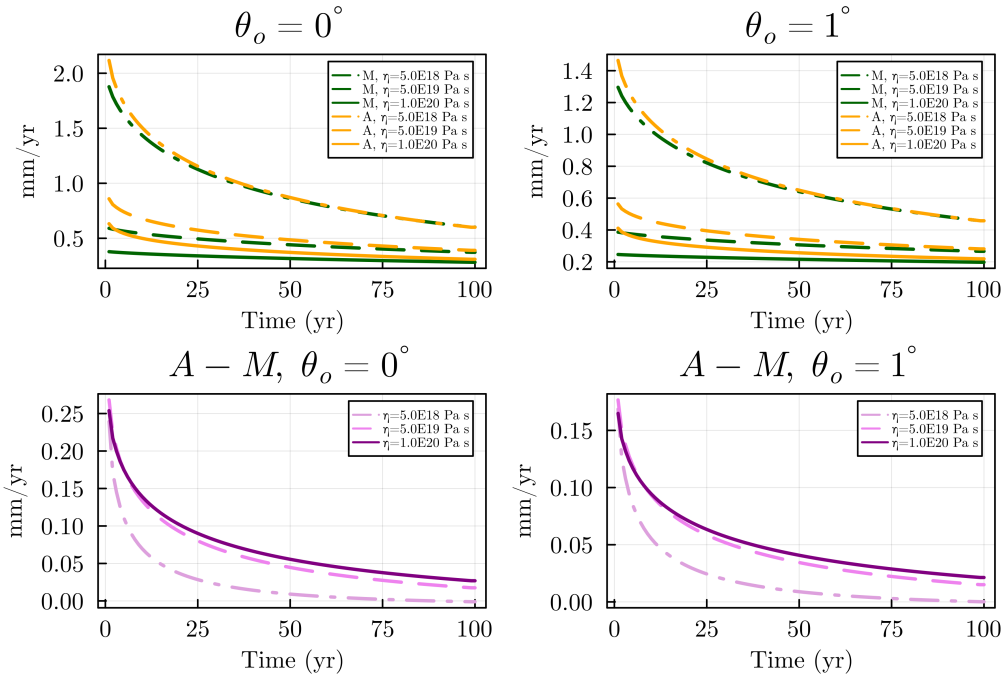

Figure 5.6: (TOP) **Vertical displacement rates** plotted as in Figure 5.6 but for a disc load of half-amplitude $\alpha = 0.3^\circ$ and a Heaviside ice history. (BOTTOM) **Difference between pairs of equivalent "Maxwell" and "Andrade" models**, always as a function of time.

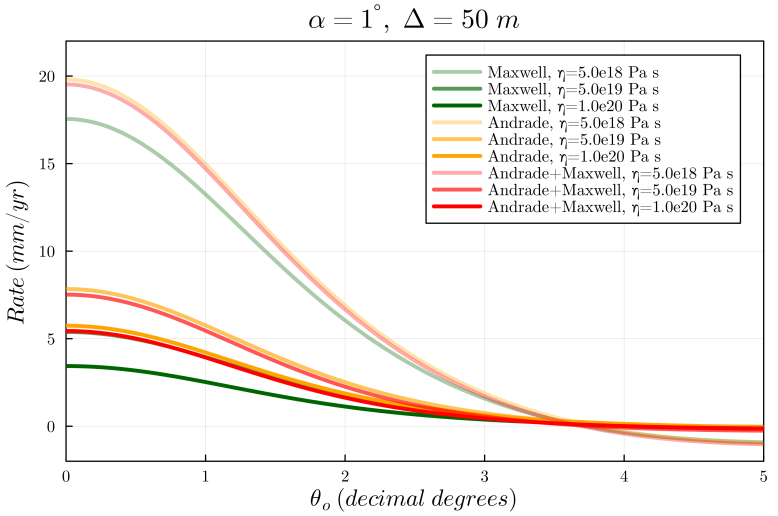

(a)

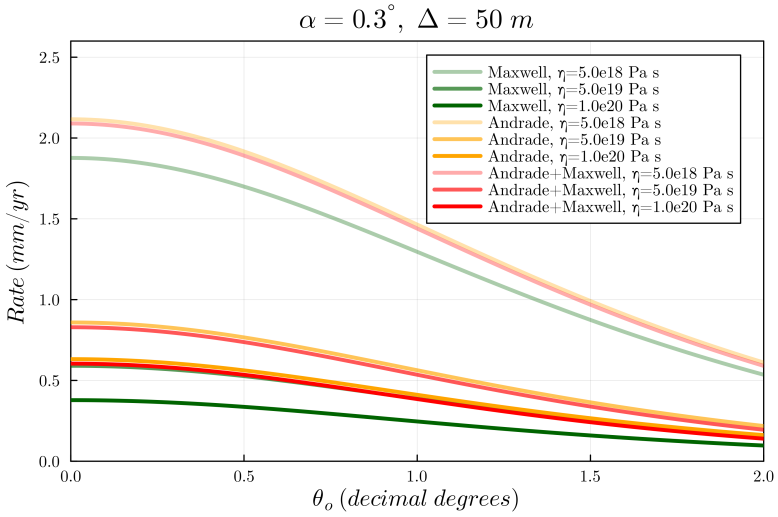

(b)

Figure 5.7: **Displacement rate profiles.** Panels (a) and (b) display the response (as a function of the angular distance from the centre of the load θ_o) to a Heaviside disc load of initial height $h = 50\ m$ and half-amplitude 1° and 0.3° respectively. The green curves refer to Maxwell models, the orange to Andrade ones, and the red to the Andrade + Maxwell ones. Different intensities in the colors reflect different SUM viscosities.

LNs in the previous chapter (Figure 4.2). This fact is largely known in geodynamics but also in planetary science. For instance, Tobie et al. (2019) argues that using a Maxwell rheology for modeling the tidal response of the Moon led to an underestimation of the viscosity. This is because, at higher frequencies, far from those associated to the τ_M of the model, Maxwell rheology underestimates the viscous dissipation. This is true for tidal loading, but, translated in the framework of surface loading, this means that the Maxwell system is less prone to start flowing on too short time scales. However, we must retain that in many cases in geophysics, the viscosity is the main unknown, and its assessment is the final goal of many GIA studies. Thus, one of the primary strategies to fit anomalous rates is invoking the presence of low viscosity zones (see, *e.g.*, Barletta et al., 2018), instead of supposing the presence of a more complex rheological behavior. It is clear that both approaches can be correct as far as no other constraint on the viscosity value is available.

From Figures 5.6 and 5.5 (bottom) it is interesting to notice that the models that produces the most significant differences between the "Maxwell" and "Andrade" configurations output are those with higher viscosities in the SUM. Also, as the time increases, we see that the models with $\eta_{SUM} = 5.0 \cdot 10^{18} Pa \cdot s$ tend to merge more quickly, while the other maintain a higher discrepancy for a longer time.

Then, by comparing the two panels of Figure 5.7, we can see that the differences between the pure "Andrade" model (orange) and the mixed "Andrade+Maxwell" model (red) are negligible, suggesting that the displacements are not very sensitive to the rheology of the layers below the SUM (for this very reason, the "Andrade+Maxwell model was lacking in the previous Figures 5.6 and 5.5, since it made quite problematic the interpretation of the plot). Instead, the magnitude of the "Maxwell" model is substantially lower, at least below and in the proximity of the load. Another clear difference is the rate at which the values decrease with distance from the center of the load. In both cases, at a distance of 1.5°, the magnitude of the rates has been reduced by half

with respect to the value at $\theta_0 = 0°$, meaning that in panel a), the rate has decreased by $-6.67(mm/yr)$ *per* degree, while in panel b) it is $-0.67(mmy/yr)$ *per* degree. However, as we will see in Section 5.2.2, this fact is ultimately due to the thickness of the elastic lithosphere *w.r.t.* the size of the load.

5.2.2 Role of the elastic lithosphere thickness

Figure 5.8 displays the vertical displacement rate as a function of the angular distance from the centre of the load. Each color refers to a different model: "Maxwell" (blue), "Andrade" (red), "Andrade + Maxwell" (purple), while the four shades refer to different thicknesses of the lithospheric layer. For this plot, the viscosity of the SUM was set to $5.0 \cdot 10^{19} Pa \cdot s$. As anticipated before, the thickness of the lithosphere influences the way in which the rate decreases with the distance from the load. From the physical point of view, thin lithospheres can produce higher rates in the proximity of the load, because the influence of the underlying SUM is more relevant, being closer to the surface. From a formal perspective, this is due to the way in which the load deformation coefficients and the LNs mix together. In this case, I have kept fixed the load size, while the LNs varied since the lithospheric thickness changed. As we saw in Figure 4.4, thicker lithospheres produce "more elastic" LNs, meaning that the effects of the lithosphere were more significant. If we instead keep the same model and increase the dimension of the load, we see (always with the aid of Figure 4.6) that the load coefficients tend to magnify the role of the lower degree terms, *i.e.,* the LNs that influence the most the analysis become the low degree ones, those that can sense the large-scale structure of the Earth most. To sum up this paragraph, we could say that the larger the load extension, the more it will be sensitive to the deeper structure of the Earth's model.

To better visualize this result, I made the second panel of Figure 5.8, reporting the very same results but with each curve normalised by its maximum value (that corresponds to the value at $\theta_o = 0°$). Here it is clear that the profiles corresponding to the models

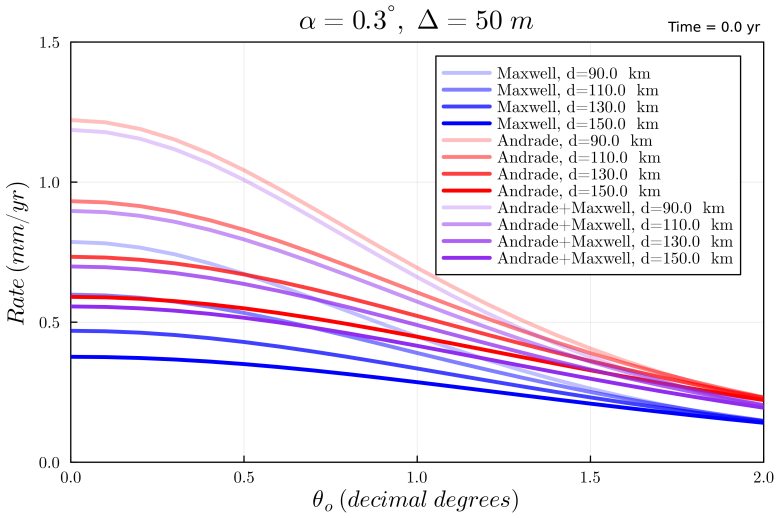

(a)

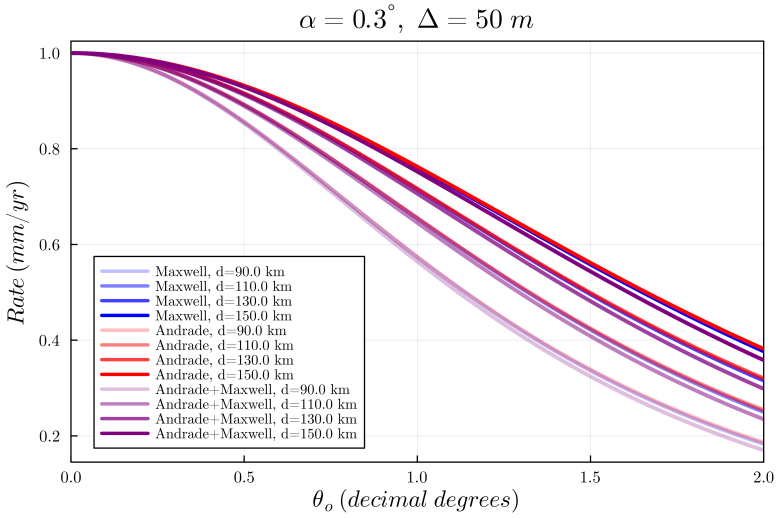

(b)

Figure 5.8: a) **Displacement rate profile** of the three rheological configurations for different values of the Lithospheric thickness $d_l = 90, 110, 130, 150\ km$; below, panel b) shows the same trend but normalized *w.r.t.* the maximum of each profile.

with thinner lithospheres are those which decay more rapidly with the distance from the centre of the load. Again, we can conclude that in this case the lithosphere works as a low-pass filter: the thicker it is, the more the high frequencies of the SRF are cut out.

5.2.3 Role of the disc-load size and mass

The size of the load is an important parameter in surface load problems: as a rule of thumb, it is generally assumed that the Earth's response is mostly driven by those layers that stay at depths comparable with the spatial extent of the disc load.

To test and verify this statement, I plotted the displacement rate as a function of the half-amplitude of the disc load (*i.e.*, the load size) for different observation points. These plots and all the other presented from now on until the end of this section, report the rates observed at time $t = 0\ yr$, the instant right after the disappearance of the ice load. The first set of results are shown in Figures 5.9 and 5.10, which report the comparison between "Andrade", "Maxwell", and "Andrade" and "Andrade+ Maxwell" respectively. The conclusions we can learn from these plots are twofold: first, the displacement rate produced by the different rheological configurations are significantly different mainly below and in the proximity of the disc load, that is when $\alpha > \theta_o$; second, that once we fixed the Earth model and the observation point, there exists a load size (and mass) that maximizes the displacement rate. For example, consider panel (a) of Figure 5.9, which displays the case of an observer placed (hypothetically) at the centre of the ice load, thus below the ice. The size of the load that maximizes the displacement rate (for this set of Earth models) in that observation point is around 3° and 4°: this means that if we enlarge the size of the load over 4°, we would not observe higher rates.

To better address this point, Figure 5.11 shows the displacement rates as a function of the load half-amplitude and observation point. In the figures we can clearly identify the presence of the maximum located between 3° and 4°, for $\theta_o = 0°$. Notice that when the load half-amplitude α is smaller than θ_o (*i.e.*, the observer is outside from the load), the

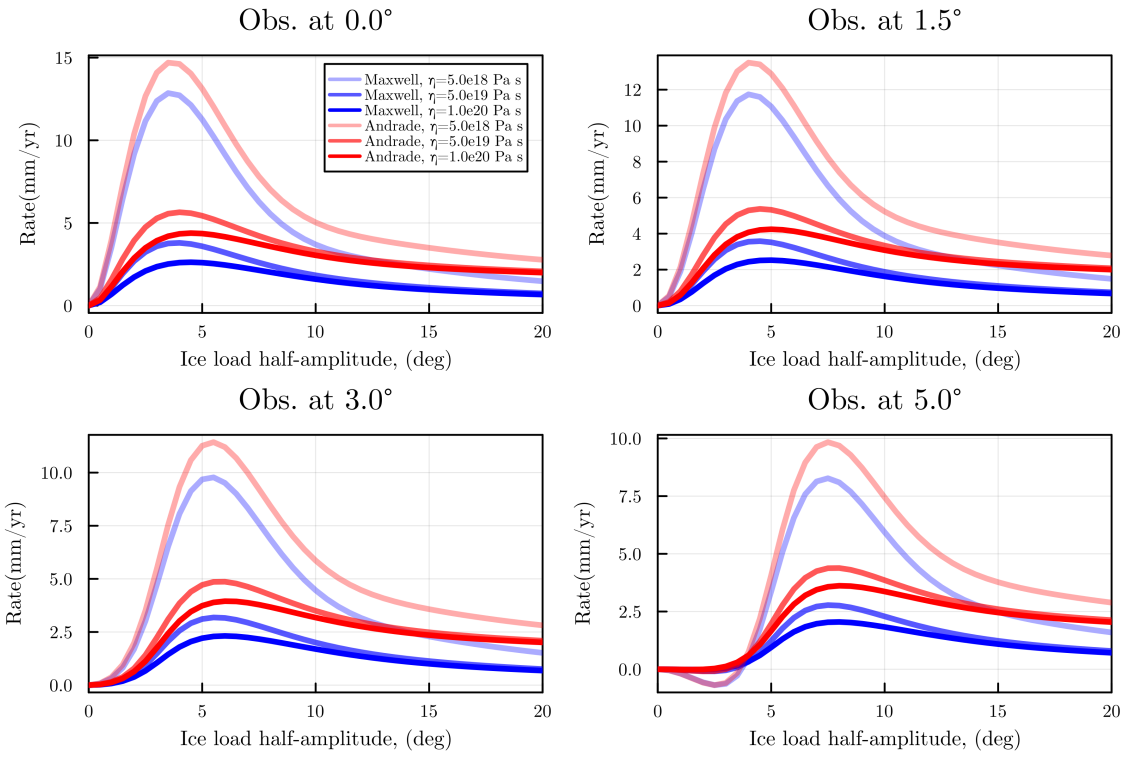

Figure 5.9: **Displacement rates as a function of the angular distance from the centre of the load.** Comparison between the Maxwell (blue) and Andrade (red) models. The different intensities of colors refer to various viscosities of the SUM ($5 \cdot 10^{18} Pa \cdot s$, $5 \cdot 10^{19} Pa \cdot s$, $1 \cdot 10^{20} Pa \cdot s$). One can notice the presence of a maximum whose location changes depending on the observation point. Also, it appears clear that the differences between the pairs of rheologies are enhanced when $\alpha > \theta_o$, *i.e.,* when the observation point is inside the area of the load.

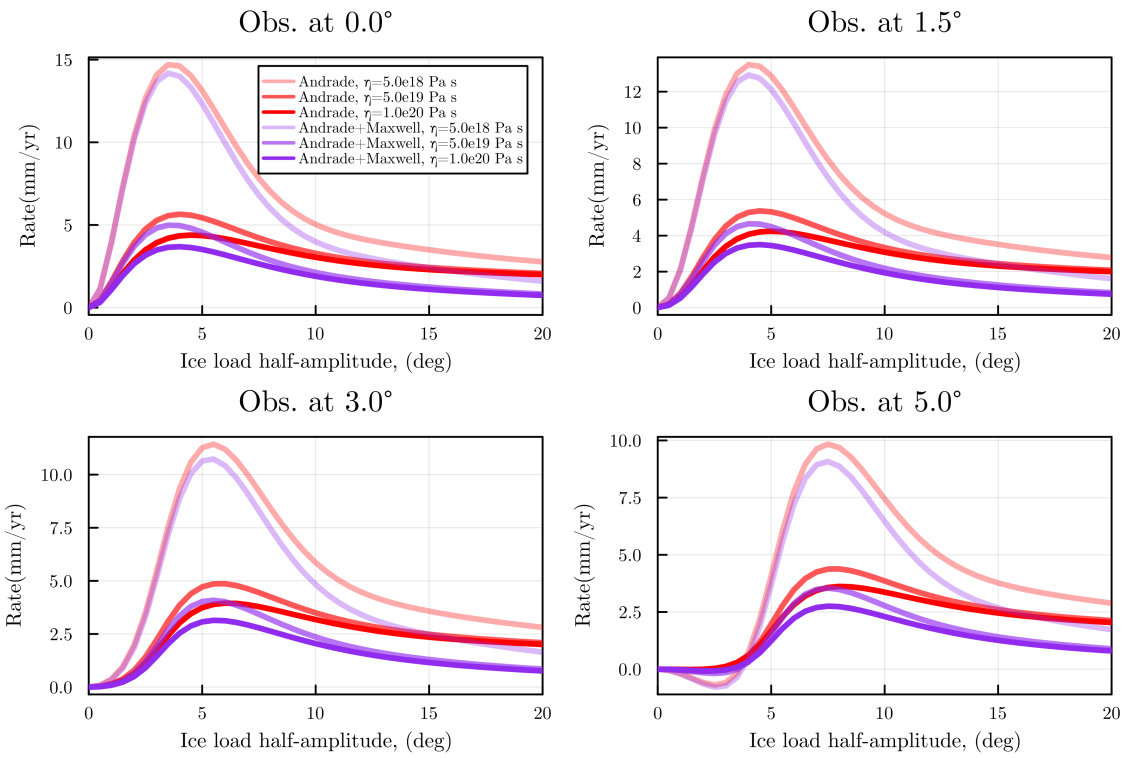

Figure 5.10: **Displacement rates as a function of the angular distance from the centre of the load.** Same as Figure 5.9, but here the comparison is between the "Andrade + Maxwell" (purple) and "Andrade" (red) models.

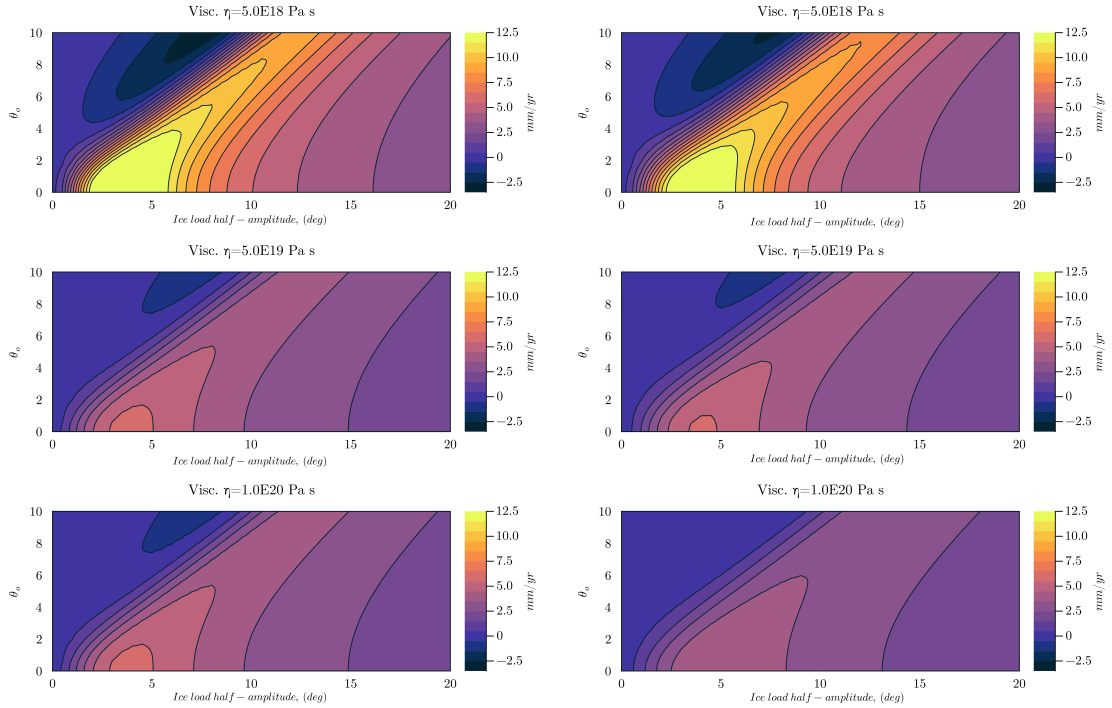

(a) *Litho. thick.*$= 90km$ (b) *Litho. thick.*$= 150km$

Figure 5.11: **Displacement rate as a function of the ice load size and observation distance** θ_o, for different lithospheric thicknesses (columns) and viscosities of the SUM (rows). Here I considered the "Andrade" configuration. The pattern is the same in all the six panels, confirming that for $\alpha < \theta_o$ the rates are lower. Small values of viscosity and lithospheric thickness enhance the magnitudes of the maxima. It is interesting to notice that, for very large loads, the rates are extremely similar, independently from the setting of the lithosphere and the SUM. This reflects the fact that such large loads would be primarily influenced by the deepest layers of the Earth, which in these experiments are identical in every model.

rates are minimal. Also, the figure investigates the effects of the lithospheric thickness, since on the right, we have the output to a model with $d_l = 90\ km$, and on the left, a similar model, but with a lithospheric thickness $d_l = 150\ km$. The difference between the two figures are subtle, but with a little effort one can see that, in case of a thicker lithosphere, the maximum rates are attained for a narrower range of load half-amplitude. Once again, this is due to the low-pass filter effect of the lithosphere.

Figure 5.12 was made along the same line of the previous one, but here, for the same lithospheric thickness ($d_l = 110\ km$) and SUM viscosity ($5.0 \cdot 10^{18} Pa \cdot s$), since the comparison is between the three rheological configurations ("Maxwell", "Andrade", "Andrade + Maxwell"). While "Andrade" and "Andrade + Maxwell" produce almost undistinguishable results, we can instead notice some difference with the "Maxwell" one. It seems that the use of Maxwell rheology has an effect similar to those observed when the lithosphere thickness is increased: smaller rates at the margins around $\alpha \sim \theta_o$ and the maxima occupy a reduced portion of the plot.

Finally, in Figure 5.13 I plot the *differences* between the expected rates of equivalent models having different rheologies in the SUM: "Andrade" - "Andrade + Maxwell" and "Andrade" - "Maxwell" respectively. The idea behind these plots is highlighting where, for a given disc size, the two models show their most significant differences. As regard the first columns of plots, showing the result of "Andrade" - "Andrade + Maxwell" for various values of the SUM viscosity, we notice that differences tend to diminish with increasing observation distance θ_o, but they increase with larger disc load size. The other column on the right shows the result for "Andrade" - " Maxwell". Here the biggest differences are located around the area of the maximum rates.

To end this section, I summarize the main results I have obtained:

- The main difference between "Andrade" and "Maxwell" configurations in the displacement rate occur in the early stages of the experiment, right after the disap-

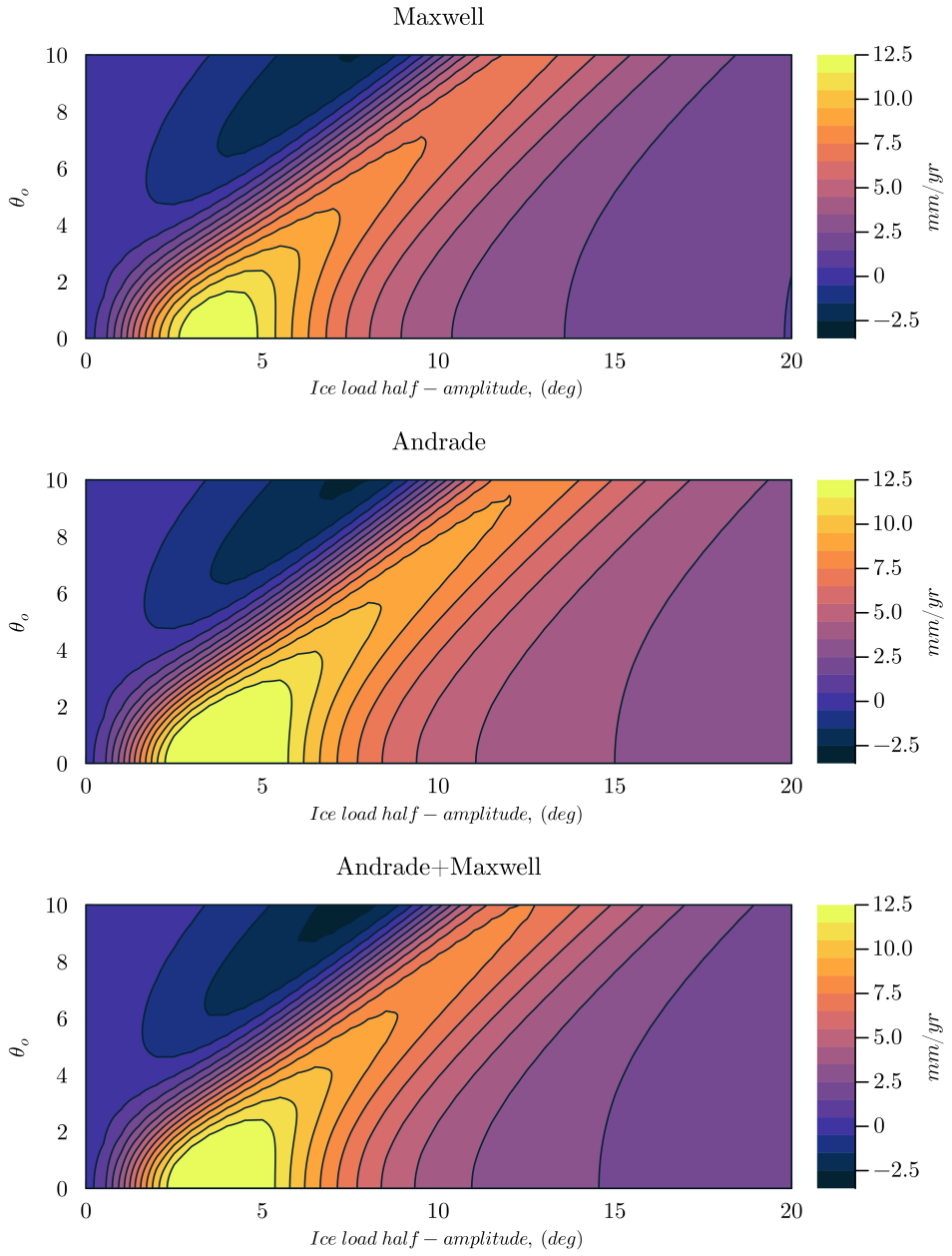

Figure 5.12: **Displacement rate as a function of the ice load size and observation distance** θ_o, for different rheologies of the SUM. Here we see clearly a feature that could be appreciated also in Figures 5.9: with equal settings of the models, Andrade's maxima fill a larger area than the Maxwell one, suggesting, once again, a greater predisposition to the bending.

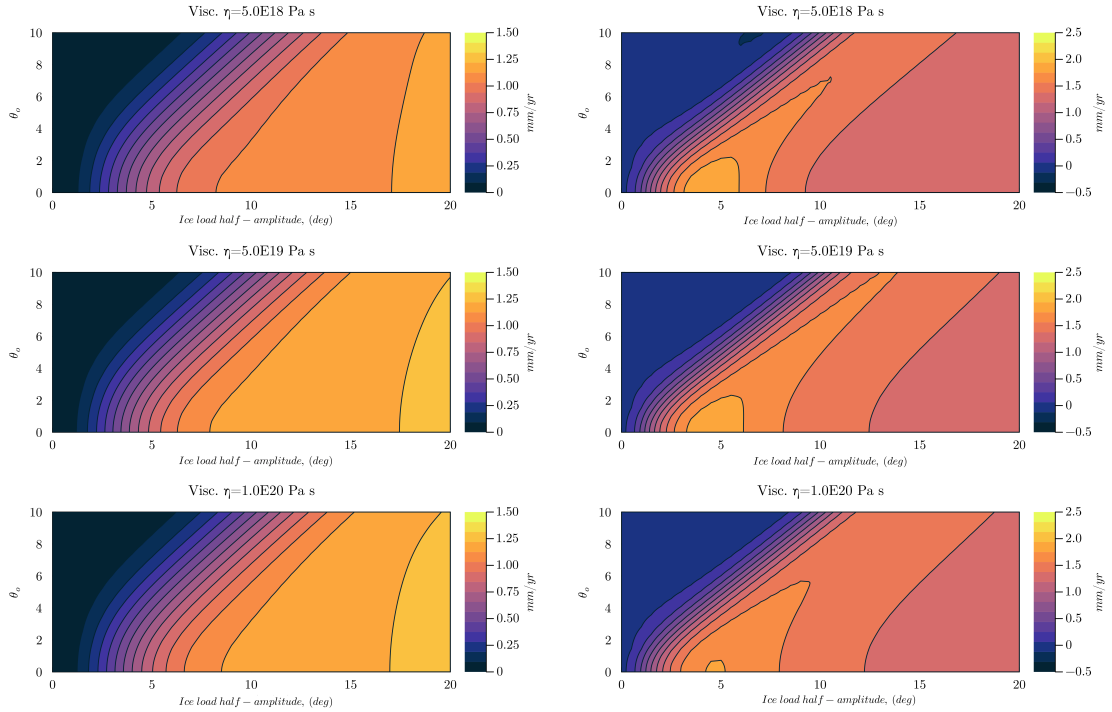

(a) *Andrade-(Andrade+Maxwell)* (b) *Andrade-Maxwell*

Figure 5.13: **Differences between two rheological settings**. This figure shows the differences between pairs of equivalent models, having different rheologies in the SUM. Each row displays the result for models having the viscosity of the SUM set on $5.0 \cdot 10^{18} Pa \cdot s$, $5.0 \cdot 10^{19} Pa \cdot s$, $1.0 \cdot 10^{20} Pa \cdot s$.

pearance of the ice load. With increasing time, these differences tend to vanish. I thus conclude that, with equal elastic and viscoelastic model parameters, the magnitudes of the accelerations differ, and that those produced by the "Andrade" configuration are greater than those expected from the Maxwell one.

- Since the early stages of deformation, the size of the load controls which Earth layers will contribute more to the determination of the output rates. Loads of small dimension will be mainly affected by the flexure of the lithosphere, while those of larger size will sense also the deeper viscoelastic layers.

- The lithosphere acts like a low-pass filter: the thicker it is, the more the signal flattens and spreads out.

- Viscosity and rheological law have similar effects, increasing or decreasing the expected rates.

- Observation points *below* the load are those in which it is possible to appreciate the greater differences among the model predictions. As we move away from the border of the load, these discrepancies tend to diminish.

5.3 Ramp unloading experiments

The second set of experiments considers a compensated disc load with a ramp ice-history: for $-\infty \leq t \leq 0$, the ice load is kept constant and its height is h, then, from $0 \leq t < \tau$, it is turned off at a constant rate and finally, for $t \geq \tau$, where $\tau > 0$, the load is absent (see Figure 4.7, right). This type of ice history is certainly more "realistic" than the Heaviside one. In general, glaciers and ice sheets experience periods of accumulation and ablation of various time scales. The shortest one is the seasonal signal, characterized by a phase of mass accretion, during the winter season, followed by a phase of mass loss, in summer. If we enlarge the observation time over the years, we would notice

that the seasonal variation is superimposed to another signal with a lower frequency, which is generally referred to as the "trend". The ramp ice history is suitable for both describing one of the two parts of the seasonal signal and the trend. However, since I did not expect to find any appreciable difference between elastic, viscoelastic or transient models over time periods smaller than $\approx$ a year, for these tests I considered only ramp histories whose length τ is of the order of $\sim 10^1\ yr$ and $\sim 10^2\ yr$. These ramps aim at being representative examples of the mass losses that many ices around the world have experienced during last century. Also the extent of the load, that has a half-amplitudes of 0.3°, corresponding to a radius of about $\sim 30\ km$, symbolizes a medium-size glacier.

The first target of this experiment is understanding if, over a time-window comparable with those of GNSS records, transient deformations can be significant. The second purpose is understanding the role of the ramp length, to figure out which impact it has in the occurrence of transient deformations.

The Earth's models considered here are the same as in previous section, plus some "elastic" models (in green in the plots), whose density and rigidity layering is identical to that of the viscoelastic counterpart. These model serves as a reference to better quantify the amount of viscoelastic contributions predicted by the other models.

5.3.1 Role of the Ramp duration

The first set of tests considers a disc load of half-amplitude 0.3°, that, over a variable period τ, loses mass with a constant height decrease of 10 m/yr. This rate, quite large, has been chosen as an upper limit for the ice loss, a sort of best case scenario: it suffices to know that in the case of Helheim Glacier, that will be presented in next section, the maximum height loss effectively accounted by the model used in this Thesis is around $7m/yr$. Thus, the results shown in the following must be read in a qualitative way rather than a quantitative one: once again, the aim is understanding how the combination of parameters regulate the final result.

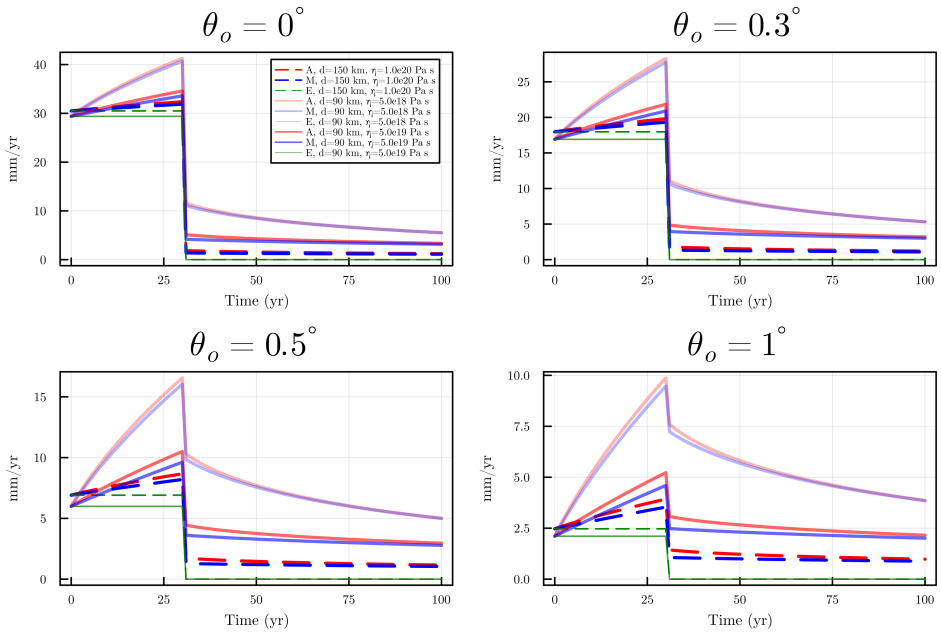

(a) ***Ramp length:*** 30 yr, ***Ice loss rate:*** 10 m/yr

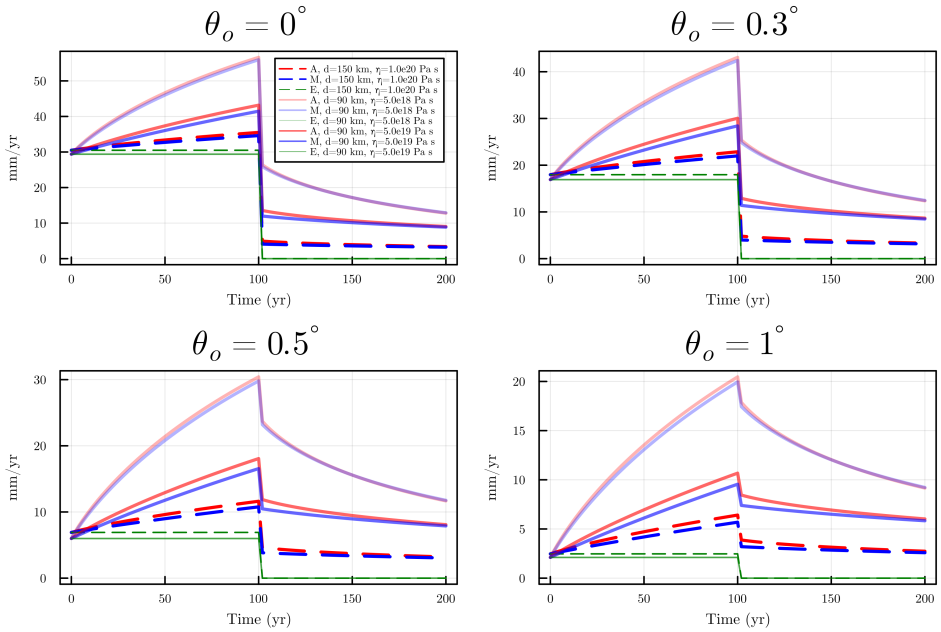

(b) ***Ramp length:*** 100 yr, ***Ice loss rate:*** 10 m/yr

Figure 5.14: **Vertical uplift rates** for different observation points ($\theta_o = 0°$, 0.3°, 0.5°, 1°). The legend with the models description is reported in the first panel of each group.

In Figure 5.14 the results of a ramp unloading of $\tau = 30\ yr$ and $\tau = 100\ yr$ are shown, for several Earth models. Red curves refer to "Andrade" configurations, blue to "Maxwell" ones, and the green ones are the Elastic models, that constitute the reference models. The intensity of colors is related to the viscosity values, while the type of curve (dashed or solid) refers to the lithosphere thickness. The motivation behind this particular choice of models is easily said: my purpose was to investigate how "softer" and "harder" models respond to ramp unloading. The "harder" ones, those indicated by dashed curves, have a very thick lithosphere (150 km) and high value of viscosity ($1 \cdot 10^{20} Pa \cdot s$), and are also those that produce results more similar to the elastic response, characterized by a constant rate during all the unloading phase $0 < t < \tau$, and the instantaneous achievement of the equilibrium right after the disappearance of the load, exhibiting thus a vanishing velocity for $t > \tau$. On the other hand, the models outlined by the solid curves, especially the lightest, those with the lowest viscosity value, $5 \cdot 10^{18} Pa \cdot s$, are those which mostly differ from the elastic results, showing increasing rates during all the duration of the ramp.

To compare the two panels (a) and (b) of Figure 5.14 it is important to remark that, while the ice loss rate is the same, $10 m/yr$, the total height loss is extremely different: for the 30 yr long ramp, it is 300 m, whilst in the other case is 1000 m. For this reason, the uplift rates at the end of the unloading phases are very different. In panel (b), the presence of a longer ramp allows to better appreciate, especially for the "softer" models, an initial moment of decreasing acceleration, that later settles around a constant value. A common characteristic to both panels is the fact that the rate drop at $t = \tau$ decreases in magnitude, with the distance from the centre of the load. Also, the magnitude of this drop seems to be independent from the ramp length.

As regard the differences between the pairs of Andrade and Maxwell models, during the unloading phase, while $(t < \tau)$, they have an initial stage in which they increase, until they adjust on two parallel paths; then, at $t = \tau$, the disappearance of the load

causes an abrupt decrease in the rates. In this second phase, the softer models, those with $\eta = 5 \cdot 10^{18} Pa \cdot s$, show very little differences between each other, while the ones with $\eta = 5 \cdot 10^{19} Pa \cdot s$ reflect a more visible discrepancy, especially right after the sudden drop. This suggests that, at least for this configuration of the Earth model and load size, lower values of viscosities in the SUM do not help in recognizing the presence of any transient pattern; instead, if we considered more viscous SUMs, the discrepancies between Maxwell and Andrade arise more clearly. In the next subsection 5.3.2 I will investigate with more detail the role of the SUM viscosity. However, it is also true that higher values of viscosity produce trends that are very similar to the elastic ones, making the identification of any inelastic contribution more difficult.

To conclude, we can see that the presence of a thicker lithosphere, as suggested by the dashed models, would make it more difficult to distinguish between "Maxwell" and "Andrade" configuration, limiting the influence of the viscoelastic SUM on the resulting uplift rates.

5.3.2 Role of the shallow upper mantle viscosity

The previous tests suggest that some values of the SUM (shallow upper mantle) viscosity intensify the differences between the rates produced by the "Maxwell" and the "Andrade" configuration. From Figure 5.14, it appears that these discrepancies are maximized by high values of viscosity. To understand the role of the viscosity, I ran a set of tests using different ramp lengths ($30, 100\ yr$), considering a wider range of viscosities for the SUM. The results, presented in Figure 5.15, refer to the rates observed at the centre of the load ($\theta_o = 0°$). The first plot on the left (in blue) represents the output rates from Maxwell configurations, on the right (in red) we have the Andrade ones and lastly, below, (in green) the differences between the two. It is clear that, as previously anticipated, higher values of viscosity increase the difference between the two models. Moreover, these discrepancies increase with time: at the very beginning of the ramp, we can clearly see in

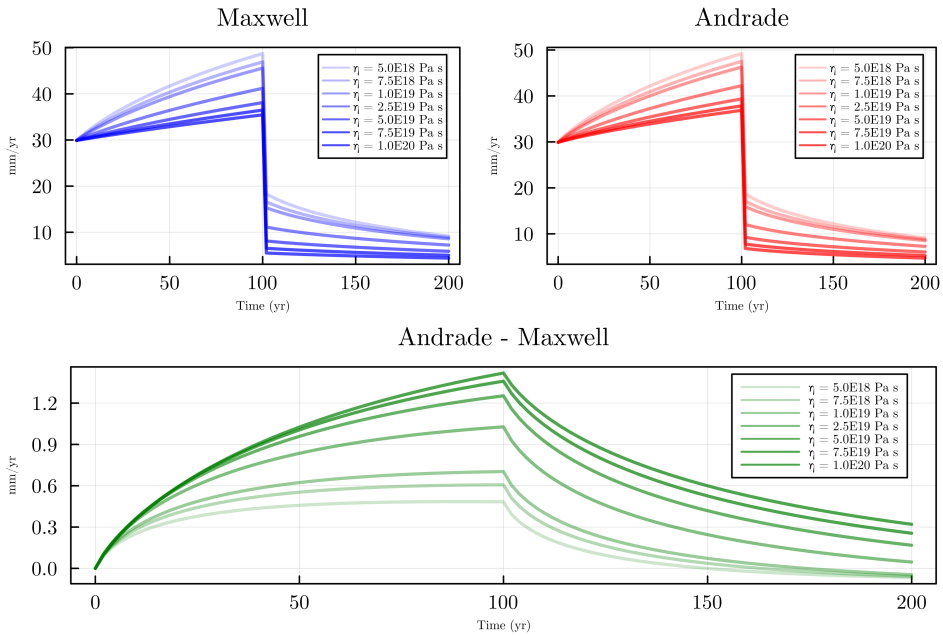

(a) ***Ramp length:*** 100 yr, ***Ice loss rate:*** 10 m/yr

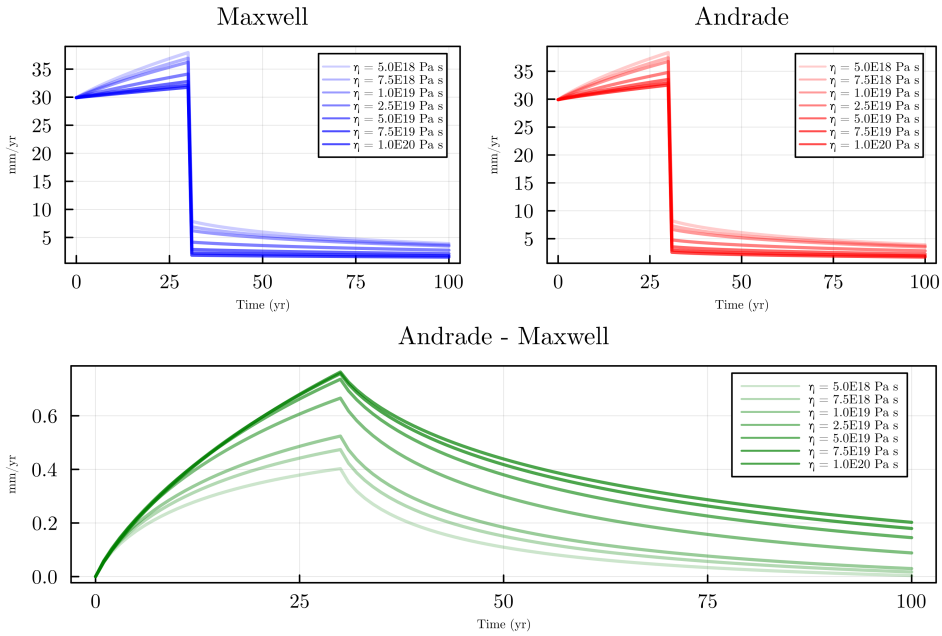

(b) ***Ramp length:*** 30 yr, ***Ice loss rate:*** 10 m/yr

Figure 5.15: **Uplift rates at** $\theta_o = 0°$, for various values of the viscosity of the SUM of Maxwell's (blue) and Andrade's (red) models, and their difference (green).

the "Andrade-Maxwell" plots that all the curves assume similar values, and then, only after some time, they start to diverge. Nevertheless, it is true that even if we increase the discrepancies by increasing the viscosity, we are also making the model to be more elastic: thus, the amount of viscoelastic contribution will decrease, making it difficult to recognize them.

The main outcomes of this section are:

- Viscosity has a double action. On one hand, high viscosity values help to distinguish between "Maxwell" and "Andrade", but on the other hand, they suppress the viscoelastic contribution, making the trend much similar to those produced by the elastic models.

- A long unloading phase gives the model the time to manifest possible peculiar features. By comparing the two group of plots in Figure 5.14, it is clear that, in the case of ramp length $\tau = 100\ yr$, the Maxwell and Andrade's output have more time to develop their discrepancies and, at the end, their differences have a greater magnitude *w.r.t.* the case of $\tau = 30\ yr$. Of course this is permitted by the fact that the melting rate of the ice mass is constant, and that, at the end of the day, the net mass loss is extremely different in the two cases, so we are basically comparing two ice masses of different size that melt at the same rate.

- Differently from the previous experiment, the presence of an ice history that evolves gradually does not allow any sudden changes, making it more difficult to infer any transient features.

5.4 A case study: the Helheim glacier

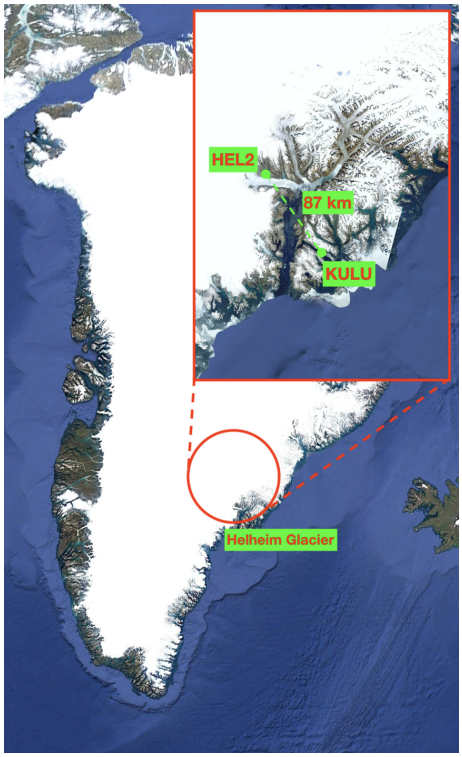

Figure 5.16: **Helheim Glacier.** The two GNSS stations HEL2 and KULU are evidenced by green labels.

The Helheim glacier (Figure 5.16) is one of the largest marine terminating outlet glaciers in Greenland: it is located in the southeast and it has a total area of approximately $50,000\ km^2$. The interest toward this glacier is due to its high rates of solid ice discharge, as well as its wide-ranging dynamics, that showed episodes of multi-annual retreats and re-advances in the last 20 years (Ultee et al., 2022). The first of them began between 2003-2005, when the glacier started showing a dramatic retreat (Williams et al., 2021). According to Williams et al. (2021), Helheim is now more vulnerable than at any moment since the Little Ice Age, meaning that the ice loss rate could reach a tipping point capable of pushing it into a new dynamic state. The two nearest GNSS station to the glacier are HEL2 (lat : 66.4012; $lon = -38.2157$) and KULU ($lat = 65.5793$; $lon = -37.1494$); the former is located in the proximity of the ice, whilst the latter is around 100 km distant. Thus, HEL2 is expected to be extremely sensitive to Helheim dynamics and mass balance variation: here the local signal of the glacier is superimposed with the elastic uplift of the surface due to the ice sheet and the viscoelastic response due to GIA. If the Helheim mass variations are able to trigger a transient response in the Earth, this station should be close enough to detect them. On the contrary, KULU is too far to be influenced significantly from Helheim glacier, but should report a signal of elastic rebound (ER) and glacial isostatic adjustment (GIA) similar to those observed at HEL2. The aim of this last test is under-

standing whether it is possible, under model conditions that try to mimic the structure of the Earth in the region of Helheim, to discern any transient signal during an observation time-period comparable with the one of GNSS records ($\sim 15\ yr$).

The ice model (courtesy of Dr. V. Barletta and Dr. Cheng Gong) consists in 46,434 disc elements of variable area, each associated to a rate of height variation (m/yr). The rates refer to a 15-year period, from January 2007 to January 2022. Among those used in this Thesis, this ice model is the more realistic. Here, the Earth's models considered have always a lithospheric thickness of 110 km, representative of the Helheim area.

The first experiments were performed considering that the ice history of each disc was represented by a Heaviside unloading. With respect to the typical time scales of GIA, $10^3\ yr$, a deglaciation of $15yr$ can be considered, in first approximation, instantaneous. Of course, this is not what is happening in Helheim, but this first experiment aims at evaluating the response of the Earth's models to a sudden change of the surface load. To apply the results of this test to a real scenario, one simply needs to rescale the amount of lost mass in order to represent a surge event or an episode of anomalous melting. This adjustment will affect only the magnitude of the resulting displacements, without altering their relative differences or temporal evolution. The results are in Figures 5.17, 5.18, 5.19, which show displacement rates obtained with a SUM viscosity of $5.0{\cdot}10^{18} Pa{\cdot}s$, $5.0 \cdot 10^{19} Pa \cdot s$ and $1.0 \cdot 10^{20} Pa \cdot s$, respectively. The difference between Figure 5.17 and the other two (Figures 5.18 and 5.19) is noteworthy: such a low viscosity in the SUM allows the "Maxwell" model to assume a trend that is very similar to the Andrade's one. On the contrary, the cases in which η_{SUM} was set to $5.0 \cdot 10^{19} Pa \cdot s$ (Figure 5.18) and $1.0 \cdot 10^{20} Pa \cdot s$ (Figure 5.19) exhibit a rate that for the "Maxwell" model is almost constant. Andrade's model instead, clearly shows a time dependent decay, that only for time $t > 15\ yr$ assumes a nearly steady state. However, the magnitude of these rates is quite small. A possible explanation could be that for this very case, a better resolution in the layering of the lithosphere is necessary to obtain more reliable results.

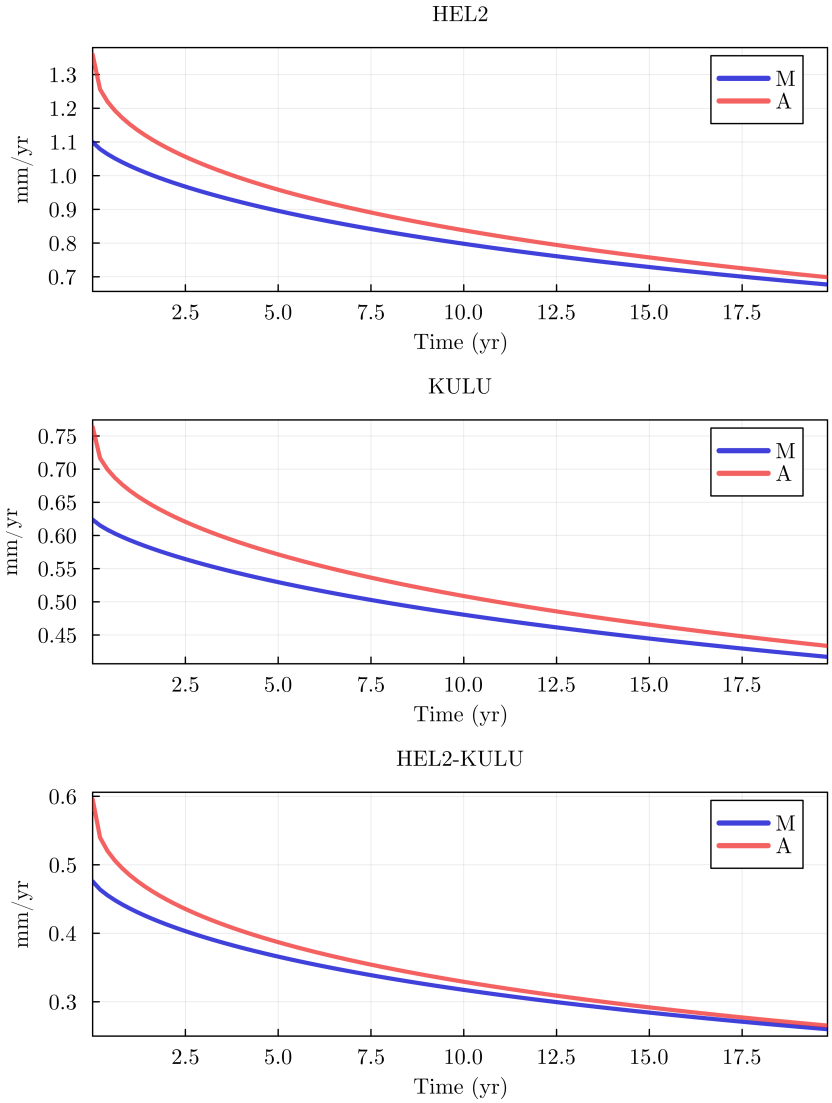

Figure 5.17: **Vertical rates** at HEL2 and KULU stations, and the difference HEL2-KULU assuming a Heaviside unloading. Earth model with rheological configurations "Andrade" and "Maxwell", $\eta_{SUM} = 5.0 \cdot 10^{18} Pa \cdot s$. Notice that the y-scale is different in each plot.

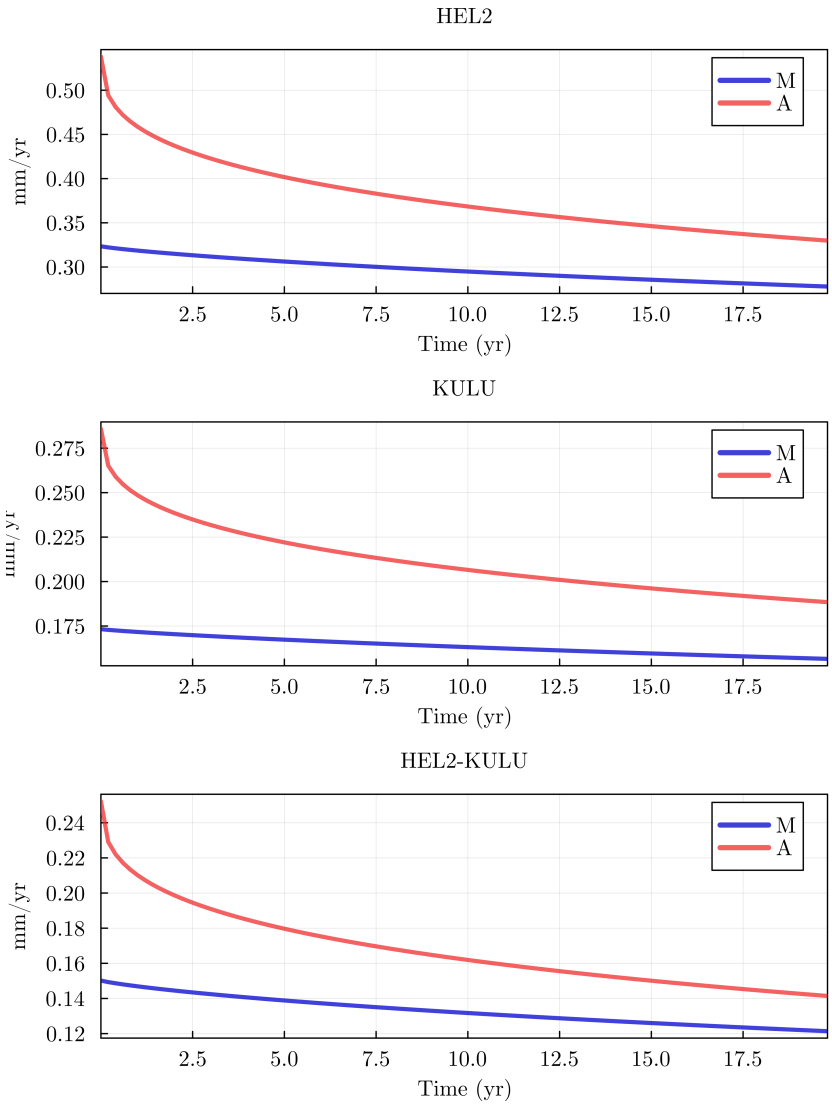

Figure 5.18: **Vertical rates** at HEL2 and KULU stations, and the difference HEL2-KULU assuming a Heaviside unloading. Same as Figure 5.17, but for $\eta_{SUM} = 5.0 \cdot 10^{19} Pa \cdot s$. Notice that the y-scale is different in each plot.

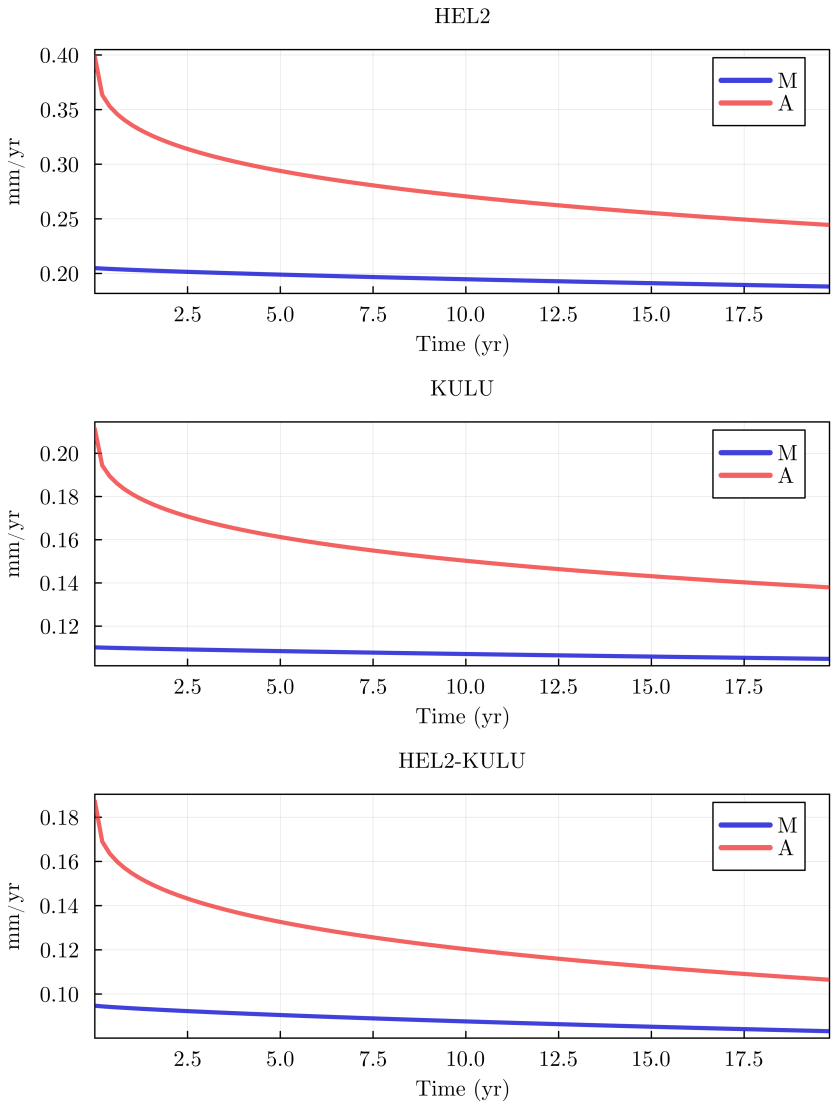

Figure 5.19: **Vertical rates** at HEL2 and KULU stations, and the difference HEL2-KULU assuming a Heaviside unloading. Same as Figure 5.17 and 5.18 but for $\eta_{SUM} = 1.0 \cdot 10^{20} Pa \cdot s$. Notice that the y-scale is different in each plot.

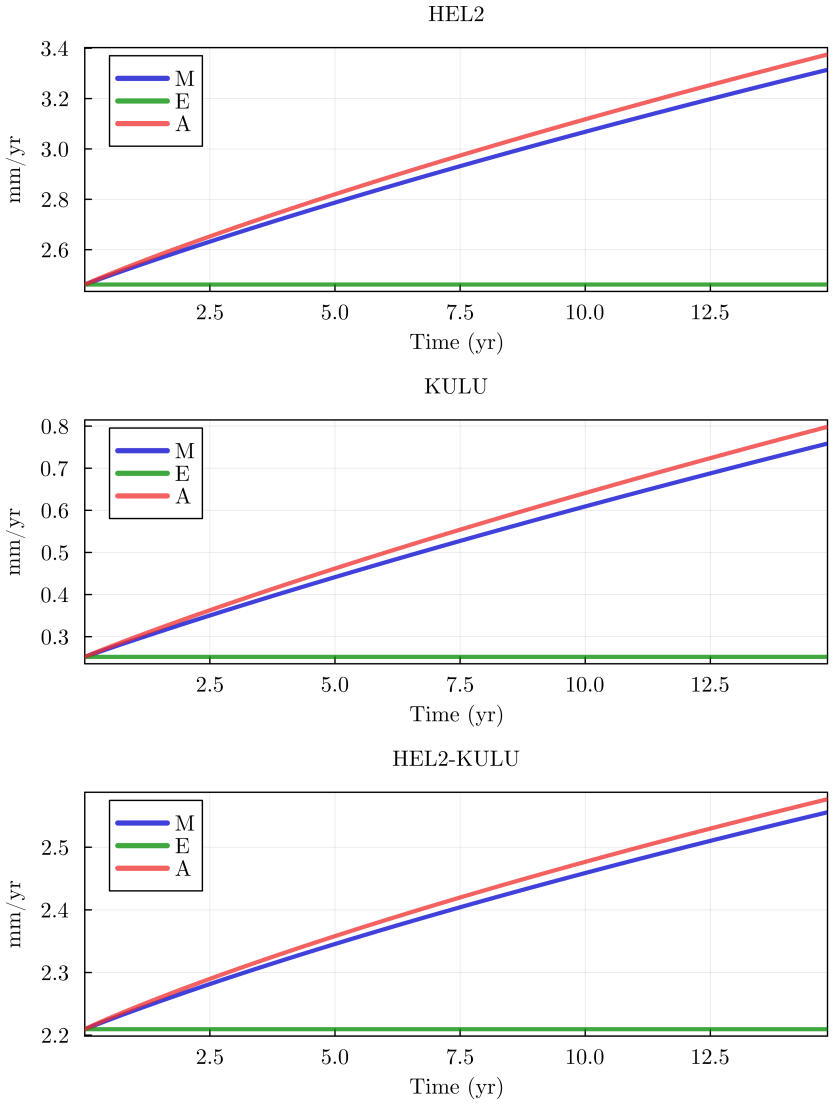

Figure 5.20: **Vertical rates** at HEL2 and KULU stations, and the difference HEL2-KULU assuming a ramp unloading. Earth model with rheological configurations "Andrade" and "Maxwell", $\eta_{SUM} = 5.0 \cdot 10^{18} Pa \cdot s$. Notice that the y-scale is different in each plot.

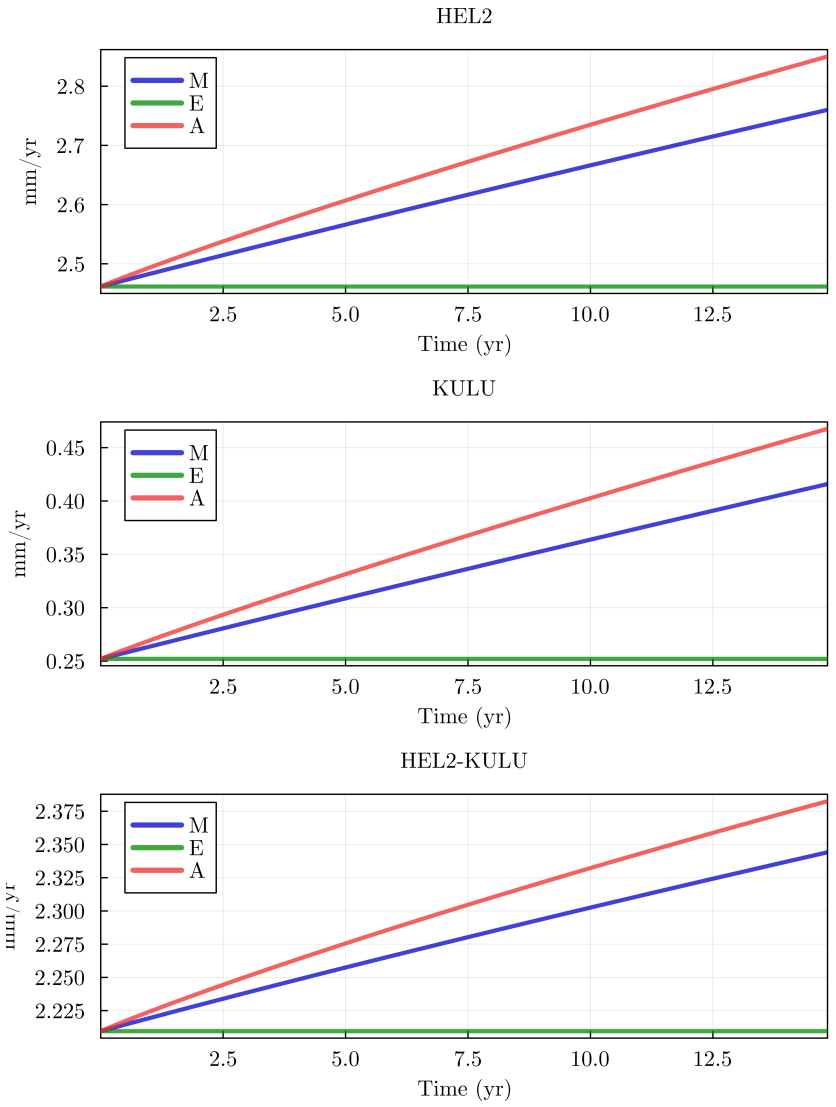

Figure 5.21: **Vertical rates** at HEL2 and KULU stations, and the difference HEL2-KULU assuming a ramp unloading. Same as Figure 5.20 but for $\eta_{SUM} = 5.0 \cdot 10^{19} Pa \cdot s$. Notice that the y-scale is different in each plot.

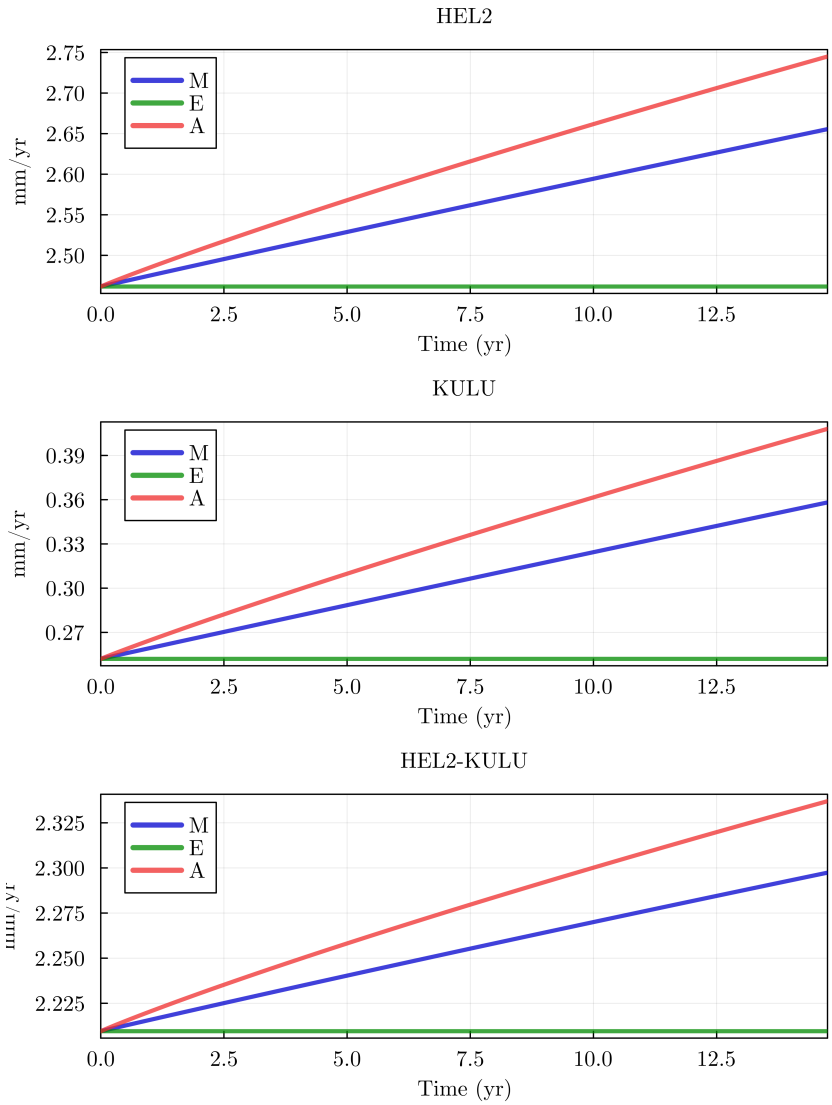

Figure 5.22: **Vertical rates** at HEL2 and KULU stations, and the difference HEL2-KULU assuming a ramp unloading. Same as Figure 5.20 and 5.21 but for $\eta_{SUM} = 1.0 \cdot 10^{20} Pa \cdot s$. Notice that the y-scale is different in each plot.

Then, the second round of experiments considers a ramp unloading for each disc element. This approach is similar to that adopted by Boughanemi and Mémin (2024): in their works, the authors obtained a ramp unloading using a sequence of Heaviside step functions. Our result should be theoretically consistent, with the only difference being that using a pure ramp function should prevent the presence of artifacts in the output. Figures 5.20, 5.21 and 5.22 display the output rate for different values of the SUM viscosity ($5 \cdot 10^{18} Pa \cdot s$, $5 \cdot 10^{19} Pa \cdot s$, and $1 \cdot 10^{20} Pa \cdot s$). The first noticeable difference *w.r.t.* the previous set of experiment is that here the "Maxwell" and "Andrade" models produce much similar trends, with no distinctive features. This result was already presented in the previous section, and must be attributed to the fact that a Heaviside ice history represents a sort of "shock" for the Earth's model, that is suddenly subject to an instantaneous mass redistribution. Instead, with the ramp ice history, the evolution of the ice is more regular, and the Earth model must adjust, at each time steps to smaller mass redistribution.

As regard Figures 5.20, 5.21 and 5.22, we can appreciate that the models with the lowest value of viscosity (Figure 5.20) are the ones that produce the highest rates at the end of the unloading period; however, like we have seen in the section regarding the ramp experiment, the model with the higher value of SUM viscosity $\eta = 1.0 \cdot 10^{20} Pa \cdot s$ is that which shows the greatest differences between the "Andrade" and "Maxwell" rheologies. Nevertheless, at the end of the ramp, their rates deviate only of $\sim 0.1\ mm/yr$, and the two curves show a very similar evolution, making these two results hard to discern on the field. We can conclude that, under these experimental conditions it would not be possible to identify any transient: by tuning the value on the SUM viscosity the Maxwell model could produce a trend equivalent to the Andrade's one.

However, a remarkable outcome is the difference of the viscoelastic curves (both Maxwell and Andrade) from the elastic one. Considering Figure 5.22, we can conclude that at HEL2, in 15 yr, the viscoelastic models have reached a rate that is a 10%

greater than the constant elastic rate. This suggests to investigate what would happen if these rates were extended over a longer time period. This is exactly what Figure 5.23 shows: I supposed that the observed rate at Helheim were obtained after a 30-years long measurement campaign, something that will be possible in the next future. In this hypothetical case, the final rates produced by the models with $\eta_{SUM} = 5.0 \cdot 10^{18} Pa \cdot s$ and $\eta_{SUM} = 1.0 \cdot 10^{20} Pa \cdot s$ are, respectively, 3.9 and 2.9 mm/yr, while the elastic counterpart exhibits a fixed trend around 2.4 mm/yr. This means an increase *w.r.t.* the initial elastic rate of 60% and 20% respectively. Nevertheless, even if it is true that with a longer observation window the discrepancies between "Andrade" and "Maxwell" models increase, the general evolution of the trends is similar, and the effects of rheology can be mimicked by adequately tuning the viscosity.

This fact suggests that, in the near future, the concept of "elastic" contribution could become no longer adequate to account for geodetic observations: as I discussed in the introduction, the general approach used to justify the rates at Greenland GNSS stations is considering the record as the result of the sum of the elastic displacement due to present day ice evolution, and a viscoelastic contribution from GIA.

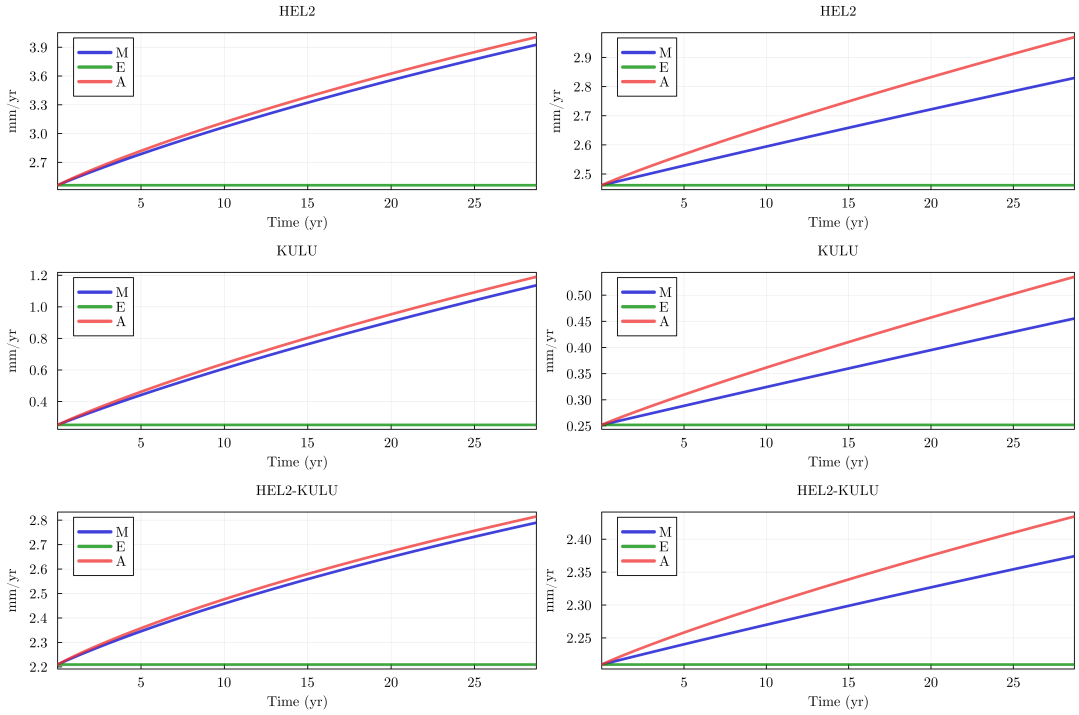

(a) ***Ramp length:*** $30\ yr$, $\eta = 5.0 \cdot 10^{18} Pa \cdot s$

(b) ***Ramp length:*** $30\ yr$, $\eta = 1.0 \cdot 10^{20} Pa \cdot s$

Figure 5.23: **Uplift rates at HEL2 and KULU**, for models with SUM viscosity of $\eta = 5.0 \cdot 10^{18} Pa \cdot s$ and $\eta = 1.0 \cdot 10^{20} Pa \cdot s$ respectively.

Chapter 6

Concluding remarks and outlook

In this Thesis work, I have explored the possible effects of transient rheology on the surface response of a spherical planet, with a particular attention to the region of Greenland.

The first part of my research (Chapter 2) has been devoted to a full investigation of the Andrade rheology, a transient model that has gained much success in the latest years, especially in planetary science. The main results include two previously unknown analytical expressions: the Andrade's relaxation modulus and the the Love numbers of a uniform sphere with Andrade rheology. These formulas can be employed to assess the deformation and gravity field variations of planets (and exoplanets) with unknown or poorly constrained structure, to obtain a first approximate estimate of their response to tidal or surface forcing. Since they contain the higher transcendental Mittag-Leffler Function, they are characterized by a certain degree of complexity. By an analytical approach, I have demonstrated that they obey a series of limiting cases that further confirm their correctness. These include the elastic limit for $t \to 0$, the fluid limit for $t \to \infty$ and the Maxwell limit for $\zeta \to \infty$.

In Chapter 3, I have approached the calculation of Love numbers for a spherical, symmetric and incompressible planet. Particularly, for the case of a two-layer fluid, inviscid

planet, together with my supervisor and co-supervisor, we retrieved a surprisingly simple approximated relation between the normalized LN $\tilde{k}_2$ and the normalized moment of inertia $\tilde{N}$, which reads $\tilde{N} \sim \tilde{k}_2^{0.4}$, and which provides a good estimate of $\tilde{N}$ as a function of k_2 over a wide range of possible two-layer models. We have verified that in case of gravitationally stable planetary models with an arbitrarily large number of homogeneous layers, this rule of thumb provides an upper limit to the possible range of mean moment of inertia corresponding to a given value of $\tilde{k}_2$. Remarkably, the simulations have shown that, especially for small values of k_2, the ROT is more accurate than the celebrated Radau-Darwin formula.

Finally, in the last part of the Thesis, I have delved into the analysis of some case studies, sorted for increasing complexity. I have explored the role of several parameters involved in the determination of the SRF. The aim was to outline the best condition in which it is possible to distinguish transient effects following surface unloading events, with a particular attention to the applications in the Greenland region.

For this part, my main conclusions are:

- **Rheology**: Identifying a clear transient pattern following a surface unloading event is not straightforward. From the comparison of the Heaviside ice histories and the ramp ones, it follows that rapid changes in the ice evolution, *i.e.,* sudden modifications of the system, are those in which the transient features arise more clearly. Instead, in case of a gradual and smooth ice history, like the ramp one, distinguishing between a viscoelastic model and a transient one is hardly possible.

- **Viscosity**: it plays a crucial role in the determination of the magnitudes of the displacement rates. Low viscosities have been suggested in presence of anomalously fast GNSS rates (Nield et al., 2014; Barletta et al., 2018, 2022). However, the effects of viscosity can be confused with those produced by a "softer" rheological model, like the Andrade's one. Indeed, as we have seen here, the transient in Andrade's rheology allows for a faster transition between the elastic phase and the viscous

flow. Nevertheless, in view of the not clear difference between the vertical pattern produced by a low viscosity or that due to a different rheological mechanism, it is not possible to draw further conclusions. To do so, an independent constraint on the viscosity value would be necessary.

- **Lithosphere**: The thickness of the lithosphere is another important parameter. By fixing it, we are setting the depth of the first viscoelastic layer, and thus we are setting a lower limit for the ice load dimension: if the load has a smaller size, it will not sense the presence of the viscoelastic layers, that lay too deep beneath the surface. To have an idea of the length-scales involved in a general experiment, a good point to start is plotting the load coefficients, to understand which harmonic degrees (and so, which spatial scales) are more significant.

- **Distance from the centre of the load**: Some of the outcomes of the first experiment suggest that a large part of the Earth response is "hidden" beneath the ice load. As we increase the distance of the observation point, we start noting that not only the magnitude of the rates diminishes, but also that the discrepancies between the various models is washed out.

I believe it is important to highlight some of the limitations of my modeling approach and of the numerical tests performed. First of all, the maximum harmonic degree of my computation is set to $l_{max} = 1024$. Although for the first two experiments this parameter is appropriate in view of Jeans' rule (Jeans, 1923; Bevis et al., 2016), it is legitimate to wonder whether this is also the case of the last experiment. Indeed, in this last case, I considered a set of smaller disc loads with variable amplitude. Another consideration concerns the lithospheric model. Here I assumed a thick, homogeneous layer, while in general, in Elastic Rebound modeling (see Spada et al. (2012); Nielsen et al. (2012); Adhikari et al. (2021)), the PREM model is often employed. In this way, one disposes of a more detailed description of the outermost layer of the Earth, since this model assumes

that the density ρ, and the Lamé constants μ and λ are defined through polynomial functions of radius r. Of course, the choice of a uniform lithosphere may affect the magnitude of the computed rates of deformation. Also, one must wonder whether a perfectly elastic lithosphere is indeed a correct model of the Earth's outer layer (Ranalli, 1995).

Speaking of which, the anelastic contributions in the lithosphere or in the crust may affect the modeled rates. This issue has been discussed in Durkin et al. (2019): in this work, the authors correct the values of rigidity to account for local inelastic contribution, showing that they can produce uplift rates with a discrepancy up to 20–40% with respect to those modeled using PREM. Regarding the rheological model, all the experiments have been performed setting the values of the Andrade's parameters to $\alpha = 1/3$ and $\zeta = 1$. The influence on the SRF of a variation of these two parameters has not been considered in this work.

To sum up, the optimal conditions that increase the possibility of observing and identifying transient features include the geographical proximity of the GNSS station, the observation point, from the source of the unloading, or even better, an observation point below the load, and the presence of shallow lithospheres, i.e. not too deep viscoelastic layers. This implies that much effort should be placed into subglacial geodesy, a field that is not yet achieved and that would enable direct observation of the Earth response to ice unloading beneath glaciers and ice sheets (Schroeder et al., 2024).

The presence of a low viscosity zone does not imply higher chances to infer transient deformations, but if further constraints on the viscosity are available, then it may become possible to discern between a full-Maxwell SUM, or a more complicated model.

In the last experiment, I had the chance of evaluating the effect of a more realistic ice model. From this last case, it is apparent that the viscoelastic and anelastic components in the displacements represent a significant contribution already at decadal time scales. This is consistent with the findings of Ivins et al. (2020); Adhikari et al. (2021); Paxman

et al. (2023) and Lau (2024). This suggests that in the near future, it may be necessary to surpass the modeling of a pure elastic response to present-day ice melting, in favor of a more rheologically sophisticated Earth's model.

Bibliography

1. Adhikari, S., Milne, G., Caron, L., Khan, S., Kjeldsen, K., Nilsson, J., Larour, E. and Ivins, E. (2021), 'Decadal to centennial timescale mantle viscosity inferred from modern crustal uplift rates in Greenland', *Geophysical Research Letters* **48**(19), e2021GL094040.

2. Akinsanmi, B., Barros, S., Santos, N., Correia, A., Maxted, P., Boué, G. and Laskar, J. (2019), 'Detectability of shape deformation in short-period exoplanets', *Astronomy & Astrophysics* **621**, A117.

3. Alterman, Z., Jarosch, H. and Pekeris, C. L. (1959), 'Oscillations of the earth', *Proceedings of the Royal Society of London. Series A. Mathematical and Physical Sciences* **252**(1268), 80–95.

4. Amorim, D. O. and Gudkova, T. (2024), 'Constraining Earth's mantle rheology with Love and Shida numbers at the M2 tidal frequency', *Physics of the Earth and Planetary Interiors* **347**, 107144.

5. Andrade, E. N. D. C. (1910), 'On the viscous flow in metals, and allied phenomena', *Proceedings of the Royal Society of London. Series A, Containing Papers of a Mathematical and Physical Character* **84**(567), 1–12.

6. Andrade, E. N. D. C. (1962), 'The validity of the $t^{1/3}$ law of flow of metals', *Philosophical Magazine* **7**(84), 2003–2014.

7. Bagheri, A., Khan, A., Al-Attar, D., Crawford, O. and Giardini, D. (2019), 'Tidal response of Mars constrained from laboratory-based viscoelastic dissipation models and geophysical data', *Journal of Geophysical Research: Planets* **124**(11), 2703–2727.

8. Barletta, V. R., Bevis, M., Smith, B. E., Wilson, T., Brown, A., Bordoni, A., Willis, M., Khan, S. A., Rovira-Navarro, M., Dalziel, I. et al. (2018), 'Observed rapid bedrock uplift in Amundsen Sea Embayment promotes ice-sheet stability', *Science* **360**(6395), 1335–1339.

9. Barletta, V. R., Bordoni, A. and Khan, S. A. (2024), 'GNET derived mass balance and glacial isostatic adjustment constraints for Greenland', *Geophysical Research Letters* **51**(9), e2023GL106891.

10. Barletta, V. R., Sørensen, L. S. and Forsberg, R. (2013), 'Scatter of mass changes estimates at basin scale for Greenland and Antarctica', *The Cryosphere* **7**(5), 1411–1432.

11. Barletta, V. R., van der Wal, W., Bordoni, A. and Khan, S. A. (2022), Effect of icelandic hotspot on mantle viscosity in southeast greenland, *in* 'EGU General Assembly Conference Abstracts', pp. EGU22–10884.

12. Barros, S., Akinsanmi, B., Boué, G., Smith, A., Laskar, J., Ulmer-Moll, S., Lillo-Box, J., Queloz, D., Cameron, A. C., Sousa, S. et al. (2022), 'Detection of the tidal deformation of WASP-103b at 3 σ with CHEOPS', *Astronomy & Astrophysics* **657**, A52.

13. Bennike, O., Björck, S. and Lambeck, K. (2002), 'Estimates of South Greenland late-glacial ice limits from a new relative sea level curve', *Earth and Planetary Science Letters* **197**(3-4), 171–186.

14. Berg, D., Barletta, V., Hassan, J., Lippert, E., Colgan, W., Bevis, M., Steffen, R. and Khan, S. (2024), 'Vertical Land Motion Due To Present-Day Ice Loss From Greenland's and Canada's Peripheral Glaciers', *Geophysical Research Letters* **51**(2), e2023GL104851.

15. Bevis, M., Melini, D. and Spada, G. (2016), 'On computing the geoelastic response to a disk load', *Geophysical Journal International* **205**(3), 1804–1812.

16. Bevis, M., Wahr, J., Khan, S. A., Madsen, F. B., Brown, A., Willis, M., Kendrick, E., Knudsen, P., Box, J. E., van Dam, T. et al. (2012), 'Bedrock displacements in Greenland manifest ice mass variations, climate cycles and climate change', *Proceedings of the National Academy of Sciences* **109**(30), 11944–11948.

17. Bierson, C. and Nimmo, F. (2016), 'A test for Io's magma ocean: Modeling tidal dissipation with a partially molten mantle', *Journal of Geophysical Research: Planets* **121**(11), 2211–2224.

18. Boas, M. L. (2006), *Mathematical methods in the physical sciences*, John Wiley & Sons.

19. Boughanemi, A. and Mémin, A. (2024), 'Effects of Andrade and Burgers rheologies on glacial isostatic adjustment modeling in Antarctica', *Geodesy and Geodynamics* **15**(5), 429–440.
URL: *https://www.sciencedirect.com/science/article/pii/S167498472400017X*

20. Boussinesq, J. (1885), *Application des potentiels à l'étude de l'équilibre et du mouvement des solides élastiques: principalement au calcul des deformations et des pressions que produisent, dans ces solides, des efforts quelconques exercés sur und petite partie de leur surface ou de leur intérieur; memoire suivi de notes étendues sur divers points de physique mathématique et d'analyse*, Gauthier-Villars.

21. Carter, J. A. and Winn, J. N. (2010), 'Empirical constraints on the oblateness of an exoplanet', *The Astrophysical Journal* **709**(2), 1219.
URL: *https://dx.doi.org/10.1088/0004-637X/709/2/1219*

22. Castillo-Rogez, J. C., Efroimsky, M. and Lainey, V. (2011), 'The tidal history of Iapetus: Spin dynamics in the light of a refined dissipation model', *Journal of Geophysical Research: Planets* **116**(E9).

23. Castillo-Rogez, J., Weiss, B., Beddingfield, C., Biersteker, J., Cartwright, R., Goode, A., Melwani Daswani, M. and Neveu, M. (2023), 'Compositions and interior structures of the large moons of Uranus and implications for future spacecraft observations', *Journal of Geophysical Research: Planets* **128**(1), e2022JE007432.

24. Cerruti, V. (1882), *Ricerche intorno all'equilibrio de' corpi elastici isotropi*, Salviucci.

25. Chandrasekhar, S. and Milne, E. A. (1933), 'The Equilibrium of Distorted Polytropes: (I). The Rotational Problem', *Monthly Notices of the Royal Astronomical Society* **93**(5), 390–406.
URL: *https://doi.org/10.1093/mnras/93.5.390*

26. Choi, Y., Morlighem, M., Rignot, E. and Wood, M. (2021), 'Ice dynamics will remain a primary driver of Greenland ice sheet mass loss over the next century', *Communications Earth & Environment* **2**(1), 26.

27. Christensen, R. (1982), *Theory of Viscoelasticity*, Dover, Mineola, New York.

28. Consorzi, A. (2021), Role of transient deformation in Glacial Isostatic Adjustment, Master Thesis, University of Bologna, Bologna, Italy.

29. Consorzi, A., Melini, D., González-Santander, J. L. and Spada, G. (2024), 'On the Love Numbers of an Andrade Planet', *Earth and Space Science*

11(9), e2024EA003779.
URL: *https://agupubs.onlinelibrary.wiley.com/doi/abs/10.1029/2024EA003779*

30. Consorzi, A., Melini, D. and Spada, G. (2023), 'Relation between the moment of inertia and the k_2 Love number of fluid extra-solar planets', *Astronomy & Astrophysics* **676**, A21.

31. Cook, A. H. (1980), 'Interiors of the Planets', *Cambridge Planet. Science Series* .

32. Correia, A. C. (2014), 'Transit light curve and inner structure of close-in planets', *Astronomy & Astrophysics* **570**, L5.

33. Cottrell, A. (1996), 'Andrade creep', *Philosophical Magazine Letters* **73**(1), 35–36.

34. Cottrell, A. (2004), 'A microscopic theory of Andrade creep', *Philosophical Magazine Letters* **84**(11), 685–689.

35. Cottrell, A. and Aytekin, V. (1947), 'Andrade's creep law and the flow of zinc crystals', *Nature* **160**(4062), 328–329.

36. Durkin, W., Kachuck, S. and Pritchard, M. (2019), 'The importance of the inelastic and elastic structures of the crust in constraining glacial density, mass change, and isostatic adjustment from geodetic observations in Southeast Alaska', *Journal of Geophysical Research: Solid Earth* **124**(1), 1106–1119.

37. Efroimsky, M. (2012*a*), 'Bodily tides near spin–orbit resonances', *Celestial Mechanics and Dynamical Astronomy* **112**(3), 283–330.

38. Efroimsky, M. (2012*b*), 'Tidal dissipation compared to seismic dissipation: In small bodies, earths, and super-earths', *The Astrophysical Journal* **746**(2), 150.

39. Farrell, W. (1972), 'Deformation of the Earth by surface loads', *Reviews of Geophysics* **10**(3), 761–797.

40. Farrell, W. and Clark, J. A. (1976), 'On postglacial sea level', *Geophysical Journal International* **46**(3), 647–667.

41. Fung, Y. (1965), *Foundations of Solid Mechanics*, Prentice-Hall.

42. Gevorgyan, Y., Boué, G., Ragazzo, C., Ruiz, L. S. and Correia, A. C. (2020), 'Andrade rheology in time-domain. Application to Enceladus' dissipation of energy due to forced libration', *Icarus* **343**, 113610.

43. Gomez, N., Pollard, D. and Holland, D. (2015), 'Sea-level feedback lowers projections of future antarctic ice-sheet mass loss', *Nature communications* **6**(1), 8798.

44. González-Santander, J. L., Spada, G., Mainardi, F. and Apelblat, A. (2024), 'Calculation of the relaxation modulus in the Andrade model by using the Laplace transform', *Fractal and Fractional* **8**(8), 439.

45. Gorenflo, R., Kilbas, A. A., Mainardi, F. and Rogosin, S. (2020), *Mittag-Leffler functions, related topics and applications*, Springer.

46. Gribb, T. T. and Cooper, R. F. (1998), 'Low-frequency shear attenuation in polycrystalline olivine: Grain boundary diffusion and the physical significance of the Andrade model for viscoelastic rheology', *Journal of Geophysical Research: Solid Earth* **103**(B11), 27,267–27,279.

47. Hanyk, L., Matyska, C. and Yuen, D. A. (1999), 'Secular gravitational instability of a compressible viscoelastic sphere', *Geophysical Research Letters* **26**(5), 557–560.

48. Haskell, N. A. (1935), 'The motion of a viscous fluid under a surface load', *Physics* **6**(8), 265–269.

49. Haskell, N. A. (1937), 'The viscosity of the asthenosphere', *American Journal of Science* pp. 22–28.

50. Hellard, H., Csizmadia, S., Padovan, S., Rauer, H., Cabrera, J., Sohl, F., Spohn, T. and Breuer, D. (2019), 'Retrieval of the fluid Love number k_2 in exoplanetary transit curves', *The Astrophysical Journal* **878**(2), 119.

51. Hellard, H., Csizmadia, S., Padovan, S., Sohl, F., Breuer, D., Spohn, T. and Rauer, H. (2018), 'Measurability of the fluid Love number k_2 in WASP-121b', *Abstract EPSC2018-310* .

52. Hubbard, W. (1984), *Planetary Interiors*, Van Nostrand Reinhold.

53. Hubbard, W. B. (1975), 'Gravitational field of a rotating planet with a polytropic index of unity', *sovast* **18**, 621–624.

54. Hubbard, W. B. (2013), 'Concentric Maclaurin spheroid models of rotating liquid planets', *The Astrophysical Journal* **768**(1), 43.
URL: *https://dx.doi.org/10.1088/0004-637X/768/1/43*

55. Ivins, E., Caron, L., Adhikari, S., Larour, E. and Scheinert, M. (2020), 'A linear viscoelasticity for decadal to centennial time scale mantle deformation', *Reports on Progress in Physics* **83**(10), 106801.

56. Jackson, I. and Faul, U. H. (2010), 'Grainsize-sensitive viscoelastic relaxation in olivine: Towards a robust laboratory-based model for seismological application', *Physics of the Earth and Planetary Interiors* **183**(1-2), 151–163.

57. James, T. S. (1991), *Postglacial deformation*, Princeton University.

58. Jeans, J. H. (1923), 'The propagation of earthquake waves', *Proceedings of the Royal Society of London. Series A, Containing Papers of a Mathematical and Physical Character* **102**(718), 554–574.

59. Jeffreys, H. and Crampin, S. (1970), 'On the modified Lomnitz law of damping', *Monthly Notices of the Royal Astronomical Society* **147**(3), 295–301.

60. Johnston, P. (1993), 'The effect of spatially non-uniform water loads on prediction of sea-level change', *Geophysical Journal International* **114**(3), 615–634.

61. Karato, S.-i. (2021), 'A theory of inter-granular transient dislocation creep: Implications for the geophysical studies on mantle rheology', *Journal of Geophysical Research: Solid Earth* **126**(10), e2021JB022763.

62. Kaula, W. M. (1963), 'Elastic models of the mantle corresponding to variations in the external gravity field', *Journal of Geophysical Research* **68**(17), 4967–4978.

63. Kellermann, C., Becker, A. and Redmer, R. (2018), 'Interior structure models and fluid Love numbers of exoplanets in the super-Earth regime', *Astronomy & Astrophysics* **615**, A39.

64. Kennett, B. L. N. and Bunge, H.-P. (2008), *Geophysical continua: deformation in the Earth's interior*, Cambridge University Press.

65. Khan, S. A., Aschwanden, A., Bjørk, A. A., Wahr, J., Kjeldsen, K. K. and Kjaer, K. H. (2015), 'Greenland ice sheet mass balance: a review', *Reports on progress in physics* **78**(4), 046801.

66. King, M. D., Howat, I. M., Candela, S. G., Noh, M. J., Jeong, S., Noël, B. P., van den Broeke, M. R., Wouters, B. and Negrete, A. (2020), 'Dynamic ice loss from the Greenland Ice Sheet driven by sustained glacier retreat', *Communications Earth & Environment* **1**(1), 1–7.

67. Kramm, U., Nettelmann, N., Redmer, R. and Stevenson, D. J. (2011), 'On the degeneracy of the tidal Love number k_2 in multi-layer planetary models: application to Saturn and GJ 436b', *Astronomy & Astrophysics* **528**, A18.

68. Lambeck, K., Rouby, H., Purcell, A., Sun, Y. and Sambridge, M. (2014), 'Sea

level and global ice volumes from the Last Glacial Maximum to the Holocene', *Proceedings of the National Academy of Sciences* **111**(43), 15296–15303.

69. Lau, H. C. (2023), 'Transient rheology in sea level change: implications for meltwater pulse 1A', *Earth and Planetary Science Letters* **609**, 118106.

70. Lau, H. C. P. (2024), 'Surface loading on a self-gravitating, linear viscoelastic Earth: moving beyond Maxwell', *Geophysical Journal International* **237**(3), 1842–1857.
URL: *https://doi.org/10.1093/gji/ggae149*

71. Liu, L., Khan, S. A., van Dam, T., Ma, J. H. Y. and Bevis, M. (2017), 'Annual variations in GPS-measured vertical displacements near Upernavik Isstrøm (Greenland) and contributions from surface mass loading', *Journal of Geophysical Research: Solid Earth* **122**(1), 677–691.

72. Long, A. J., Woodroffe, S. A., Roberts, D. H. and Dawson, S. (2011), 'Isolation basins, sea-level changes and the Holocene history of the Greenland Ice Sheet', *Quaternary Science Reviews* **30**(27-28), 3748–3768.

73. Longman, I. (1963), 'A Green's function for determining the deformation of the Earth under surface mass loads: 2. Computations and numerical results', *Journal of Geophysical Research* **68**(2), 485–496.

74. Louchet, F. and Duval, P. (2009), 'Andrade creep revisited', *International Journal of Materials Research* **100**(10), 1433–1439.

75. Love, A. E. H. (1909), 'The yielding of the Earth to disturbing forces', *Proceedings of the Royal Society of London. Series A, Containing Papers of a Mathematical and Physical Character* **82**(551), 73–88.

76. Love, A. E. H. (1911), *Some problems of geodynamics: being an essay to which the Adams prize in the University of Cambridge was adjudged in 1911*, CUP Archive.

77. Love, A. E. H. (2013), *A treatise on the mathematical theory of elasticity*, Cambridge University Press.

78. Lubarda, V. and Lubarda, M. (2020), 'On the Kelvin, Boussinesq, and Mindlin problems', *Acta Mechanica* **231**(1), 155–178.

79. Mainardi, F. (2020), 'Why the Mittag-Leffler function can be considered the Queen Function of the fractional calculus?', *Entropy* **22**(12).

80. Mainardi, F. (2022), *Fractional calculus and waves in linear viscoelasticity: an introduction to mathematical models*, 2nd edn, World Scientific.

81. Mainardi, F., Pironi, P. and Tampieri, F. (1995), A numerical approach to the generalized Basset problem for a sphere accelerating in a viscous fluid, *in* 'Proceedings CFD', Vol. 95, pp. 105–112.

82. Mainardi, F. and Spada, G. (2011), 'Creep, relaxation and viscosity properties for basic fractional models in rheology', *The European Physical Journal Special Topics* **193**(1), 133–160.

83. Martens, H. R. (2016), Using Earth deformation caused by surface mass loading to constrain the elastic structure of the crust and mantle, PhD thesis, California Institute of Technology.

84. McCarthy, C. and Castillo-Rogez, J. C. (2013), 'Planetary ices attenuation properties', *The science of solar system ices* pp. 183–225.

85. McKenzie, D. (1967), 'The viscosity of the mantle', *Geophysical Journal International* **14**(1-4), 297–305.

86. Melini, D., Saliby, C. and Spada, G. (2022), 'On computing viscoelastic Love numbers for general planetary models: the ALMA3 code', *Geophysical Journal International* **231**(3), 1502–1517.

87. Mitrovica, J. and Peltier, W. (1992), 'A comparison of methods for the inversion of viscoelastic relaxation spectra', *Geophysical journal international* **108**(2), 410–414.

88. Mitrovica, J. X. (1996), 'Haskell [1935] revisited', *Journal of Geophysical Research: Solid Earth* **101**(B1), 555–569.

89. Mittag-Leffler, G. (1903), 'Une généralisation de l'intégrale de Laplace-Abel', *CR Acad. Sci. Paris (Ser. II)* **137**, 537–539.

90. Molodensky, S. (1977), 'Relation between Love numbers and load factors', *Izv. Phys. Solid Earth* **13**, 147–9.

91. Morlighem, M., Williams, C. N., Rignot, E., An, L., Arndt, J. E., Bamber, J. L., Catania, G., Chauché, N., Dowdeswell, J. A., Dorschel, B. et al. (2017), 'BedMachine v3: Complete bed topography and ocean bathymetry mapping of Greenland from multibeam echo sounding combined with mass conservation', *Geophysical Research Letters* **44**(21), 11–051.

92. Mott, N. (1953), 'LXXVIII. A theory of work-hardening of metals II: flow without slip-lines, recovery and creep', *The London, Edinburgh, and Dublin Philosophical Magazine and Journal of Science* **44**(354), 742–765.

93. Munk, W. H. and MacDonald, G. J. (1975), *The Rotation of the Earth: A Geophysical Discussion*, Cambridge University Press.

94. Müller, G. (1986), 'Generalized Maxwell bodies and estimates of mantle viscosity',

Geophysical Journal International **87**(3), 1113–1141.
URL: *https://doi.org/10.1111/j.1365-246X.1986.tb01986.x*

95. Nield, G. A., Barletta, V. R., Bordoni, A., King, M. A., Whitehouse, P. L., Clarke, P. J., Domack, E., Scambos, T. A. and Berthier, E. (2014), 'Rapid bedrock uplift in the Antarctic Peninsula explained by viscoelastic response to recent ice unloading', *Earth and Planetary Science Letters* **397**, 32–41.

96. Nielsen, K., Khan, S. A., Korsgaard, N. J., Kjær, K. H., Wahr, J., Bevis, M., Stearns, L. A. and Timm, L. H. (2012), 'Crustal uplift due to ice mass variability on upernavik isstrøm, west greenland', *Earth and Planetary Science Letters* **353-354**, 182–189.
URL: *https://www.sciencedirect.com/science/article/pii/S0012821X12004529*

97. Okumura, I. A. (1995), 'On the generalization of Cerruti's problem in an elastic half-space', *Doboku Gakkai Ronbunshu* **1995**(519), 1–10.

98. Olivieri, M. and Spada, G. (2015), 'Ice melting and earthquake suppression in Greenland', *Polar science* **9**(1), 94–106.

99. Padovan, S., Margot, J.-L., Hauck, S. A., Moore, W. B. and Solomon, S. C. (2014), 'The tides of Mercury and possible implications for its interior structure', *Journal of Geophysical Research: Planets* **119**(4), 850–866.

100. Padovan, S., Spohn, T., Baumeister, P., Tosi, N., Breuer, D., Csizmadia, S., Hellard, H. and Sohl, F. (2018), 'Matrix-propagator approach to compute fluid Love numbers and applicability to extrasolar planets', *Astronomy & Astrophysics* **620**, A178.

101. Pan, L., Mitrovica, J. X., Milne, G. A., Hoggard, M. J. and Woodroffe, S. A. (2024), 'Timescales of glacial isostatic adjustment in Greenland: is transient rheology required?', *Geophysical Journal International* **237**(2), 989–995.

102. Paxman, G. J., Lau, H. C., Austermann, J., Holtzman, B. K. and Havlin, C. (2023), 'Inference of the timescale-dependent apparent viscosity structure in the upper mantle beneath Greenland', *AGU Advances* **4**(2), e2022AV000751.

103. Peltier, W. (1974), 'The impulse response of a Maxwell Earth', *Reviews of Geophysics* **12**(4), 649–669.

104. Peltier, W., Drummond, R. and Tushingham, A. (1986), 'Post-glacial rebound and transient lower mantle rheology', *Geophysical Journal International* **87**(1), 79–116.

105. Peltier, W. R. (2004), 'Global glacial isostasy and the surface of the ice-age Earth: the ICE-5G (VM2) model and GRACE', *Annu. Rev. Earth Planet. Sci.* **32**(1), 111–149.

106. Peltier, W., Yuen, D. and Wu, P. (1980), 'Postglacial rebound and transient rheology', *Geophysical Research Letters* **7**(10), 733–736.

107. Plazek, D. J. and Plazek, C. T. (2021), 'A history of Andrade creep and the investigation of the dielectric dipolar Andrade creep', *Journal of Non-Crystalline Solids* **560**, 120625.

108. Pollitz, F. F. (2005), 'Transient rheology of the upper mantle beneath central Alaska inferred from the crustal velocity field following the 2002 Denali earthquake', *Journal of Geophysical Research: Solid Earth* **110**(B8).

109. Post, E. L. (1930), 'Generalized differentiation', *Transactions of the American Mathematical Society* **32**(4), 723–781.

110. Ragazzo, C. (2020), 'The theory of figures of Clairaut with focus on the gravitational modulus: inequalities and an improvement in the Darwin–Radau equation', *São Paulo Journal of Mathematical Sciences* **14**(1), 1–48.

111. Ragozzine, D. and Wolf, A. S. (2009), 'Probing the interiors of very hot Jupiters using transit light curves', *The Astrophysical Journal* **698**(2), 1778.

112. Ranalli, G. (1995), *Rheology of the Earth*, Springer Science & Business Media.

113. Reiner, M. (1964), 'The Deborah number', *Physics today* **17**(1), 62–62.

114. Renaud, J. P. and Henning, W. G. (2018), 'Increased tidal dissipation using advanced rheological models: Implications for Io and tidally active exoplanets', *The Astrophysical Journal* **857**(2), 98.

115. Rignot, E. and Kanagaratnam, P. (2006), 'Changes in the velocity structure of the Greenland Ice Sheet', *Science* **311**(5763), 986–990.

116. Roche, E. (1873), 'Essai sur la constitution et l'origine du système solaire', *Memoires de l'Academie de Montpellier (Section des Sciences)* **8**, 235–325.

117. Ruane, A. C. (2024), 'Synthesis Report of the IPCC Sixth Assessment Report (AR6)'.

118. Sabadini, R., Vermeersen, B. and Cambiotti, G. (2016), *Global dynamics of the Earth*, Springer.

119. Sabadini, R., Yuen, D. and Gasperini, P. (1985), 'The effects of transient rheology on the interpretation of lower mantle viscosity', *Geophysical Research Letters* **12**(6), 361–364.

120. Schapery, R. A. (1962*a*), Approximate methods of transform inversion for viscoelastic stress analysis, *in* '4th US National Congress on Applied Mechanics'.

121. Schapery, R. A. (1962*b*), Irreversible thermodynamics and variational principles with applications to viscoelasticity, PhD thesis, California Institute of Technology.

122. Schroeder, D., Falconer, J. and Siegfried, M. (2024), Enabling subglacial geodesy through high-precision radar sounding and gnss time series observations, Technical report, Copernicus Meetings.

123. Schutz, B. E., Zwally, H. J., Shuman, C. A., Hancock, D. and DiMarzio, J. P. (2005), 'Overview of the ICESat mission', *Geophysical research letters* **32**(21).

124. Scott-Blair, G. (1951), 'A survey of general and applied rheology', *British Journal of Applied Physics* **2**(2), 60.

125. Scott-Blair, G. (1970), 'On power equations relating stress to shear rate in rheology', *Journal of Texture Studies* **1**(4), 431–436.

126. Shepherd, A., Ivins, E. R., Barletta, V. R., Bentley, M. J., Bettadpur, S., Briggs, K. H., Bromwich, D. H., Forsberg, R., Galin, N., Horwath, M. et al. (2012), 'A reconciled estimate of ice-sheet mass balance', *Science* **338**(6111), 1183–1189.

127. Shida, T. (1912), 'On the Body Tides of the Earth, A Proposal for the International Geodetic Association', *Proceedings of the Tokyo Mathematico-Physical Society. 2nd Series* **6**(16), 242–258.

128. Simon, K. M., Riva, R. E. and Broerse, T. (2022), 'Identifying geographical patterns of transient deformation in the geological sea level record', *Journal of Geophysical Research: Solid Earth* **127**(7), e2021JB023693.

129. Sørensen, L. S., Simonsen, S. B., Nielsen, K., Lucas-Picher, P., Spada, G., Adalgeirsdottir, G., Forsberg, R. and Hvidberg, C. S. (2011), 'Mass balance of the Greenland ice sheet (2003–2008) from ICESat data–the impact of interpolation, sampling and firn density', *The Cryosphere* **5**(1), 173–186.

130. Spada, G. (1992), Rebound post-glaciale e dinamica rotazionale di un pianeta viscoelastico stratificato, PhD thesis, University of Bologna.

131. Spada, G. (2003), 'The theory behind TABOO', *Samizdat Press, Golden CO* .

132. Spada, G. (2008), 'ALMA, a Fortran program for computing the viscoelastic Love numbers of a spherically symmetric planet', *Computers & Geosciences* **34**(6), 667–687.

133. Spada, G. (2017), 'Glacial Isostatic Adjustment and Contemporary Sea Level Rise: An Overview', *Surveys in Geophysics* **38**(1), 1–33.

134. Spada, G. (2024), Personal conversation.

135. Spada, G., Antonioli, A., Boschi, L., Boschi, L., Brandi, V., Cianetti, S., Galvani, G., Giunchi, C., Perniola, B., Agostinetti, N. P. et al. (2004), 'Modeling Earth's post-glacial rebound', *Eos, Transactions American Geophysical Union* .

136. Spada, G., Barletta, V. R., Klemann, V., Riva, R., Martinec, Z., Gasperini, P., Lund, B., Wolf, D., Vermeersen, L. and King, M. (2011), 'A benchmark study for glacial isostatic adjustment codes', *Geophysical Journal International* **185**(1), 106–132.

137. Spada, G. and Boschi, L. (2006), 'Using the Post—Widder formula to compute the Earth's viscoelastic Love numbers', *Geophysical Journal International* **166**(1), 309–321.

138. Spada, G., Galassi, G. and Olivieri, M. (2014), 'A study of the longest tide gauge sea-level record in Greenland (Nuuk/Godthab, 1958–2002)', *Global and planetary change* **118**, 42–51.

139. Spada, G. and Melini, D. (2019), 'SELEN^4 (SELEN version 4.0): a Fortran program for solving the gravitationally and topographically self-consistent sea-level equation in glacial isostatic adjustment modeling', *Geoscientific Model Develop-*

ment **12**(12), 5055–5075.
URL: *https://www.geosci-model-dev.net/12/5055/2019/*

140. Spada, G., Ruggieri, G., Sørensen, L. S., Nielsen, K., Melini, D. and Colleoni, F. (2012), 'Greenland uplift and regional sea level changes from ICESat observations and GIA modelling', *Geophysical Journal International* **189**(3), 1457–1474.

141. Spada, G. and Stocchi, P. (2006), *The sea level equation, theory and numerical examples*, Aracne Editrice.

142. Spada, G. and Stocchi, P. (2007), 'SELEN: A Fortran 90 program for solving the "sea-level equation"', *Computers & Geosciences* **33**(4), 538–562.

143. Spada, G. et al. (2003), 'TABOO – user guide', *Samizdat Press, Golden CO* .

144. Steinbrügge, G., Padovan, S., Hussmann, H., Steinke, T., Stark, A. and Oberst, J. (2018), 'Viscoelastic tides of Mercury and the determination of its inner core size', *Journal of Geophysical Research: Planets* **123**(10), 2760–2772.

145. Sundberg, M. and Cooper, R. F. (2010), 'A composite viscoelastic model for incorporating grain boundary sliding and transient diffusion creep; correlating creep and attenuation responses for materials with a fine grain size', *Philosophical Magazine* **90**(20), 2817–2840.
URL: *https://doi.org/10.1080/14786431003746656*

146. Swarr, M. J., Martens, H. R. and Fu, Y. (2024), 'Sensitivity of GNSS-derived estimates of terrestrial water storage to assumed Earth structure', *Journal of Geophysical Research: Solid Earth* **129**(3), e2023JB027938.

147. Tan, B. H., Jackson, I. and Fitz Gerald, J. D. (1997), 'Shear wave dispersion and attenuation in fine-grained synthetic olivine aggregates: Preliminary results', *Geophysical Research Letters* **24**(9), 1055–1058.

148. The IMBIE team (2020), 'Mass balance of the Greenland Ice Sheet from 1992 to 2018', *Nature* **579**(7798), 233–239.

149. Thomson, W. (1848), 'Note on the integration of the equations of equilibrium of an elastic solid', *Cambridge and Dublin Mathematical Journal* **3**, 87–89.

150. Thomson, W. (1863), 'XXVII. On the rigidity of the Earth', *Philosophical Transactions of the Royal Society of London* **153**, 573–582.

151. Tobie, G., Grasset, O., Dumoulin, C. and Mocquet, A. (2019), 'Tidal response of rocky and ice-rich exoplanets', *Astronomy & Astrophysics* **630**, A70.

152. Ultee, L., Felikson, D., Minchew, B., Stearns, L. A. and Riel, B. (2022), 'Helheim Glacier ice velocity variability responds to runoff and terminus position change at different timescales', *Nature Communications* **13**(1), 6022.

153. Vermeersen, L. and Mitrovica, J. (2000), 'Gravitational stability of spherical self-gravitating relaxation models', *Geophysical Journal International* **142**(2), 351–360.

154. Virtanen, P., Gommers, R., Oliphant, T. E., Haberland, M., Reddy, T., Cournapeau, D., Burovski, E., Peterson, P., Weckesser, W., Bright, J., van der Walt, S. J., Brett, M., Wilson, J., Millman, K. J., Mayorov, N., Nelson, A. R. J., Jones, E., Kern, R., Larson, E., Carey, C. J., Polat, İ., Feng, Y., Moore, E. W., VanderPlas, J., Laxalde, D., Perktold, J., Cimrman, R., Henriksen, I., Quintero, E. A., Harris, C. R., Archibald, A. M., Ribeiro, A. H., Pedregosa, F., van Mulbregt, P. and SciPy 1.0 Contributors (2020), 'SciPy 1.0: Fundamental Algorithms for Scientific Computing in Python', *Nature Methods* **17**, 261–272.

155. Wahl, S. M., Hubbard, W. B. and Militzer, B. (2017), 'The Concentric Maclaurin Spheroid method with tides and a rotational enhancement of Saturn's tidal

response', *Icarus* **282**, 183–194.
URL: *https://www.sciencedirect.com/science/article/pii/S0019103516305735*

156. Wahl, S. M., Parisi, M., Folkner, W. M., Hubbard, W. B. and Militzer, B. (2020), 'Equilibrium Tidal Response of Jupiter: Detectability by the Juno Spacecraft', *The Astrophysical Journal* **891**(1), 42.
URL: *https://dx.doi.org/10.3847/1538-4357/ab6cf9*

157. Wahr, J., Molenaar, M. and Bryan, F. (1998), 'Time variability of the earth's gravity field: Hydrological and oceanic effects and their possible detection using grace', *Journal of Geophysical Research: Solid Earth* **103**(B12), 30205–30229.

158. Walterová, M., Plesa, A.-C., Wagner, F. W. and Breuer, D. (2023), 'Andrade rheology in planetary science', *ESS Open Archive eprints* **992**, essoar–169008299.

159. Weiss, J. R., Qiu, Q., Barbot, S., Wright, T. J., Foster, J. H., Saunders, A., Brooks, B. A., Bevis, M., Kendrick, E., Ericksen, T. L., Avery, J., Smalley, R., Cimbaro, S. R., Lenzano, L. E., Barón, J., Báez, J. C. and Echalar, A. (2019), 'Illuminating subduction zone rheological properties in the wake of a giant earthquake', *Science Advances* **5**(12), eaax6720.

160. Whitehouse, P. L. (2018), 'Glacial isostatic adjustment modelling: historical perspectives, recent advances, and future directions', *Earth surface dynamics* **6**(2), 401–429.

161. Widder, D. V. (1934), 'The inversion of the Laplace integral and the related moment problem', *Transactions of the American Mathematical Society* **36**(1), 107–200.

162. Williams, J. J., Gourmelen, N., Nienow, P., Bunce, C. and Slater, D. (2021), 'Helheim Glacier poised for dramatic retreat', *Geophysical Research Letters* **48**(23), e2021GL094546.

163. Wolfram Research (2010), 'Mathematica 8.0'.

164. Wolfram Research, Inc. (2024), *Mathematica, Version 14.0*, Wolfram Research, Inc., Champaign, Illinois.
URL: *https://www.wolfram.com/mathematica*

165. Woodward, R. S. (1888), *On the Form and Position of the Sea Level: With Special References to Its Dependence on Superficial Masses Symmetrically Disposed about a Normal to the Earth's Surface*, number 48, US Government Printing Office.

166. Wu, P. and Peltier, W. (1982), 'Viscous gravitational relaxation', *Geophysical Journal International* **70**(2), 435–485.

167. Wu, P. and Peltier, W. (1984), 'Pleistocene deglaciation and the earth's rotation: a new analysis', *Geophysical Journal International* **76**(3), 753–791.

168. Yuen, D. A., Sabadini, R. and Boschi, E. V. (1982), 'Viscosity of the lower mantle as inferred from rotational data', *Journal of Geophysical Research: Solid Earth* **87**(B13), 10745–10762.

169. Yuen, D. A., Sabadini, R. C., Gasperini, P. and Boschi, E. (1986), 'On transient rheology and glacial isostasy', *Journal of Geophysical Research: Solid Earth* **91**(B11), 11420–11438.

170. Zhang, C. (1992), 'Love numbers of the Moon and of the terrestrial planets', *Earth, Moon, and Planets* **56**(3), 193–207.

Acknowledgments / Ringraziamenti

In queste righe vorrei ringraziare il mio supervisore, il Prof. Giorgio Spada, che in questi tre anni mi ha seguita e incoraggiata continuamente. Grazie al suo supporto ho potuto svolgere questo dottorato in un ambiente sano e stimolante. Devo a lui il realizzarsi di questo primo passo all'interno del mondo accademico. Inoltre, vorrei ringraziare anche il mio co-supervisore, il Dott. Daniele Melini, sempre gentile e disponibile: senza il suo aiuto molti degli strumenti indispensabili per la realizzazione di questa tesi non esisterebbero. Entrambi hanno reso possibile questo mio percorso, e sono onorata di aver potuto imparare da loro. Vorrei anche ringraziare la Dott.ssa Valentina Barletta, che mi ha ospitato durante i tre mesi passati a Copenhagen: è stato un periodo bellissimo che ricorderò per sempre con grande gioia. Inoltre un ringraziamento va anche ai Prof. Anthony Memin e Nicola Piana Agostinetti, che hanno attentamente revisionato la tesi.

Ovviamente, rivolgo un immenso grazie ai miei genitori, Anna e Andrea, ed Elettra, mia sorella. Da sempre sono i miei primi sostenitori, e senza di loro tutto questo non sarebbe stato possibile. Grazie per aver creduto in me. A Cesare, Martina, Letizia, Riccardo, Sofia e Chiara va il merito di aver alleviato le giornate lavorative più faticose con risate e leggerezza. A Laura ed Eleonora, amiche da una vita, va un enorme grazie per aver sopportato le mie assenze e i miei deliri. Un pensiero va anche alle mie amiche Angelica, Alessandra, Alessandra, Behnaz, Gloria, Luana, Rita e Veronica, con le quali ho condiviso tanti bellissimi momenti qui a Bologna. Infine, un sentito grazie a Marco, che nonostante la distanza, non ha mai smesso di starmi vicino. Grazie per essere stato

una presenza così positiva e costante, e per avermi sempre motivata a credere nelle mie capacità, anche quando per prima ne dubitavo.